Doctoral Thesis

Development of Sheet-Type All-Solid-State Li-Ion Batteries Using Solution-Processable Sulfide Solid Electrolytes

Dong Hyeon Kim

Department of Energy Engineering

(Battery Science and Technology)

Graduate School of UNIST

2020

Development of Sheet-Type All-Solid-State Li-Ion Batteries Using Solution-Processable Sulfide Solid Electrolytes

Dong Hyeon Kim

Department of Energy Engineering
(Battery Science and Technology)

Graduate School of UNIST

Development of Sheet-Type All-Solid-State Li-Ion Batteries Using Solution-Processable Sulfide Solid Electrolytes

A dissertation
submitted to the Graduate School of UNIST
in partial fulfillment of the
requirements for the degree of
Doctor of Philosophy

Dong Hyeon Kim

12/09/2019

Approved by

Advisor
Youngsik Kim

Development of Sheet-Type All-Solid-State Li-Ion Batteries Using Solution-Processable Sulfide Solid Electrolytes

Dong Hyeon Kim

This certifies that the dissertation of Dong Hyeon Kim is approved.

12/09/2019

signature

Advisor: Youngsik Kim

signature

Advisor: Yoon Seok Jung

signature

Sang-Young Lee

signature

Kyeong-Min Jeong

signature

Hyun-Wook Lee

Abstract

Dong Hyeon Kim
School of Energy and Chemical Engineering, UNIST
Advisor - Yoon Seok Jung

With increasing demand for the application of conventional lithium-ion batteries (LIBs) to large-scale energy storage devices, associated safety concerns arising from the flammable organic liquid electrolytes (LEs) become more critical. Recently, all-solid-state lithium-ion batteries (ASLBs) using inorganic solid electrolytes (SEs) are considered a promising alternative to conventional LIBs in perspective of battery safety and energy density. Especially, sulfide SE materials are attracting great attention owing to high Li^+ conductivities of 10^{-2}–10^{-3} S cm^{-1} and deformability. From practical point of view, development of sheet-type electrodes and thin SE membranes are imperative for realizing practical high-energy all-solid-state cells. The solution-based process including polymeric components is common protocol for fabricating sheet-type electrodes in conventional LIBs. However, severe reactivity of sulfide SEs to common polar solvents and the particulate properties of these SEs lead to serious complications in the wet-slurry process for used to fabricate ASLB electrodes or SE membranes, such as the availability of solvents and polymeric binders and the formation of ionic contacts and percolation.

In this work, a new scalable fabrication protocol for sheet-type ASLB is developed by solution-processable sulfide SEs (Li_6PS_5[Cl,Br]), combined with the conventional composite LIB electrodes or porous polymer membranes. Firstly, fabrication of the sheet-type ASLB electrode is demonstrated. The liquefied SE is infiltrated into the pores of LIB electrodes and then solidified, achieving high surface coverage of SE and favorable Li^+ pathways. The SE-infiltrated $LiCoO_2$ (LCO) and graphite (Gr) electrodes show high reversible capacities, which is comparable to LE-based cells and outperforms to conventional dry-mixed electrodes. The all-solid-state LCO/Gr full cells using SE-infiltrated electrodes demonstrate the promising electrochemical performance at both 30 °C and 100 °C, highlighting the excellent thermal stability of ASLBs.

Moreover, sheet-type Si electrodes is fabricated and their electrochemical performance with variation of particle size of Si, polymeric binders, and external pressure is systematically investigated. Owing to intimate ionic contact by homogenous SE solution, the SE-infiltrated Si electrodes show high reversible capacities of over 3000 mA h g^{-1} and initial Coulombic efficiencies (CEs) over 80% at 30 °C. The large difference in initial CEs between Si electrode with external pressure of 20 MPa and 5 MPa indicates the importance of engineering of external pressure. The high energy density of 338 W h kg_{LCO+Si}^{-1} is

achieved for the LCO/Si full cell, which is improved by 21% compared to that of LCO/Gr full cell.

Finally, the flexible and thin (40–70 μm) SE membranes are developed by combining solution-processable SEs ($Li_6PS_5Cl_{0.5}Br_{0.5}$ (LPSClBr)) with mechanically compliant and thermally stable polymer membranes (polyimide (PI)). The PI-LPSClBr membrane exhibits the Li^+ conductivity of 0.2 mS cm^{-1} at 30 °C with significantly reducing the mass loading of SE layer (5.0–9.5 mg cm^{-2} for PI-LPSClBr and 113 mg cm^{-2} for thick SE layer). The $LiNi_{0.6}Co_{0.2}Mn_{0.2}O_2$/graphite full cell using PI-LPSClBr shows promising electrochemical performance (at 30 °C without liquid electrolytes) and excellent thermal stability, outperforming the ASLBs using composite solid electrolyte (PEO-LiTFSI including inorganic filler). Finally, the SE injection process, similar to liquid electrolyte injection in conventional LIBs, is successfully demonstrated.

Contents

List of figures

$_x$-infiltrated PI membranes.

Figure 51. Cross-sectional SEM image of NCM/PI-$Li_6PS_5Cl_{0.5}Br_{0.5}$/LTO all-solid-state full-cells and its corresponding elemental maps.

Figure 52. Results of NCM/LTO all-solid-state full-cells employing PI (or PE)-$Li_6PS_5Cl_{0.5}Br_{0.5}$ membranes. a) First-cycle charge-discharge voltage profiles of NCM/PI-$Li_6PS_5Cl_{0.5}Br_{0.5}$/LTO and NCM/PEI-$Li_6PS_5Cl_{0.5}Br_{0.5}$/LTO all-solid-state full-cells at 30 ^oC and b) their corresponding rate capabilities.

Figure 53. Results of all-solid-state full-cells employing PI-$Li_6PS_5Cl_{0.5}Br_{0.5}$ membranes. a) First two-cycle charge-discharge voltage profiles and b) the corresponding cycling performance of NCM/graphite all-solid-state full-cells employing PI-$Li_6PS_5Cl_{0.5}Br_{0.5}$ membranes at 0.1C and 30 ^oC.

Figure 54. Charge-discharge voltage profiles for NCM/graphite all-solid-state full-cells employing PI-$Li_6PS_5Cl_{0.5}Br_{0.5}$ membranes at 0.1C and 30 ^oC before and after exposure to 180 ^oC for 1 h.

Figure 55. Photographs of PEO-LiTFSI including 10 wt % of Al_2O_3 before and after exposure to high temperature (180 and 400 °C).

Figure 56. a) Schematic illustrating fabrication of ASLBs by injection of liquefied sulfide SEs ($Li_6PS_5Cl_{0.5}Br_{0.5}$-EtOH solution) into Al/NCM/PI NWs/LTO/Al assemblies and b) the corresponding first-cycle charge-discharge voltage profiles at 0.1C and 70 °C.

List of tables

Nomenclature

LIB	Lithium-ion battery
LE	Liquid electrolyte
EV	Electric vehicle
SEI	Solid electrolyte interphase
SE	Solid electrolyte
ASLB	All-solid-state lithium-ion battery
LTO	$Li_4Ti_5O_{12}$
AM	Active material
PVDF	Poly(vinylidene fluoride)
PAA	Poly(acrylic acid)
CMC	Carboxymethyl cellulose
NMP	N-methyl-2-pyrrolidinone
PEO	Polyethylene oxide
OPC	Oxide-polymer composite
RT	Room temperature
LCO	$LiCoO_2$
Gr	Graphite
LPSClBr	$Li_6PS_5Cl_{0.5}Br_{0.5}$
PI	Polyimide
LGPS	$Li_{10}GeP_2S_{12}$
MIEC	Mixed ionic and electronic conducting
ACN	Acetonitrile
THF	Tetrahydrofuran
DME	Dimethoxyethane
LPSCl	Li_6PS_5Cl
LPS	Li_3PS_4
BM-LPSCl	Ball-milled Li_6PS_5Cl
Sol-LPSCl	Solution-processed Li_6PS_5Cl
PAA	Polyamic acid
PDMA	Pyromellitic dianhydride
PEI	Polyetherimide
TMA	Trimethylaluminum
LiTFSI	Lithium bis(trifluoromethanesulfonyl)imide
G3	Triethylene glycol dimethyl ether
Li(G3)TFSI	Equimolar mixture of LiTFSI and G3 (triglyme)
NCM	$LiNi_{0.6}Co_{0.2}Mn_{0.2}O_2$
FTIR	Fourier transform infrared spectroscopy
TGA	Thermogravimetric analysis
FESEM	Field-emission scanning electron microscopy
EDXS	Energy dispersive X-ray spectroscopy
HRTEM	High-resolution transmission electron microscopy
PEEK	Polyaryletheretherketone
EIS	Electrochemical impedance spectroscopy
GITT	Galvanostatic intermittent titration technique

1. Introduction

Since the commercialization of conventional lithium-ion batteries (LIBs) in early 1990s, they have been dominantly used for portable electronics owing to their higher energy and power densities than those of other secondary batteries.[1-6] The development of the layered cathode materials ($LiCoO_2$) and carbonaceous anode materials (graphite) based on intercalation chemistries significantly contributed to commercialization of current LIB systems.[4, 7-9] Moreover, employment of the organic liquid electrolytes (LEs), such as lithium hexafluorophosphate ($LiPF_6$) dissolved in carbonate-based solvents, allowed the employment of high-voltage electrode chemistries for conventional LIBs by forming stable solid electrolyte interphase (SEI) especially for graphite anode.[10-11] Over 20 years, the gradual increase of Ni contents and cut-off voltage for $LiNi_xCo_yMn_zO_2$ cathode materials and exploration of alternative anode materials such as Li metal, silicon have been main research trends for both the academic and industrial point of views.[12-15] Furthermore, engineering for minimizing the inactive components (separator, electrolytes, binders, carbon additives, cell packaging) significantly decreased the weight and volume of battery. These continuous progresses in LIB technologies in perspective of materials and engineering aspects resulted in stepwise increase of energy densities, leaching to 250 W h kg_{cell}^{-1}.[2, 16] The ongoing interests in electric vehicles (EVs) and grid-scale energy storage system require further improvement of current LIBs with respect to energy densities and cycle life. While higher upper cutoff voltage or thinning polymeric separator could increase the energy density, associated safety concerns also become more serious, which is originated from flammable organic liquid electrolytes. For expanding the application of current LIBs to large-scale devices such as EVs and energy storage systems (ESSs), battery safety become prime of importance.[17-18]

In this regard, replacement of conventional LEs with inorganic solid electrolytes (SEs) is considered as ideal solution for battery safety.[19-24] All-solid-state lithium-ion batteries (ASLBs) employing nonflammable inorganic SEs have attracted great attention as a promising alternative to conventional LIBs owing to their ultimate safety and potential to surpass the energy density of LIBs by stacking bipolar electrodes and minimizing inactive components in the battery pack.[25-26] Moreover, possible application of Li metal has led to explosive interests in research for ASLBs.[27-28] For high-performance ASLBs, requirement for SEs are i) high Li^+ conductivity at wide temperature range, ii) electrochemical stability, iii) favorable mechanical properties, iv) compatibility with various electrode materials. There have been mainly two different kinds of inorganic SEs, oxide- and sulfide-based SEs. Oxide SEs show the Li^+ conductivities in the range of 10^{-3}–10^{-4} S cm^{-1} at room temperature and have better chemical stability compared to sulfide SEs.[22, 29] However, due to the poor mechanical properties, high temperature sintering process is required to form ionic contacts. This sintering process causes unwanted side reactions with active materials such as LCO, thereby forming highly resistive interphase. In contrast, owing to higher polarizability of sulfur atom than oxygen atom, sulfide SEs are softer and more

deformable than oxide SEs. This means that sulfide SEs enable to form 2D ionic contacts by simple cold-pressing, which is contrast to high-temperature sintering of oxide SEs.[21, 30] Moreover, there has been a remarkable progress in sulfide SEs in terms of Li-ion conductivities, achieving the comparable Li^+ conductivities to those of LEs (e.g., $Li_{10}GeP_2S_{12}$: 1.2×10^{-2} S cm^{-1}, $Li_{9.54}Si_{1.74}P_{1.44}S_{11.7}Cl_{0.3}$: 2.5×10^{-2} S cm^{-1}, $Li_7P_3S_{11}$: 1.7×10^{-2} S cm^{-1}, Li_6PS_5X: $\geq 1.0 \times 10^{-3}$ S cm^{-1}, $Li_{6+x}P_{1-x}Ge_xS_5I$: $1.84 \pm 2.7 \times 10^{-2}$ S cm^{-1}, $Li_{5.5}PS_{4.5}Cl_{1.5}$: $1.2 \pm 0.2 \times 10^{-2}$ S cm^{-1}, $Li_{6.6}Si_{0.6}Sb_{0.4}S_5I$: 2.4×10^{-2} S cm^{-1}).[25, 31-34] In these regards, sulfide SEs are considered as more promising candidates for high-performance ASLBs compare to oxide SEs. Furthermore, considering the higher Li^+ transference number of SEs (close to 1) compared to LEs (< 0.5), Li^+ conductivities of sulfide SEs are enough to realize high-energy ASLBs.[30]

Compared to thin-film type ASLBs using vacuum deposition technique, composite-structured bulk type ASLBs are more attractive in perspective of energy density, processing cost, and scalable fabrication (Figure 1).[21] Owing to similarity with conventional LIBs, electrode materials, used for LIBs such as $LiMO_2$ (M = Co, Ni, Mn), graphite, sulfur-based electrodes, and $Li_4Ti_5O_{12}$ (LTO), have been widely used for bulk-type ASLBs. Conventional composite electrodes of ASLBs are fabricated based on the manually mixing electrode components (active materials (AM), SEs, carbon additives) in dry conditions, followed by cold-pressing.[30, 35-36] However, the dry-mixed composite electrodes show limited contact area between active materials and SEs, which is contrasted by the case of conventional LIBs that all the exposed surface of AM was wetted by LEs ensuring the intimate ionic contacts. Dry-mixing protocol for fabricating electrodes causes poor ionic contacts, which results in lower electrochemical performance than expected even though high ionic conductivities of sulfide SEs (10^{-2} ~ 10^{-3} S cm^{-1}). While the direct coating of SEs on AM by pulsed laser deposition was reported, high cost is obstacle for commercialization.[30, 37] In this regards, cost-effective solution-based protocol is considered as promising ways to solve ionic contact issues. Wet-synthesis of β-Li_3PS_4, based on Li_2S and P_2S_5 in tetrahydrofuran (THF), was firstly reported in 2013, showing the Li^+ conductivity of 1.6 x 10^{-4} S cm^{-1}.[38] As motivated by this work, wet-syntheses of other sulfide SEs (e.g., $Li_7P_2S_8I$, $Li_7P_3S_{11}$), also reported,[39-41] highlighting the unique advantages of wet-syntheses such as low heat-treatment temperature and control of particle size and morphology. In contrast to wet-synthesis staring from precursors, recent reports showed that as-prepared sulfide SEs dissolved in polar solvents, forming homogeneous SE solution (e.g., 0.4LiI-0.6Li_4SnS_4 in MeOH, Li_6PS_5Cl (LPSCl) in EtOH, Na_3SbS_4 in MeOH).[36, 42-43] Direct SE coating on active materials significantly improved electrochemical performance of ASLBs, emphasizing the importance of ionic contacts.

From the viewpoint of practical application of ASLBs, sheet-type electrodes are imperative.[44] Dry-mixed pelletized electrodes are hard to be employed for scalable process because of poor mechanical properties. As in the case of LIBs, wet-slurry process including polymeric binders is imperative to fabricate roll-to-roll processable sheet-type electrodes. Unfortunately, the application of conventional

polymeric binders and solvents (e.g., poly(vinylidene fluoride) (PVDF), poly(acrylic acid) (PAA), carboxymethyl cellulose (CMC)) and solvents (N-methyl-2-pyrrolidinone (NMP) or water) is hindered due to severe reactivity of sulfide SEs with polar solvents.[45-46] Thus, the choice of solvents for wet-slurry process of ASLBs is limited to nonpolar or very less polar aprotic solvents such as xylene and toluene. The availability of polymeric binders is also highly restricted to those are soluble in xylene or toluene, such as nitrile-butadiene rubber (NBR), styrene-butadiene rubber (SBR), and silicone rubber.[47-50] Moreover, the optimization of wet-slurry process for ASLBs require the homogenization of four components (active materials, SEs, carbon additives, and polymeric binders) for achieving favorable ion/electron conduction pathway simultaneously. Additional consideration is required compared to slurry process of conventional LIBs which is three components system. Furthermore, many variables such as size/morphology of components, and slurry mixing condition may be critical for electrochemical performance of ASLBs, which could increase engineering costs.[51]

On the other hand, with respect to the cell-based energy density, development of free-standing and thin SE membranes is required.[52-53] The thick SE layer (> 500 μm) has been widely used for evaluating all-solid-state cells, which is contrasted by thin separator (< 20 μm) of commercialized LIBs. The SE layers as thin as possible is highly desirable in perspective of energy density. Recent work by Li and co-workers showed that required thickness of SE layer is 30–100 μm for competing with conventional LIBs.[53] While direct coating of SE slurry including polymeric binder on either cathode or anodes was used for reducing the thickness of SE layers, the use of same binder and processing solvent for both in electrodes and SE layers could cause the inhomogeneity at interface, which is more severe for electrode with larger dimension.[44] In these regards, development of the free-standing and thin SE membranes is indispensable to realize high performance ASLBs and of great interest to both academic and industrial viewpoint. For SE membranes, both oxide and sulfide SEs were combined with polymers to improve mechanical properties, which could allow the employment of scalable process.[52, 54] However, incorporation polymer possibly degrades the thermal stability of SE layer, which is directly related with battery safety. The SE membranes, similar to separator in LIBs, have to maintain it original dimension without shrinkage and melting at elevated temperature for preventing internal short circuit.

For SE membranes, introduction of polymeric components is required to improve mechanical properties. To date, most of previous researches on SE membranes have been focused on oxide-polymer composites (OPCs) consist of polymer electrolyte and oxide SEs.[27, 55-62] Polyethylene oxide (PEO) was mostly used for polymer host in OPCs. Recently, incorporation of nanowire oxide SEs into polymer electrolyte significantly improved the Li^+ conductivities of ~0.1 mS cm^{-1} at RT, which is induced by the fast Li^+ transport by interfacial layer.[62] However, the high temperature condition (50–80 °C) is still required for operation of ASLBs and poor electrochemical stability of PEO limits the cathode materials operating below 4 V.[27, 61, 63] More recently, multilayered SE membranes were also reported by combining

the oxidative stable poly(acrylonitrile) and reduction-resistant polyethylene glycol diacrylate.[64] While the $LiNi_{0.8}Co_{0.1}Mn_{0.1}O_2$/Li cells using this membrane shows promising electrochemical performance with expanded electrochemical window, it should be noted that small amount of liquid electrolyte was added for operation at RT. In contrast, despite of favorable properties of sulfide SEs, there are only few reports for sulfide SE-based membranes due to the chemical instability which hinders the application of solution-based process.[52, 54, 65-66]

As motivated by aforementioned issues, a new scalable fabrication protocol for sheet-type electrodes and thin SE membranes is developed by solution-processable sulfide SEs (Li_6PS_5[Cl,Br]), combined with the conventional composite LIB electrodes or porous polymer membranes. Firstly, fabrication of the sheet-type ASLB electrode is demonstrated. The liquefied SE is infiltrated into the pores of LIB electrodes and then solidified, achieving high surface coverage of SE and favorable Li^+ pathways. The SE-infiltrated $LiCoO_2$ (LCO) and graphite (Gr) electrodes show high reversible capacities, which is comparable to LE-based cells and outperforms to conventional dry-mixed electrodes. The all-solid-state LCO/Gr full cells using SE-infiltrated electrodes demonstrate the promising electrochemical performance at both 30 °C and 100 °C, highlighting the excellent thermal stability of ASLBs. Moreover, sheet-type Si electrodes is fabricated and their electrochemical performance with variation of particle size of Si, polymeric binders, and external pressure is systematically investigated. Finally, the flexible and thin (40–70 μm) SE membranes are developed by combining solution-processable SEs ($Li_6PS_5Cl_{0.5}Br_{0.5}$ (LPSClBr)) with mechanically compliant and thermally stable polymer membranes (polyimide (PI)). The PI-LPSClBr membrane exhibits the Li^+ conductivity of 0.2 mS cm^{-1} at 30 °C with significantly reducing the mass loading of SE layer (5.0–9.5 mg cm^{-2} for PI-LPSClBr and 113 mg cm^{-2} for thick SE layer). The $LiNi_{0.6}Co_{0.2}Mn_{0.2}O_2$/graphite full cell using PI-LPSClBr shows promising electrochemical performance (at 30 °C without liquid electrolytes) and excellent thermal stability.

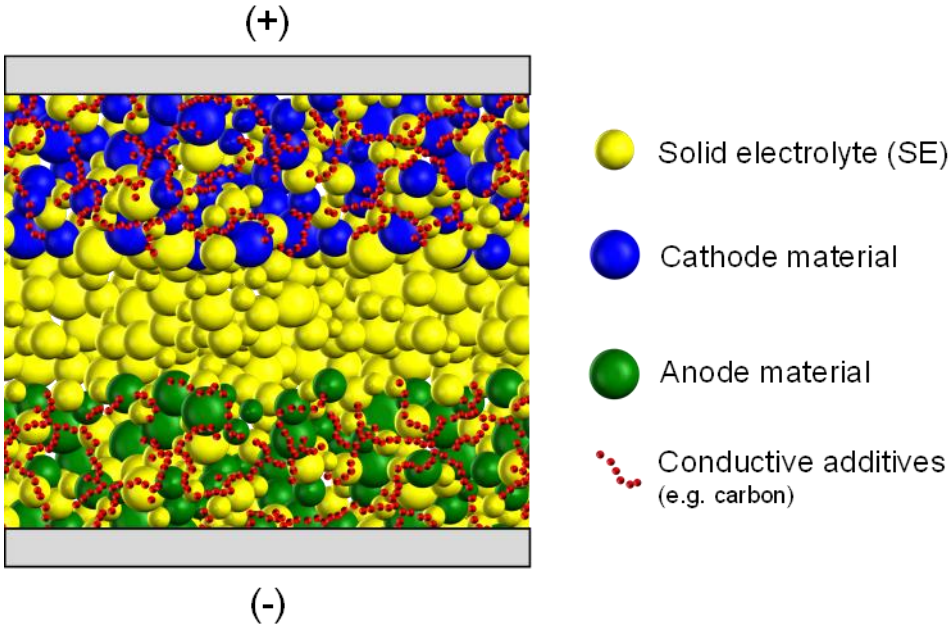

Figure 1. Schematic diagram of bulk-type all-solid-state batteries. Reproduced with permission.[21] Copyright 2015, Wiley-VCH.

2. Background

2.1 Basic principle of lithium-ion batteries

With growing demands for reliable energy storage systems, rechargeable lithium-ion batteries (LIBs) are getting great attention owing to their high energy/power densities and efficiencies, compared to other secondary batteries. Conventional LIBs are composed of cathode, anode, liquid electrolyte (LE), and separator (Figure 2).[1] In rechargeable batteries, anode means where the oxidation is taking place during discharging and the reduction is occurred in cathode. In most common cases, transition metal oxide ($LiMO_2$ (M = Ni, Co, Mn)) and graphite (Gr) were used as cathode and anodes, respectively. During charging, $LiMO_2$ is oxidized by extracting Li^+ and losing e-, whereas Gr is reduced. During discharging, opposite reaction takes place by transform chemical energy to electrical energy. Overall, lithium-ions are reversibly extracted (charge) and intercalated (discharge) between two electrodes with electron flow through external circuit during operation of batteries, which is expressed by

$$LiMO_2 + C_6 \leftrightarrows Li_{1-x}MO_2 + Li_XC_6,\ x = \sim 0.5$$

The cell capacity is related with the amount of reversibly intercalated lithium ions and cell voltage is determined by difference of electrochemical potential of cathode and anode. The energy of batteries is calculated by multiplying capacity and voltage.

In case of $LiCoO_2$, the amount of reversibly extracted/intercalated lithium-ions limited to ~0.5, which is related with structural instability. In anode side (Gr), irreversible consumption of lithium is occurred by reductive decomposition of LEs at initial cycles, thereby forming solid electrolyte interphase (SEI). For LEs, $LiPF_6$ was dissolved in mixture of carbonate-based solvents (e.g., ethylene carbonate (EC), diethyl carbonate (DEC), dimethyl carbonate (DMC)). The development of these carbonate-based LEs significantly contributed to commercialization of LIBs, enabling the application of the high-voltage electrode chemistries such as LCO and Gr (average voltage of ~3.7 V).[10] It is attributed to the formation of stable SEI at initial cycles. The Li^+ conductivity of LEs are in range of 10^{-2}–10^{-3} S cm^{-1}, which is affected by the types of Li salt, solvent, and concentration. The major drawback of LEs are low Li^+ transference number (< 0.5), which could cause concentration polarization at high current density. Separator acts as physical barriers between electrodes, preventing short-circuit. For separators, requirements are i) mechanical strength, ii) wettability to LEs, iii) high porosity to uptake enough LEs, iv) thickness, v) thermal stability which is directly related battery safety, vi) electrochemical and chemical stability.

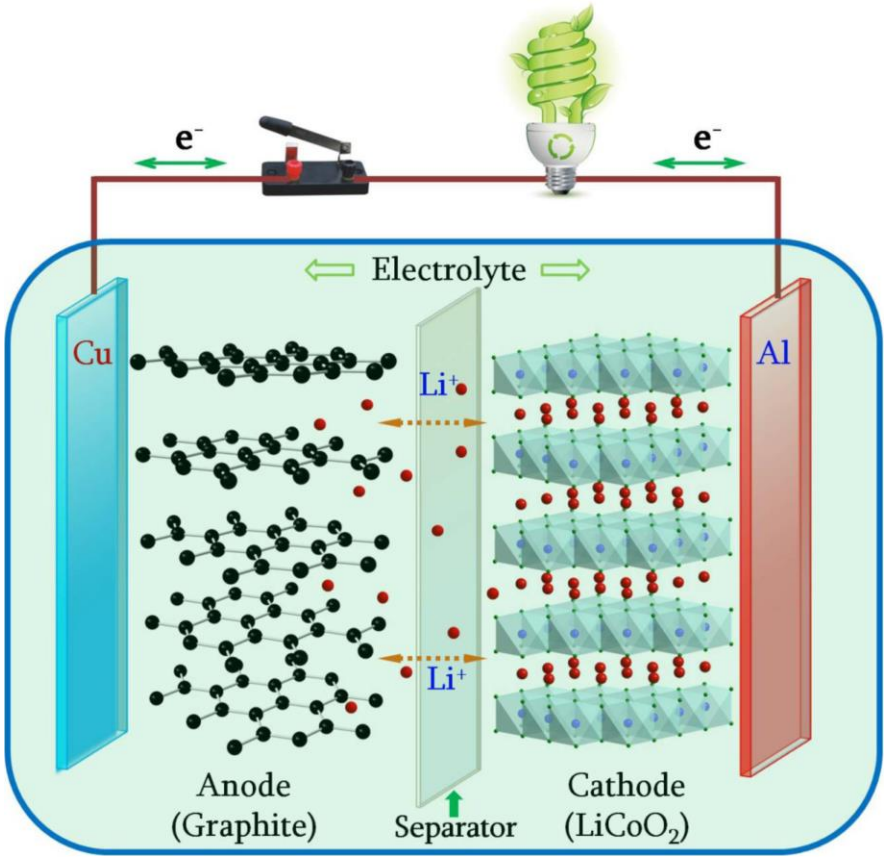

Figure 2. Schematic of the configuration of rechargeable Li-ion batteries. Reproduced with permission.[9] Copyright 2016, Elsevier

2.2 All-solid-state lithium-ion batteries

2.2.1 Solid electrolytes for all-solid-state batteries

Development of highly conductive solid electrolytes are key issues for realizing high performance ASLBs. The ion transport mechanism of SEs is totally different from the LEs in conventional LIBs. While both the cations and anions are mobile for LEs, only cations are mobile in SEs. Moreover, solvation and de-solvation process at electrode-electrolyte interface is not required for SEs. These features led to possibly expect the promising electrochemical performance of ASLBs.[29]

To date, difference classes of SEs have been reported. Arrhenius plots of Li^+ conductivities for these SEs are also shown in Figure 3. To achieve high ionic conductivity, requirement for crystalline SEs are i) enough concentration of mobile charge carries, iii) available empty site with low activation barriers, iii) open frameworks having continuous 3D conduction ion pathways, iv) highly polarizable frameworks. The overall ionic conductivity affected by these factors is expressed by

$$\sigma = \frac{A}{T} n_c \exp\left(-\frac{E_a}{kT}\right),$$

(*A* is a constant related to the crystal structure, n_c is the concentration of mobile-ion carriers (e.g., vacancy or interstitial), E_a is the activation energy for ion transport, *T* is temperature in K, and *k* is the Boltzmann constant).[30]

Compared to oxide SEs, sulfide SEs show higher ionic conductivities, which is attributed to highly polarizable sulfur. Larger open channels for lithium conduction could be formed by sulfur having a bigger ionic radius than oxygen, thereby lowering migration energy barriers. Furthermore, in contrast to high-temperature process for oxide SEs, sulfide SEs are mechanically sinterable by simple cold-pressing. These advantages of sulfide SEs over oxides one has led to explosive interest for development of new, highly conductive sulfide SEs.[67]

Glass-ceramic Li_2S-P_2S_5 binary SEs were initially received great attention as promising candidate. Several compositions of Li-P-S were discovered, which depends on the ratio of Li_2S and P_2S_5 and heat-treatment condition.[68-71] While the crystal Li-P-S such as ($Li_4P_2S_6$) have low ionic conductivity of 10^{-7} S cm^{-1}, some highly conductive metastable phases could be precipitated in glass phases during heat-treatment temperature, thereby increasing ionic conductivity. These meta-stable phases could be obtained by only heat-treatment of glass phases not a conventional solid-state method. Li_7P_3S11 is a representative case for highly conductive glass-ceramic SE, showing ionic conductivity of over 10^{-3} S cm^{-1}. Also, meta-stable β-Li_3PS_4 was also reported.[72]

Kanno and co-workers have found the $Li_{10}GeP_2S_{12}$ (LGPS) and their derivatives showing high ionic conductivity of over 10^{-2}, which is similar to those of conventional LEs.[31] LGPS was derived from (1-x)Li_4GeS_4-xLi_3PS_4 systems. Despite of high ionic conductivity, high cost of Ge and poor electrochemical stability (especially at low voltage) are major drawbacks of LGPS for practical

application. More recently, Y. Kato and co-workers reported the Ge-free $Li_{9.54}Si_{1.74}P_{1.44}S_{11.7}Cl_{0.3}$, showing the highest ionic conductivity of 2.5×10^{-2} S cm^{-1} among reported SEs.[25]

Li argyrodites, Li_6PS_5X (X = Cl, Br, I), are another promising sulfide SEs owing to high ionic conductivity, moderate electrochemical stability for both cathodes and anodes, relatively cheap precursors, and wet-processability. Deiseroth and co-workers firstly reported the Li argyrodite (Li_6PS_5Cl, Li_6PS_5Br, Li_6PS_5I).[73] The ionic conductivities are highly affected by type of halogen ions, which is related with S^{2-}/X^- site disorder. In contrast to Li_6PS_5Cl and Li_6PS_5Br, the Li_6PS_5I shows low ionic conductivity of 10^{-7} S cm^{-1}, which is attributed to large ionic radius of I^- than S^{2-}. More recently, W. Zeier and co-workers reported the iodine containing argyrodite by substituting P^{5+} with Ge^{4+} having larger ionic radius.[34] This induced the site disorder of S^{2-}/I^-, achieving high ionic conductivity of 5.4×10^{-3} S cm^{-1}. The halogen rich argyrodite, $Li_{5.5}PS_{4.5}Cl_{1.5}$, is also reported, showing the ionic conductivity of 9.4×10^{-3} S cm^{-1}.[33]

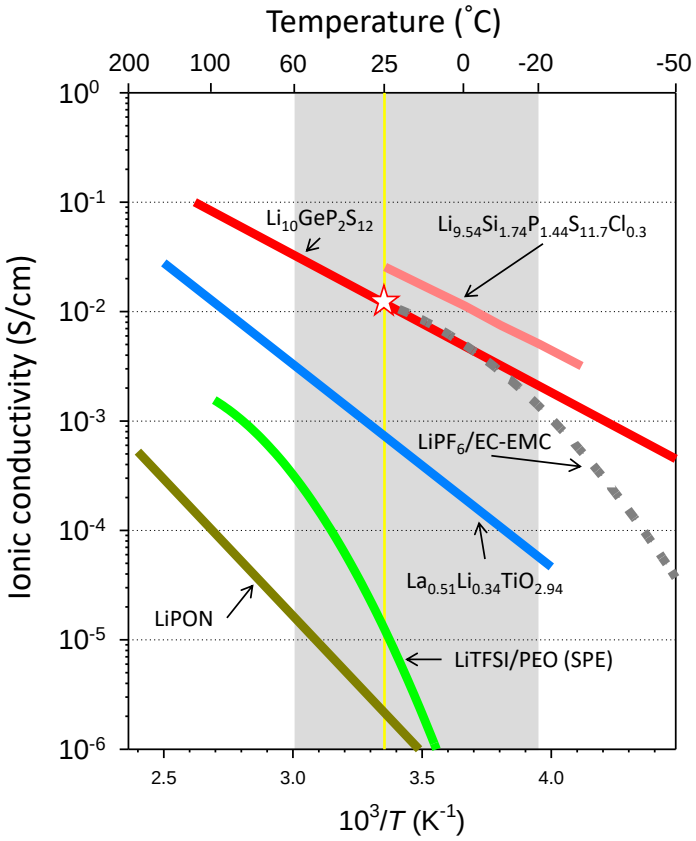

Figure 3. Arrhenius plots of Li-ion conductivities for the representative SE materials. The gray region indicates the temperature range where liquid electrolytes are stable or work. Reproduced with permission.[30] Copyright 2018, Wiley-VCH.

2.2.2 Electrochemical stability of sulfide solid electrolytes

In addition to ionic conductivities of SEs, electrochemical stability within the operating voltage range is highly important. However, in contrast to common expectation that inorganic SEs have wide electrochemical windows compared to that of LEs, recent work based on theoretical calculations showed that the electrochemical stability of inorganic SEs are overestimated (Figure 4).[30, 74] Especially, most of sulfide SEs have very narrow intrinsic electrochemical stability windows (1.7–2.5 V vs. Li/Li^+), which originated from the high reduction potential of P^{5+} and low oxidative potential of S^{2-} in the thiophosphate compounds. This means that sulfide SEs are not thermodynamically stable in the operating voltage ranges of common electrode materials and decomposition of SEs may not be prevented. Whether the decomposition products are electronically conductive or not affects to continuous degradation of SEs. Ionically conducting but electronically insulating properties is desirable, which is similar to stable SEI layers in conventional LIB electrodes. In contrast, mixed ionic and electronic conducting (MIEC) interfacial layer could propagate continuous decomposition of SEs.[30]

Common layered oxide materials ($LiMO_2$) were generally used for cathode for ASLBs. However, the operating voltage of these cathode exceeds the anodic limit of sulfide SEs, resulting in formation of electronically insulating decomposition products.[74-76] However, in terms of compatibility with electrode materials, the reaction between cathode and SEs are also critical for electrochemical performance. It is generally known that reaction of Li thiophosphate SEs with $LiCoO_2$ is highly favorable, forming electronically conductive cobalt sulfide.[75] Complementary analyses demonstrated the formation of MIEC interphase layers by interdiffusion of Co, P and S, which affect to continuous capacity fading of ASLBs. As in the case of conventional LIBs, introduction of protective layers such as $LiNbO_3$, Li_3BO_3-Li_2CO_3 has been suggested for $LiCoO_2$, demonstrating improved electrochemical performance compared to pristine one.[77]

With respect to anode-SE interface, many studies have been focused on compatibility of SEs with Li metal. It depends on the cation chemistries such as Ti, Ge, which generates different interphase layers. compatibility with electrode materials such as $LiMO_2$ (M = Ni, Co, Mn) and Li metal. Lithium thiophosphate SEs were reduced into Li3P, and Li2S, which is electronically insulating, thereby preventing further decomposition of SEs. In contrast, Li10GeP2S12 showed different behaviors, which is attributed Ge reduction. During lithiation, Li-Ge alloying reaction take place at < 0.6 V, which generate the MIEC interphase layer. The layer propagates the growth of interphase layers, thereby increasing cell resistance.[30]

Recently, the halide- and hydride-based SEs have been reported, having excellent oxidative and reductive stability, respectively.[78-79] In contrast to conventional LIBs, multilayered SE layers could be enabled in all-solid-state cells. Thus, designing SE layers should not be overlooked.[80]

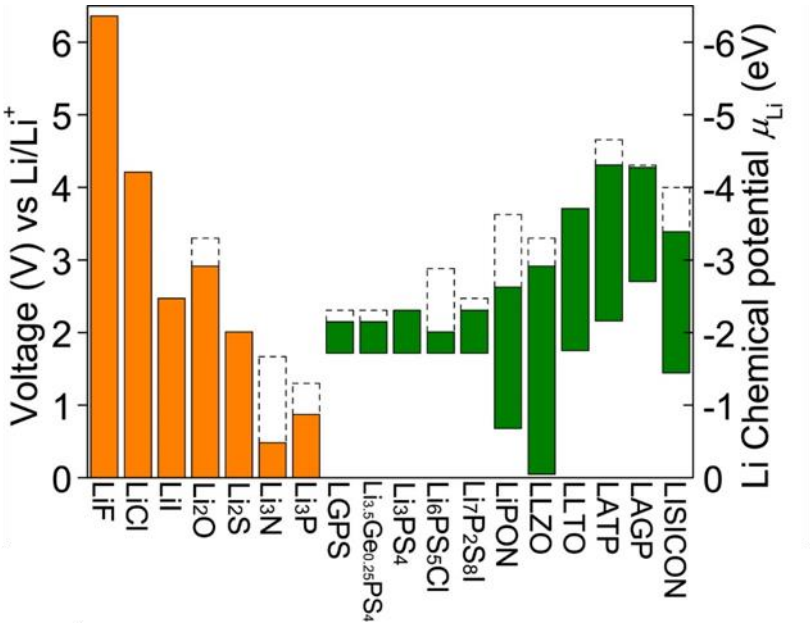

Figure 4. Electrochemical window (solid color bar) of solid electrolyte and other materials. The oxidation potential to fully delithiate the material is marked by the dashed line. Reproduced with permission.[74] Copyright 2015, the American Chemical Society.

2.2.3 Wet-process for sulfide solid electrolytes

To date, sulfide SEs have been synthesized by solid-state method such as mechanical milling or dry-mixing of precursors, followed by high temperature heat-treatment (Figure 5).[30] While the highly conductive sulfide SEs were obtained by solid-state syntheses, it suffers from poor scalability and inhomogeneous size and morphology of SEs. Moreover, traditional mechanical-milling requires a lot of processing time and effort. In these regards, development of wet-process for sulfide SEs is getting great attention. However, until 2012, there have been limited candidates which could be synthesized by wet-process due to the poor chemical stability of sulfide materials with polar solvent.[30]

The wet-process of sulfide SEs mainly divided into liquid-phase synthesis and solution process. In liquid-phase synthesis, precursors (Li_2S and P_2S_5) were dispersed in proper solvents such as acetonitrile (ACN), tetrahydrofuran (THF), dimethoxyethane (DME) and ethyl acetate.[30, 37, 81] Rather than dissolution of precursors, the complexed was formed such Li_3PS_4·THF (Figure 5). Evaporation of solvent and further heat-treatment is carried out to obtain SEs. From liquid-phase synthesis, thiophosphate SEs have been prepared such as Li_3PS_4, and $Li_7P_3S_{11}$ using various solvents.[38-40] Moreover, new metastable sulfide SEs, $Li_7P_2S_8I$, which could not be synthesized by solid-state synthesis, were obtained.[39] Recent works also reported the synthesis of lithium argyrodite SEs (Li_6PS_5X (X = Cl, Br, I)) by two-step process, achieving the ionic conductivity of over 10^{-3} S cm^{-1}.[82-83] Liquid-phase synthesis is advantageous for reducing processing time and control the particle size and morphologies compared to conventional solid-state synthesis. The smaller particle size is desirable to minimize the fraction SEs in electrodes and improving contact area with active materials. For liquid-phase synthesis, selection of proper solvent is highly important.[81] However, there are only limited solvent and precursors (mostly Li_2S and P_2S_5) until now. Exploration of solvent which could dissolve various metal sulfide such as GeS2, SnS2, SiS_2, and Sb_2S_3 is required. Furthermore, elucidating the reaction mechanism is also necessary to design new, highly conductive solid electrolytes using liquid-phase synthesis.

In case of solution process, it is based on dissolution-precipitation procedure. The as-prepared SEs (not precursors) were dissolved in polar solvent such as methanol, and ethanol by forming homogeneous SE solution (Figure 5). Li_4SnS_4 and Li_6PS_5X are representative cases for solution-processable Li SEs.[36, 42] Both SEs are well soluble in MeOH, and EtOH, respectively. Considering the reactivity of PSx with EtOH, it is surprising that Li_6PS_5Cl is dissolved in EtOH. It is attributed to the interaction between Li_2S and EtOH mitigate the hydrolysis reaction of PS_x in Li_6PS_5X in EtOH.[30] After evaporation of solvent, further heat-treatment is carried out to remove solvent completely and to crystallize SEs. The unique advantage of solution process compared to previous liquid-phase synthesis is its homogeneity. While the ionic conductivities of solution processed SEs were lower than those of SEs prepared by solid-state synthesis, SE solution is similar to the liquid electrolytes in conventional LIBs, expecting the formation of intimate ionic contacts with active materials. Recent works demonstrated the direct SE coating on active materials using Li_4SnS_4-LiI in MeOH solution. Despite the lower ionic conductivities of Li_4SnS_4-

LiI (~0.4 mS cm^{-1}) than $Li_{10}GeP_2S_{12}$ (6.0 mS cm^{-1}), electrochemical performance was greatly improved (especially rate capabilities), which is attributed to high surface coverage of SEs on active materials.[36] This result emphasizes the importance of ionic contacts as well as ionic conductivities. The Li^+ conductivities of solution-processed SE with variation of heat-treatment temperature is shown in Figure 6 and most of SEs exhibited the ionic conductivities of below 10^{-3} S cm^{-1}. Formation of organic impurities may affect to ionic conductivities of SEs after solution process, which require high-temperature heat-treatment.[83-84] Reducing impurities and lowering heat-treatment temperature is crucial for considering the compatibility with electrode components and large-scale fabrication.

Overall, the wet-process showed exceptional advantages compared to conventional solid-state synthesis such as scalability, obtaining new composition of SEs, and intimate ionic contacts with active materials. Exploration of various solvents and optimization of wet-process could lead to further development of wet-process of sulfide SE.

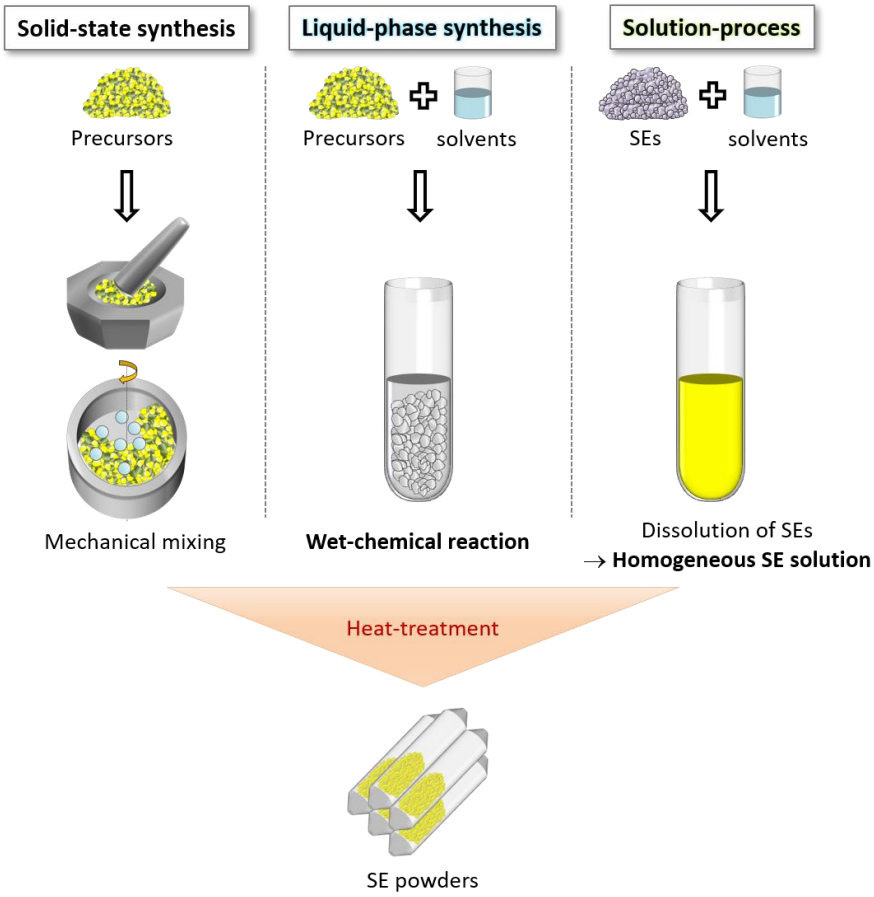

Figure 5. Schematic diagram illustrating preparation of sulfide SE materials by the conventional solid-state methods, the liquid-phase synthesis, and the solution process. Reproduced with permission.[30] Copyright 2018, Wiley-VCH.

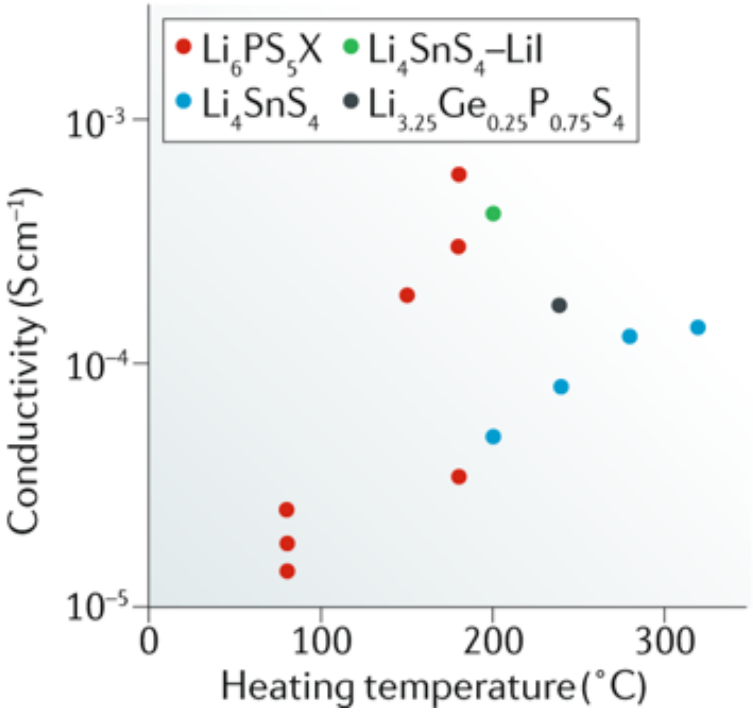

Figure 6. Heating temperatures of dissolution–precipitation processes and corresponding conductivities (near room temperature) of precipitated electrolytes. Reproduced with permission.[37] Copyright 2019, Nature Publishing Group

3. Experimental

3.1 Preparation of materials

The $Li_6PS_5Cl_{1-x}Br_x$ powders were prepared by ball-milling a stoichiometric mixture of Li_2S (99.9%, Alfa Aesar), P_2S_5 (99%, Sigma-Aldrich), LiCl (99.99%, Alfa Aesar), and LiBr (99.9%, Alfa Aesar) at 600 rpm for 10 h at room temperature with ZrO_2 balls. Ball-milled Li_6PS_5Cl (LPSCl) and $Li_6PS_5Cl_{0.5}Br_{0.5}$ (LPSClBr) are referred to as "BM-LPSCl" and "BM-LPSClBr", respectively. The homogenous SE solution was prepared by dissolving ball-milled $Li_6PS_5Cl_{1-x}Br_x$ powders in anhydrous EtOH (99.5%, Sigma-Aldrich), at a concentration of 100 mg mL^{-1} (for electrodes) or 150 mg mL^{-1} (for SE membranes), and then used for infiltration process. After evaporating the EtOH under vacuum at room temperature, heat-treatment was performed at 80 to 550 ℃ for 6 h to obtain solution-processed $Li_6PS_5Cl_{1-x}Br_x$ powders, which are referred to as "Sol-LPSCl (for Li_6PS_5Cl (x = 0.0))". Crystalline Li_6PS_5Cl powders were prepared by heat-treating a stoichiometric mixture of Li_2S, P_2S_5, and LiCl at 550 °C for 10 h in a quartz ampoule sealed under vacuum and used for slurry process or SE layers in all-solid-state cells. Li_4SnS_4 powders were prepared by heat-treatment of a stoichiometric mixture of Li_2S and SnS_2 (99.999%, American Elements) powders at 450 °C in a vacuum-sealed quartz ampoule. The $0.4LiI\text{-}0.6Li_4SnS_4$ solution was prepared by dissolving a stoichiometric mixture of Li_4SnS_4 and LiI (99.95%, Alfa Aesar) into anhydrous MeOH (99.8%, Sigma-Aldrich). Li_3PS_4 (LPS) powders with conductivity of 1.0×10^{-3} S cm^{-1} at 30 °C were prepared by ball-milling a stoichiometric mixture of Li_2S and P_2S_5 powders at 500 rpm for 10 h with ZrO_2 balls and subsequent heat-treatment at 243 °C for 1 h in a vacuum-sealed glass ampoule. $Li_{10}GeP_2S_{12}$ (LGPS) powders with a conductivity of 6.0×10^{-3} S cm^{-1} at 30 °C were prepared by heat-treatment of a stoichiometric mixture of Li_2S, P_2S_5, and GeS_2 (99.9%, American Elements) powders at 550 °C for 10 h in a quartz ampoule sealed under vacuum. As a polymer scaffolds for SE membranes, porous polyimide (PI) was fabricated by imidization of polyamic acid (PAA) synthesized by using pyromellitic dianhydride (PMDA, 97% Sigma Aldrich) and 4,4'-oxydianiline (ODA, 97% Sigma Aldrich) monomers. The PAA precursor was synthesized through polymerization of PMDA and ODA monomers (equimolar ratio) with dehydrated dimethylacetamide (DMAc) at 0 °C. After reacting for 4 h, the transparent PAA solution was obtained and used for electrospinning. For preparation of polyetherimide (PEI), a 23 wt% of PEI solution was prepared by dissolving the PEI (Ultem 1000) in a solvent mixture of DMAc/N-methyl pyrrolidone (NMP) = 1/1 (w/w) at 70 °C for 12 h. The PAA and PEI membranes were obtained by electrospinning technique using each solution. The detailed experimental conditions of electrospinning were 13 kV with a feed rate of 3.5 uL min^{-1} (for PAA) and 15 kV with a feed rate of 4.5 uL min^{-1} (for PEI) at a distance of 15 cm from the nozzle. The as-prepared PAA was imidized with stepwise thermal curing process in N_2 gas conditions: (i) at 60 ºC for 30 min, (ii) at 120 ºC for 30 min, (iii) at 200 ºC for 1 h, (v) at 300 ºC for 1 h,

(iv) at 400 ºC for 10 min.

3.2 Preparation of electrodes and solid electrolyte membranes

The conventional LIB composite electrodes used for the infiltration of solution-processable SEs were prepared by casting and spreading slurries on current collectors (Al for $LiCoO_2$ (LCO) and Ni foil for graphite (Gr) and Si electrodes), followed by drying at 120 °C in a convection oven. The slurries were prepared by mixing of active materials (LCO, Gr, micro-Si (10 μm, Shandong), nano-Si (< 50 nm, Alfa Aesar)), polymeric binders (polyvinylidene fluoride (PVDF, KF1100, Kureah Inc) or PAA/CMC (50/50 wt %, Aldrich)), and carbon additives (Super P) in NMP (for PVDF) or water (for PAA/CMC) as solvent. The mass loadings of active materials were 10 mg cm^{-2} for LCO, 6 mg cm^{-2} for Gr, and 0.8–1.2 mg cm^{-2} for Si, respectively. $LiNbO_3$ (0.3 wt.%) was coated on LCO powder by the wet-chemical method, before using the electrodes. x The infiltration of conventional composite electrodes with SEs was carried out by dipping the as-prepared electrodes into the SE solution, followed by drying in an Ar-filled glove box and subsequent heat-treatment at 180 °C under vacuum. Porosity was obtained for three kinds of electrodes; i) before the SE-infiltration, ii) after the SE-infiltration, iii) after the SE-infiltration, followed by the cold-pressing under 770 MPa or the hot-pressing under 460 MPa at 150 °C using a custom-made hot-pressing tool. Mixture electrodes were prepared by manual mixing of active materials (LCO or Si), SEs, carbon additives, and (PVDF) under dry conditions (dry-mixed electrode) or by casting slurries, which consist of active materials (LCO), SEs, carbon additives, and nitrile-butadiene rubber (NBR), on Al current collector (slurry-processed electrode). The Al_2O_3 ALD films were grown directly on the as-formed LCO electrodes at 180 °C by using trimethylaluminum (TMA, 97%) and H_2O as the precursors, as described in previous reports.x For SE membranes, infiltration of LPSClBr was carried out by dropping SE solution onto PI or PEI. After evaporation of solvent in Ar-filled glove box, heat-treatment was performed at 400 ℃ in Ar atmosphere for PI and 180 ℃ under vacuum for PEI. These resulting SE membranes were referred to as “PI-LPSClBr” and “PEI-LPSClBr”, respectively. Before preparation of oxide-polymer electrolytes (OPCs), all precursors were dried under vacuum. Lithium bis(trifluoromethanesulfonyl)imide (LiTFSI, 99.95%, Sigma-Aldrich), poly(ethylene oxide) (PEO, Mw ≈ 600,000, Sigma-Aldrich), Al_2O_3 (< 50 nm, Sigma-Aldrich) were added into acetonitrile (99.8%, Sigma-Aldrich), followed by mechanical stirring at 50 ℃ for 10 h. The [EO]/[Li] ratio is 16:1 and weight fraction of Al_2O_3 in total amount of PEO and LiTFSI is 10 wt %. The mixture was casted on PTFE plate using doctor blade, followed by drying at 50 ℃. Further heat-treatment was carried out at 60 ℃ for 5 h under vacuum to remove solvent completely. The composite electrodes for ASLBs were fabricated by wet-slurry process. The slurries were prepared by mixing active materials ($LiNi_{0.6}Co_{0.2}Mn_{0.2}O_2$ (NCM622) or Gr or $Li_4Ti_5O_{12}$ (LTO)), LPSClBr, NBR, and carbon additives (only for NCM622 and LTO) in anhydrous o-xylene (or dibromomethane (DBM) for LTO). For LTO electrode,

small amount of solvate ionic liquid (equimolar mixture of LiTFSI and G3 (triglyme), LiG3) was added. The compositions of electrodes were 70 : 27.5 : 1.0 : 1.5, 58.6 : 39.1 : 1.5 : 0.0, and 49.1 : 45.1 : 1 : 1.5 : 3.5 (LiG3) for NCM622, graphite, and, LTO, respectively. The slurry mixtures were casted on current collectors (Al and Ni foil (only for graphite) using doctor blade, followed by heat-treatment at 120 ℃ (or 60 ℃ for LTO) under vacuum. The mass loadings of active materials were 8.5 mg cm^{-2}, 6.0 mg cm^{-2}, and 12.6 mg cm^{-2} for NCM, graphite, and LTO, respectively. The conventional LIB electrodes used for SE injection process also fabricated by same slurry process. The slurries were prepared by mixing of active materials ($LiCoO_2$ (LCO) or LTO), PVDF, carbon additives with weigh fraction of 97 : 1 : 2 and 80 : 10 : 10 for LCO and LTO, respectively. The as-prepared electrodes were assembled with PI, forming LCO/PI/LTO assembly, and then used for SE injection process.

3.3 Materials characterization

Raman spectra were measured with a 532 nm ND-YAG laser using an Alpha300S (Witec Instruments). For XRD measurements, SE powders or composite electrodes were sealed with a beryllium window and mounted on a MiniFlex600 diffractometer (Rigaku Corp.) (Cu Kα radiation of 1.54056 Å) at 15 mA and 40 kV. Fourier transform infrared spectroscopy (FTIR) spectrum was collected using Bruker Alpha FTIR spectrometer with ATR mode between 4000 and 500 cm^{-1}. Thermogravimetric analysis (TGA) experiment was carried out from 25 to 400 or 800 °C at 10 °C min^{-1} under Ar using a Q50 (TA Instrument Corp.). Cross-sections of surfaces of the electrodes and SE membranes were prepared by polishing at 5 kV with an Ar ion beam (JEOL, IB-19510CP). The field-emission scanning electron microscopy (FESEM) images and the corresponding energy dispersive X-ray spectroscopy (EDXS) elemental maps of cross-sectioned electrodes were obtained using a JSM-7000F (JEOL). The high-resolution transmission electron microscopy (HRTEM) images and the corresponding EDXS elemental maps were obtained using JEM-2100F (JEOL) after sectioning with a 30 keV Ga^+ ion beam. For FESEM and HRTEM measurements, the SE-infiltrated composite electrodes and SE membranes were densified by pressing under 770 MPa or 520 MPa, respectively, at RT.

3.4 Electrochemical characterization

The Li^+ conductivity was measured by AC impedance method using a Li-ion blocking Ti/(SE pellet or SE membrane)/Ti symmetric cells. Both SE powder and SE membrane were cold-pressed at 370 MPa and at RT. The electronic conductivity of SE membrane was measured by DC polarization method using Ti/SE membrane/Ti symmetric cells. All-solid-state half-cells that employed Li-In alloy (a nominal composition of $Li_{0.5}In$) as the counter and reference electrode were fabricated as follows. After forming an SE layer by cold-pressing SE powders (150 mg of LPSCl or LGPS/LPS or LPS), the electrodes (the SE-infiltrated, dry-mixed or slurry-mixed electrodes) were put on one side of the formed SE layer (on the LGPS side in the case of a LGPS/LPS bilayer). Then, $Li_{0.5}In$, which was prepared by mixing Li

(FMC Lithium Corp.) and In (99%, Sigma-Aldrich) powders, was spread on the other side SE layer, followed by pressing at 370 MPa. The galvanostatic charge-discharge cycling of the all-solid-state LCO and Gr half-cells was carried out in a voltage range of 3.0–4.3 V (vs. Li/Li^+) and 0.005–2.0 V (vs. Li/Li^+) at 30 °C, respectively. For Si/Li-In half cells, the galvanostatic charge-discharge was carried out in a voltage range of 0.005–1.5 V (vs. Li/Li^+) for the first cycle and 0.01–1.2 V (vs. Li/Li^+) for subsequent cycles at 30 °C. For self-discharge experiments, Si/Li-In half cells were cycled once and discharged to 0.01 V (vs. Li/Li^+). Then, the cells were kept for 7 days at 30 °C, followed by de-lithiation (charge). The all-solid-state full cells were prepared by putting the electrodes on each side of the SE layer, followed by pressing at 370 MPa or 770 MPa. For the SE layer, either a conventional thick (~600 μm) SE layer (150 mg of LGPS/LPS or LPS) or thin SE membranes (SE-NW (~70 μm), PI-LPSClBr (~40 μm), or PEI-LPSClBr (~40 μm)) were used. The SE-NW composite film (LPS-NW-LPS) was fabricated by slurry casting of the LPS suspension on a Ni foil, followed by transferring to NW scaffold by cold-pressing. The np ratio was approx. 1.3 and 1.7 for LCO/Gr and LCO/Si, respectively. The all-solid-state LCO/Gr full cells were cycled in voltage range of 2.0–4.3 V or 2.0–4.2 V. Before cycling at 100 °C, the LCO/Gr full cell was charged/discharged once at 0.1C (0.14 mA cm^{-2}) and 30 °C. The LCO/Si full cell was cycled in a voltage range of 2.8–4.2 V at 30 °C. For NCM622/Gr and NCM622/LTO full cells, galvanostatic cycling tests were carried out at 30 °C in a voltage range of 2.0–4.2 V and 1.3–2.7 V, respectively. The LCO/LTO full cells prepared by SE injection process was cycled in voltage range of 1.3–2.7 V at 70 °C. The external pressure (140 MPa, 70 MPa, 20 MPa, or 5 MPa) was applied during operation. All the procedures were performed in a polyaryletheretherketone (PEEK) mold (diameter = 1.3 cm) with Ti metal rods as current collectors. The electrochemical impedance spectroscopy (EIS) measurements of LCO/$Li_{0.5}$In half cells were performed from 1.5 MHz to 5 mHz with an amplitude of 10 mV, using the cells discharged to 60 mA h g^{-1} at 0.1C and rested for more than 3 h. The galvanostatic intermittent titration technique (GITT) measurements were carried out with a pulse current of 0.5C (0.7 mA cm^{-2}) for 60 s and rested for 2 h. The surface coverage of SE on the active particles (LCO) was obtained by dividing the apparent surface area of LCO particles (obtained by N_2 adsorption-desorption isotherm) by the contact area between LCO particles and LPSCl (obtained by GITT analysis). For the liquid-electrolyte-cell tests, 2032-type coin cells using Li metal as the counter and reference electrode were used. For LCO/Li coin cells, a solution of $LiPF_6$ (1.0 M) dissolved in a mixture of ethylene carbonate (EC), ethyl methyl carbonate (EMC), and dimethyl carbonate (DMC) (3:4:3 v/v) was used as the electrolyte. Prior to the assembly of Si coin cells, all the Si electrodes were heat-treated at 180 °C under vacuum. For Si/Li coin cells, a solution of 1.0 M $LiPF_6$ in a mixture of EC and diethyl carbonate (DEC) (1:1 v/v) with 10 wt % of fluoroethylene carbonate (FEC) was used as the electrolyte. A porous polypropylene (PP)/polyethylene (PE)/PP tri-layer film (Celgard Inc.) was used as the separator. The specific capacity shown is based on the mass of active materials.

4. Results and discussion

4.1 Infiltration of solution-processable solid electrolytes for sheet-type electrodes

In this section, new facile fabrication protocol for sheet-type ASLB electrodes is developed by infiltrating solution-processable SEs into conventional LIBs electrodes. This alternative protocol takes the advantage of liquefied SEs for achieving favorable ionic percolation and intimate contacts of active materials with SEs. The Li_6PS_5Cl (LPSCl) infiltrated $LiCoO_2$ (LCO) and graphite (Gr) electrodes exhibit the reversible capacities of 140 mA h g^{-1} and 340 mA h g^{-1} at 0.14 mA cm^{-2} for LCO and Gr electrode, respectively. Finally, the promising electrochemical performance of LCO/Gr full cells using SE-infiltrated electrodes is demonstrated not only at 30 °C but also at 100 °C.

4.1.1 Characterization of solution-processable solid electrolytes

Among the solution processable sulfide SEs, the LPSCl/EtOH solution was chosen owing to wide electrochemical window of LPSCl and compatibility of EtOH with Al current collector. The LPSCl, which is prepared by ball milling and referred as "BM-LPSCl", dissolved completely in anhydrous EtOH, forming homogenous SE solution (Figure 7). Solution-processed LPSCl, which is referred to as "Sol-LPSCl", was obtained by evaporation of solvent and further heat-treatment at 180 ºC under vacuum (Figure 7). The X-ray diffraction (XRD) patterns of Sol-LPSCl is well matched with BM-LPSCl without formation of impurity phases (Figure 8a). The Raman spectra for BM-LPSCl and Sol-LPSCl also shows characteristic peaks of PS_4^{3-}, which is main structure unit of LPSCl (Figure 8b).[42] The Li^+ conductivity of Sol-LPSCl, measured by AC impedance using Ti/SE/Ti symmetric cells, was 0.19 mS cm^{-1} at 30 °C and gradually increased as the heat-treatment temperature increased, showing the highest value of 1.0 mS cm^{-1} for the sample heat-treated at 550 °C. The Arrhenius plots for BM-LPSCl and Sol-LPSCl is also shown in Figure 9. At first glance, this behavior may be explained by the enhanced crystallinity of SEs by increasing the heat-treatment temperature. However, the crystallinity effect fails to explain the high ionic conductivity of 1.0 mS cm^{-1} for BM-LPSCl (Table 1). Moreover, ball-milling of Sol-LPSCl heat-treated at 180 °C (BM-Sol-LPSCl) resulted in the enhancement in ionic conductivity (0.43 mS cm^{-1}) despite the lowered crystallinity. TGA results of BM-LPSCl, Sol-LPSCl heat-treated at 180 °C and 550 °C, and BM-Sol-LPSCl are shown in Figure 10. The heat-treatment at 550 °C or the ball-milling process which could generate local heats could be effective in decomposition of organic impurities derived from EtOH. As expected, the Sol-LPSCl (heat-treated at 180 °C) showed the distinctly higher weight loss than others, indicating the largest amount of organic impurities, which implies a correlation between ionic conductivity and organic impurities.[85]

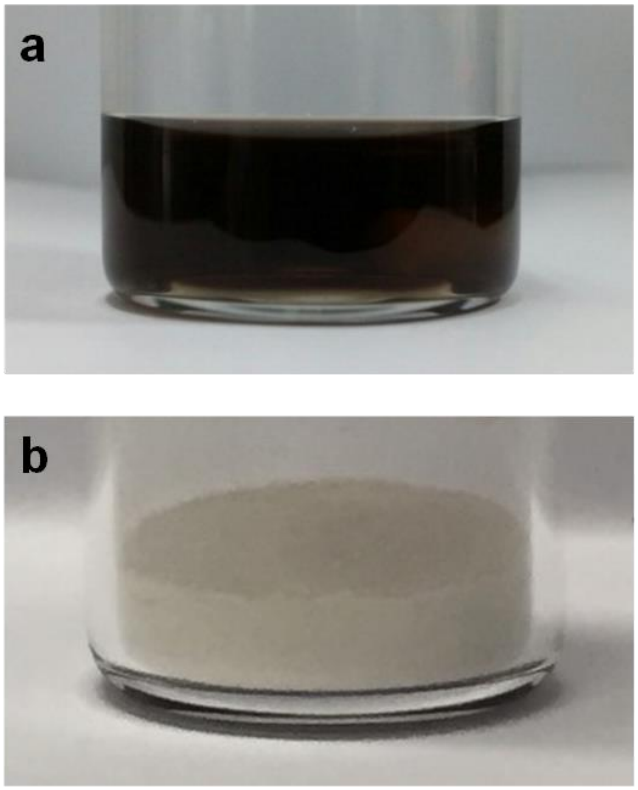

Figure 7. Photographs of a) LPSCl dissolved in EtOH and b) solution-processed LPSCl powders (Sol-LPSCl).

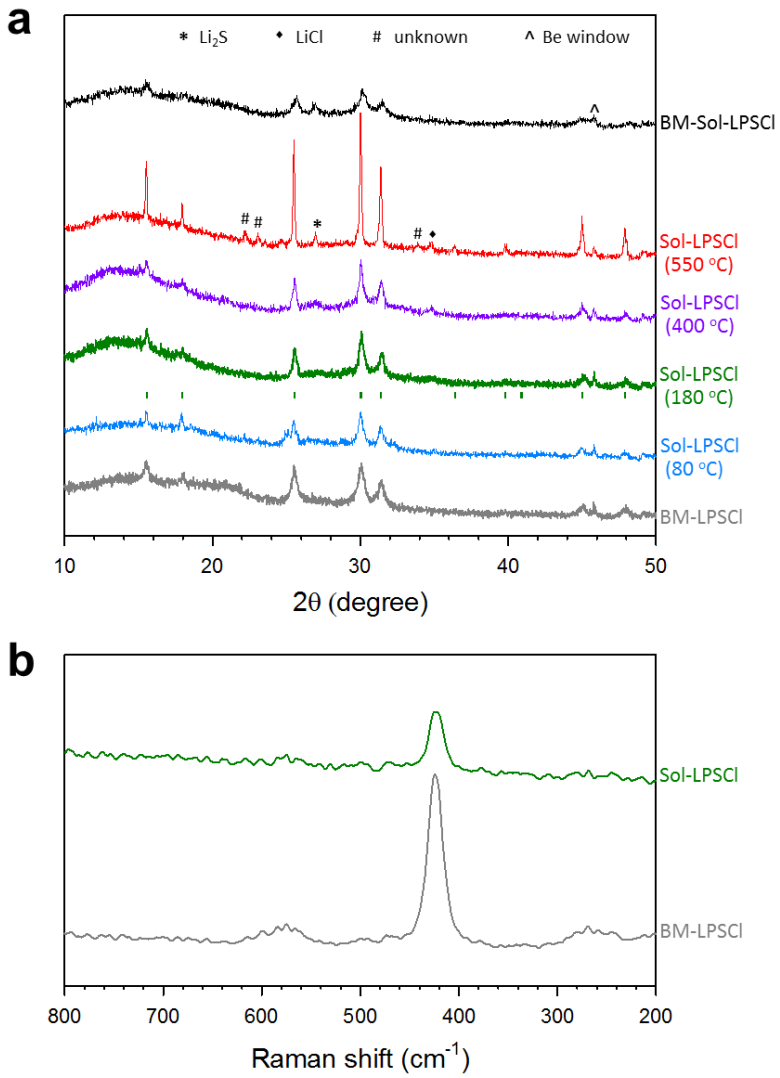

Figure 8. a) XRD patterns of LPSCl prepared by ball-milling (BM-LPSCl), solution-processing using EtOH (Sol-LPSCl) with different heat-treatment temperatures, and ball-milled Sol-LPSCl heat-treated at 180 °C (BM-Sol-LPSCl). b) Raman spectra of BM-LPSCl and Sol-LPSCl (heat-treated at 180 °C). The Bragg position for the argyrodite Li_6PS_5Cl is marked in a).

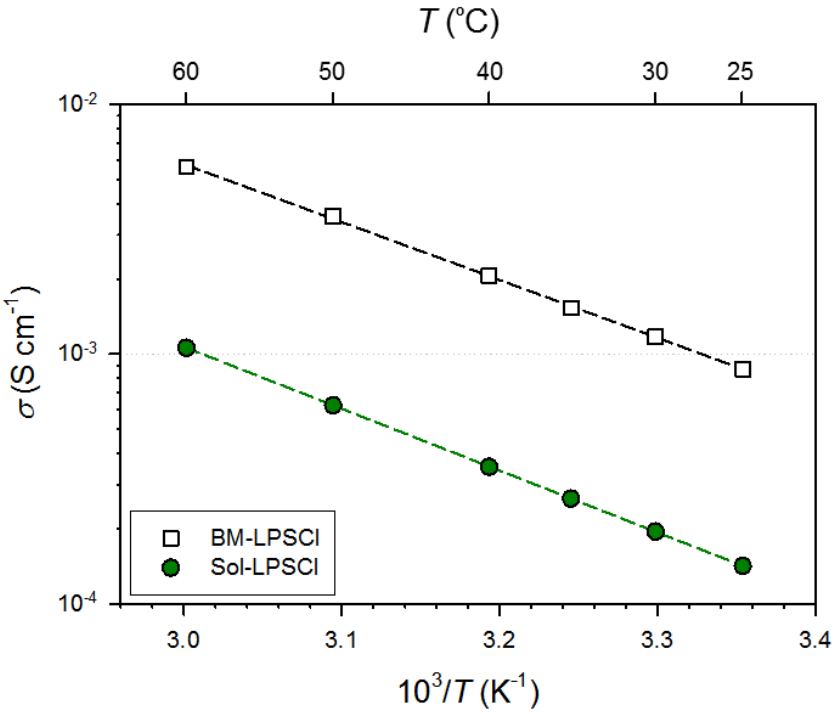

Figure 9. Arrhenius plots of the Li^+ ionic conductivity for BM-LPSCl and Sol-LPSCl.

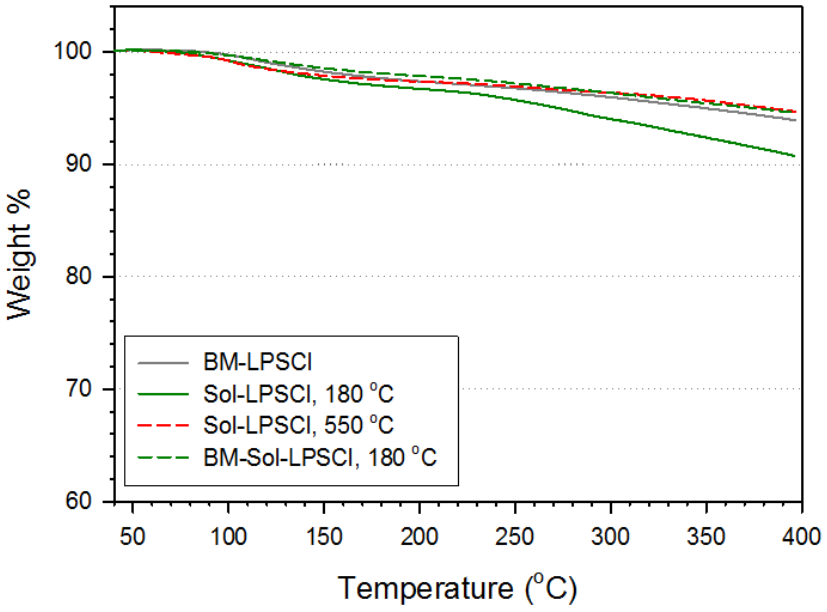

Figure 10. TGA profiles of BM-LPSCl, Sol-LPSCl, and BM-Sol-LPSCl under Ar. The heat-treatment temperatures for preparing Sol-LPSCl are shown.

Table 1. Li^+ ionic conductivities at 30 °C for BM-LPSCl, Sol-LPSCl heat-treated at different temperatures, and BM-Sol-LPSCl.

Sample name	Heat-treatment temperature [°C]	σ_{30} [mS cm^{-1}]
BM-LPSCl	-	1.0
Sol-LPSCl	80	0.010
	180	0.19
	400	0.43
	550	1.0
BM-Sol-LPSCl[a)]	180	0.59

[a)] Prepared by ball-milling Sol-LPSCl heat-treated at 180 °C

4.1.2 Sheet-type $LiCoO_2$ and graphite electrodes

The process for infiltration of solution-processable SEs into conventional composite LIB electrodes is illustrated in Figure 11. The LIB electrodes were prepared by casting slurries on current collectors, followed by drying at 120 °C. The as-prepared electrodes were infiltrated with LPSCl/EtOH solution by a dip-coating method. Evaporation of solvent and further heat-treatment at 180 °C under vacuum caused solidification of LPSCl on any exposed surface of the composite electrodes. The decreased porosity of electrodes after infiltration (prior to cold-pressing; Table 2) demonstrated that liquefied SEs are well penetrated in pores of electrodes. Prior to application to ASLBs, LPSCl-infiltrated electrodes were densified by cold-pressing at 770 MPa for achieving more intimate contact between active materials and SEs. The low porosities of 6–8% were obtained after cold-pressing and negligible porosity was observed after hot-pressing under 460 MPa at 150 °C. It should be emphasized that overall volumetric contribution of SEs and pores was 29–34%, which is comparable to the porosity of commercial LIB electrodes and much lower than previous results for ASLBs.

Porosity values of the electrodes were obtained by the following Equation 1.

$$\text{Porosity [\%]} = 100 - 100\sum(A_i M/\rho_i)/[(\pi/4)\cdot D^2\cdot t] \qquad \text{(Equation 1)}$$

The following values were used for the calculation.

A_i: weight fraction of i in the composite, M: weight of the electrode, D: diameter of the electrode (D = 1.3 cm), t: thickness of the electrode, ρ: apparent density (ρ_{LPSCl} = 1.86 g cm^{-3}, ρ_{LCO} = 5.06 g cm^{-3}, ρ_C = 2.0 g cm^{-3}, ρ_{PVDF} = 1.8 g cm^{-3})

Figure 12 represents the Raman spectra of LCO and Gr electrodes before and after infiltration of LPSCl and shows strong peaks for PS_4^{3-} at 423 cm^{-1} for all electrodes. The characteristic peaks for LCO (A_{1g} and E_g)[86] and graphite (D and G modes)[87] were also observed after infiltration. The XRD patterns of LCO and Gr electrodes before and after infiltration of LPSCl shows signature peaks of LPSCl (Figure 13) and no changes in peak position of LCO and Gr, confirming that both LCO and Gr are compatible with LPSCl solution (Figure 14). Cross-sectional field-emission scanning electron microscope (FESEM) images and their corresponding EDXS elemental maps for LPSCl-infiltrated LCO and Gr electrodes after cold-pressing were shown in Figure 15, and 16. The pores were well filled with SEs, which is excellent penetration of SE solution and deformability of sulfide SEs. The HRTEM image and corresponding EDXS elemental maps for FIB cross-sectioned electrode (Figure 17) confirmed the intimate contacts between LCO and LPSCl at microscopic level, emphasizing the importance of solution-processable SEs.

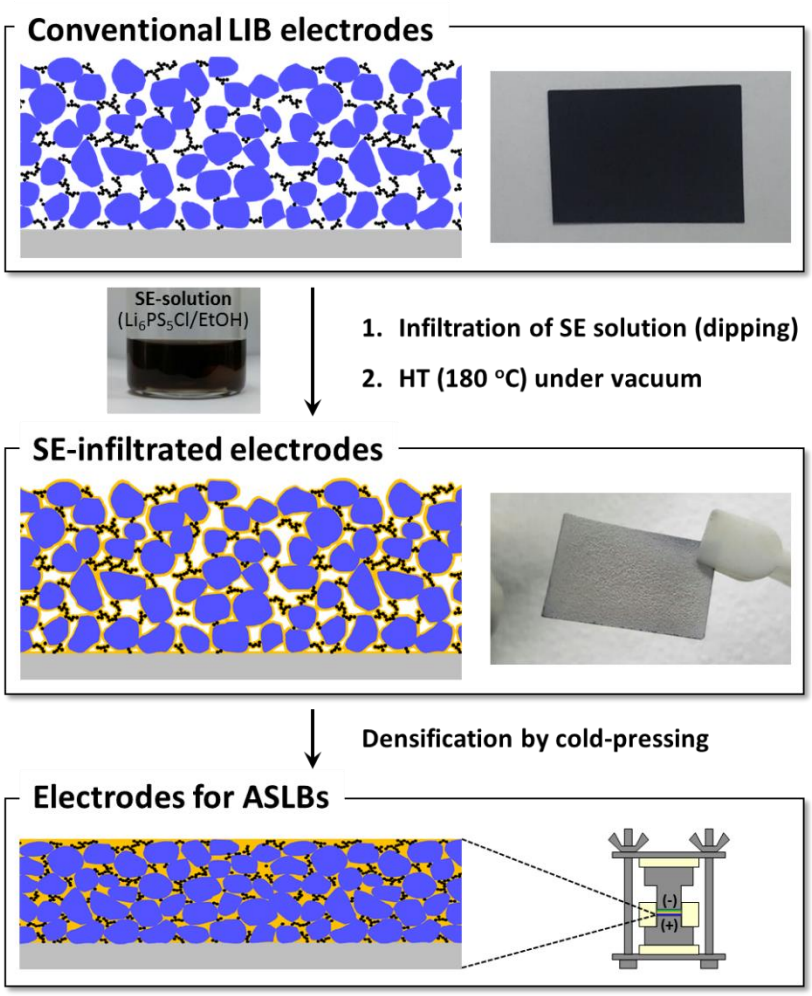

Figure 11. Schematic diagram illustrating the infiltration of conventional LIB composite electrodes with solution-processable SEs. The photographs in the panels show the $LiCoO_2$ electrodes before and after the infiltration of EtOH-solution processed Li_6PS_5Cl (LPSCl). A photograph of LPSCl-dissolved EtOH solution is also shown. Polymeric binders (PVDF) are not shown in the diagram for simplicity.

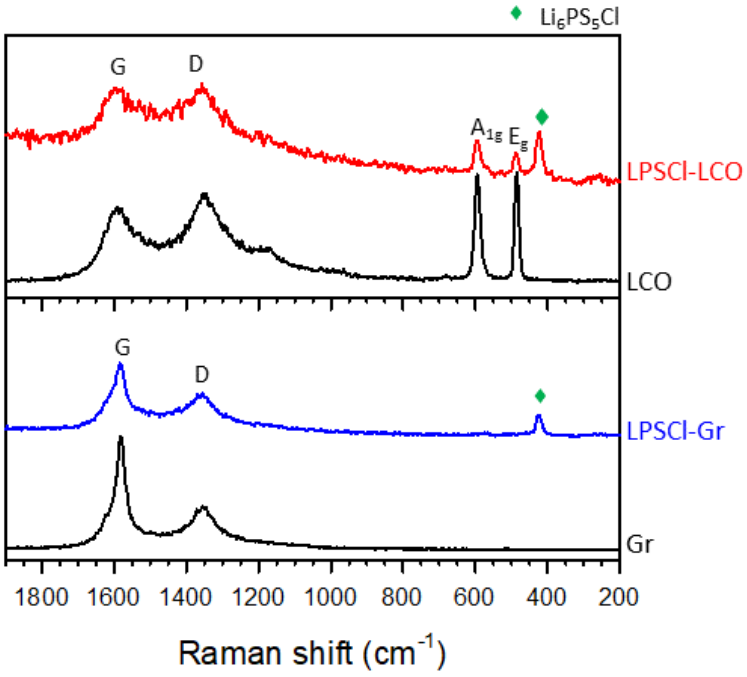

Figure 12. Raman spectra of SE (LPSCl)-infiltrated $LiCoO_2$ (LCO) and graphite (Gr) electrodes.

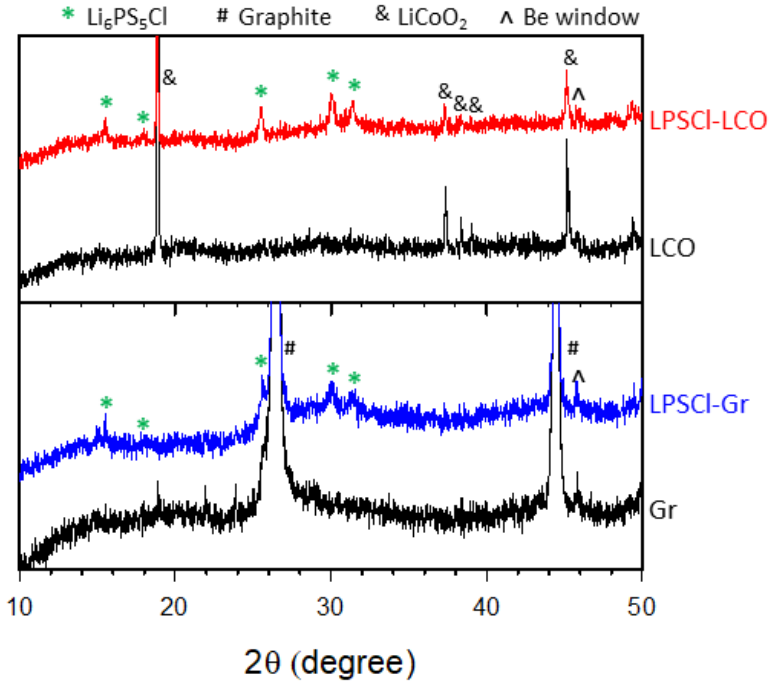

Figure 13. XRD patterns of SE (LPSCl)-infiltrated $LiCoO_2$ (LCO) and graphite (Gr) electrodes.

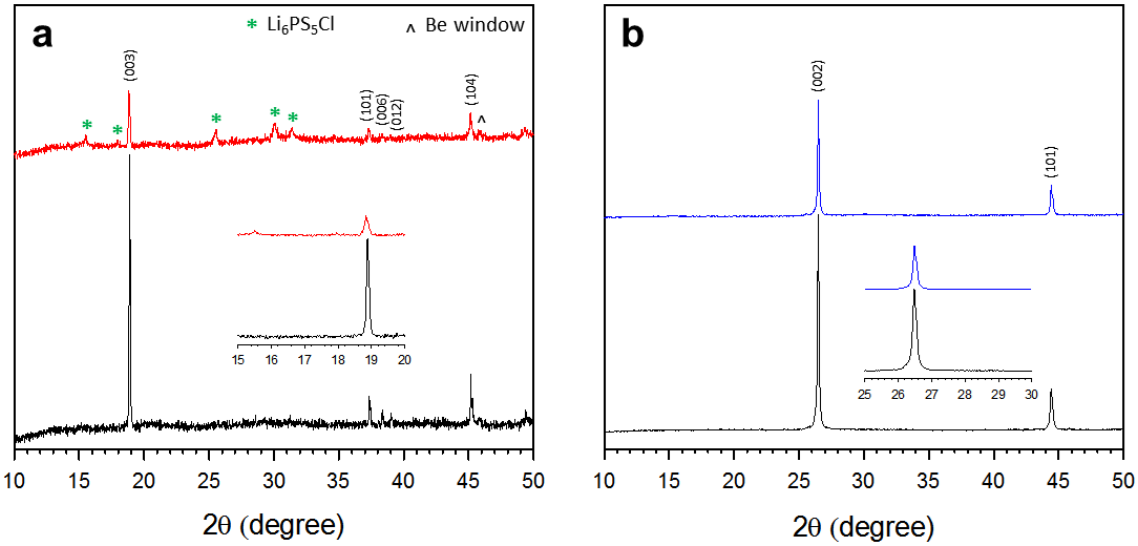

Figure 14. XRD patterns of a) LCO and b) Gr electrodes before and after infiltration with LPSCl. Enlarged views of the main peaks of $LiCoO_2$ and graphite are shown in the insets.

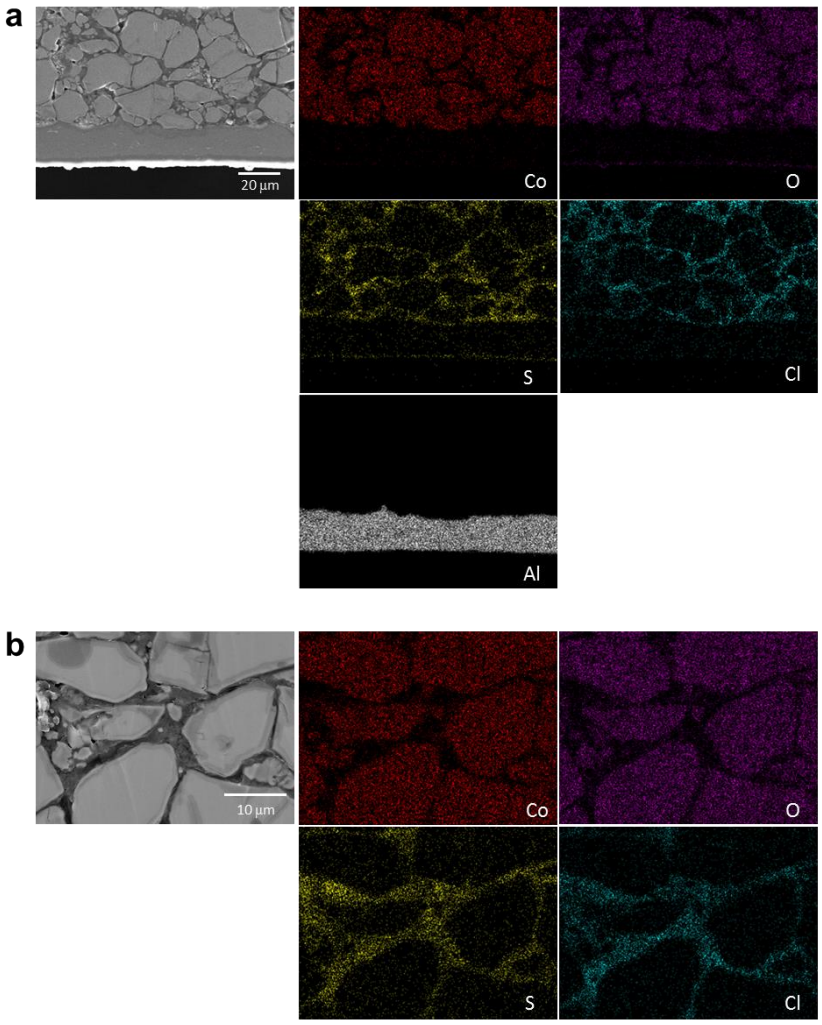

Figure 15. FESEM images of a cross-sectioned LPSCl-infiltrated LCO electrode and its corresponding EDXS elemental maps in a) low and b) high magnification.

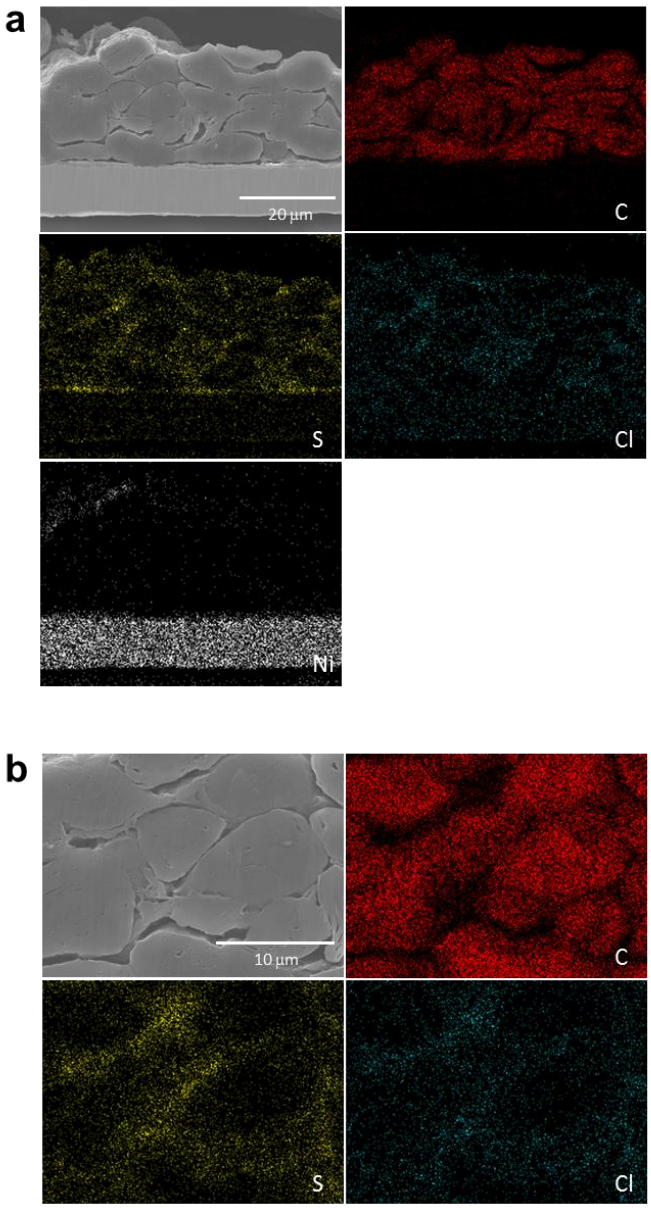

Figure 16. FESEM images of a cross-sectioned LPSCl-infiltrated Gr electrode and its corresponding EDXS elemental maps in a) low and b) high magnification.

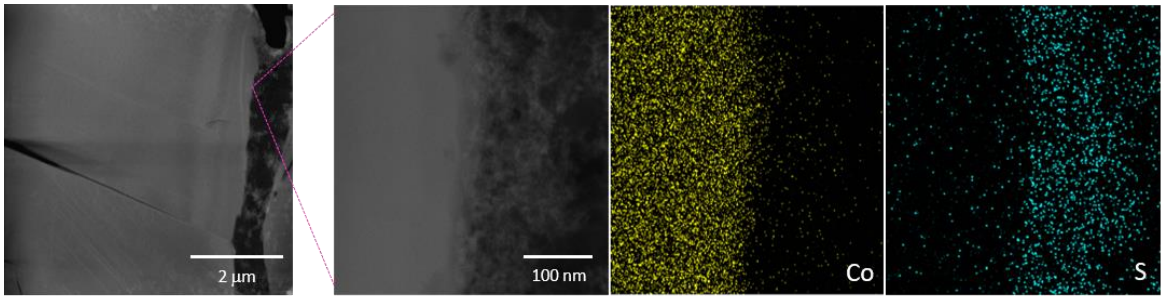

Figure 17. HRTEM images of FIB-cross-sectioned LPSCl-infiltrated LCO electrode and its corresponding EDXS elemental maps

Table 2. Characteristics of LCO and Gr electrodes for the infiltration of SE (LPSCl).

Electrode	Composition [a]	Porosity [%]			Fraction of SE		Surface coverage of SEs onto active materials [%][b]
		Before SE-infiltration	After SE-infiltration		[wt.%]	[vol.%]	
			Before cold-pressing	After cold-pressing			
LCO	96:2:2	54	29	7.3	12	26	56
	97:1:2	52	29	6.7	11	27	61
	98:1:1	53	27	6.3	12	27	65
Gr	95:5:0	50	35	7.1	21	22	-
	92:8:0	48	38	8.0	21	23	-

[a)] Weight ratio of active material : PVDF : super P

[b)] Obtained by GITT analysis

4.1.3 Electrochemical characterization

Electrochemical characterization of LPSCl-infiltrated LCO and Gr electrodes was performed at 30 °C using all-solid-state LCO/Li-In or Gr/Li-In half cells (Figure 18). The LPSCl-infiltrated LCO and Gr electrodes showed reversible capacities of 140 mA h g^{-1} for LCO and 360 mA h g^{-1} for Gr, respectively, which is comparable to liquid electrolyte (LE)-based cells (Figure 18a and 18b). In stark contrast, the all-solid-state cells using LCO electrodes without LPSCl infiltration exhibited negligible capacity (the inset in Figure 18a). It should be noted that specification of electrodes is realistic for practical applications. The mass loadings for the LCO and Gr electrodes were ~10 mg_{LCO} cm^{-2} and 6 mg_{Gr} cm^{-2}, respectively. The fractions of LPSCl were only 11 and 21 wt % for the LCO and Gr electrodes, respectively. These values are much lower than previous results for ASLBs, which fraction of SEs is 30 wt %.[88] The composition and fractions of SEs for the LCO and Gr electrodes were summarized in Table 2. The favorable electrode characteristic such as high capacities, low porosities, and low fractions of SEs demonstrated the competitiveness in volumetric energy density, compared with the conventional LIB electrodes.

The LPSCl-infiltrated LCO electrodes outperformed to dry-mixed electrodes (Mixture1 and Mixture2) and slurry-processed electrode (Mixture3), which is shown in Figure 19. Despite the inclusion of polymeric binders in SE-infiltrated LCO electrode, it exhibited higher capacity (141 mA h g^{-1}) than the Mixture1 electrode which is free from polymeric binders (135 mA h g^{-1}). The superior electrochemical performance of the SE-infiltrated LCO electrodes is attributed to more intimate ionic contacts between LCO and LPSCl enabled by liquefied SEs.[42] The surface coverage of SE on the active materials for the LPSCl-infiltrated LCO electrode, obtained by GITT analysis, was 61%. This value is much greater than conventional dry-mixed electrodes in previous work.[36] The Mixture2 electrode showed lower capacity (118 mA h g^{-1}) than Mixture1 electrode, which is attributed to ionically insulating polymeric binder. In stark contrast, capacity of only 14 mA h g^{-1} was obtained by the Mixture3 electrode, which might be explained by formation of imbalanced ionic and electronic pathways resulting from combined effects of ionically blocking binder and an uneven distribution of the electrode components (active materials, SEs, binder, and carbon additives). These comparisons emphasize the advantage of the infiltration process using solution-processable SEs in terms of intimate ionic contacts and formation of efficient ionic/electronic pathways in electrodes.

The rate capabilities for the LPSCl-infiltrated LCO and Gr electrodes with different compositions are compared in Figure 18c, and 18d. The LCO electrode with composition of 97:1:2 showed better rate capabilities than that of 96:2:2, which is attributed improved ionic contacts between LCO and LPSCl. The higher surface coverage of SEs on LCO for the composition of 97:1:2 (61%), obtained by GITT analysis (Figure 20 and Table 2) supported the enhanced rate performance compared to the composition of 96:2:2 (56%). The same trend was observed for the Gr electrodes (95:5:0 > 92:8:0). While the addition of polymeric binders is imperative for sheet-type electrodes, it is desirable to be used as little

as possible due to ionically insulating property of polymeric binders. While the further increase of surface coverage of SEs was achieved by reducing the amount of carbon additives (98:1:1), rate performance decreased, which is could be attributed to the insufficient electronic pathways in electrodes. Nyquist plots for the LPSCl-infiltrated LCO and Gr electrodes also matched well with the trends for rate performance (Figure 21).

The cycle performances of the LPSCl-infiltrated LCO and Gr electrodes at 30 °C were shown in Figure 22. The capacity retentions for the LCO and Gr electrodes cycled at 0.70 mA cm^{-2} (~0.5C) and 0.28 mA cm^{-2} were 88.6% and 86.1% after 50 and 100 cycles as compared to the capacity at the 3rd cycle, respectively. The LCO electrode (without SE) in conventional LE-based cell exhibited the capacity retention of 97.4% after 50 cycles (Figure 23). It is generally known that sulfide SEs are not thermodynamically stable in contact with LCO, which results in poorer cycling stability of LCO in all-solid-state cells than in the LE-based cell.[74-75] In this regard, a conformal Al_2O_3 coating has been applied for the as-prepared LCO electrode (before SE infiltration) to prevent the interfacial side reactions. As compared to the bare LCO electrode, the Al_2O_3 ALD-coated (~0.6 nm) LCO electrode showed an improved capacity retention of 98.1% after 50 cycles. This preliminary result highlights the importance of elaborative electrode−electrolyte interfacial engineering for ASLBs.[89]

Finally, all-solid-state full cells were assembled employing the LPSCl-infiltrated LCO and Gr electrodes, and their electrochemical performances were shown in Figure 24. The all-solid-state LCO/Gr full cell showed a reversible capacity of 117 mA h g_{LCO}^{-1}, which corresponds to energy density of 279 W h kg_{LCO+Gr}^{-1} at 30 °C. The rate performance and cycling stability of the LCO/Gr full cell at 30 °C also represented in 30 °C (Figure 25). The capacity retention at 1C based on the capacity at 0.1C was 81.7% (0.1C charge) and 51.4% (same charge-discharge rate). The LCO/Gr full cell showed excellent capacity retention of 95.9% as after 79 cycles at 0.5C, as compared to the initial capacity. Instead of the conventional thick SE pellet (~600 μm) (Figure 24a), a bendable and thin SE membrane (SE-nonwoven (NW) composite, ~70 μm) was used as SE layer for the LCO/Gr full cell. The LCO/Gr full cell with SE-NW membrane showed a reversible capacity of 94 mA h g_{LCO}^{-1} at 0.1C in voltage range of 2.0–4.2 V at 30 °C, demonstrating the applicability of roll-to-roll fabrication processes for ASLBs (Figure 24b). Galvanostatic cycling of the LCO/Gr full cell was also performed at 100 °C, which is far beyond the operating temperature range of conventional LIBs (Figure 24c and 24d). The LCO/Gr full cell showed a capacity of 86 and 65 mA h g_{LCO}^{-1} at high rate of 12C and 24C, respectively (Figure 24c). The capacity retention for the LCO/Gr full cell was 82% at 6C after 100th cycle (Figure 24d). The high temperature operation (100 °C) demonstrated excellent thermal stability of ASLBs, which is not possible for carbonate-based LE cells.[18]

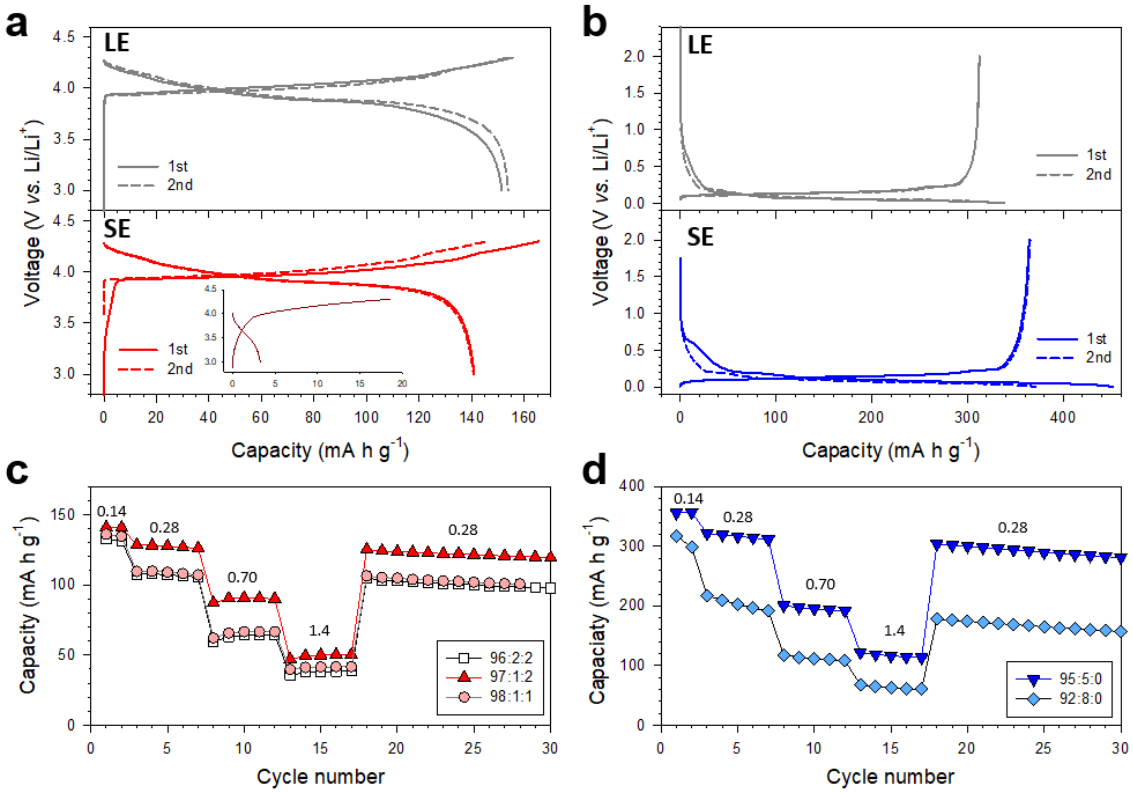

Figure 18. Electrochemical characterization of all-solid-state LCO/Li-In and Gr/Li-In half-cells employing the LPSCl-infiltrated electrodes at 30 ºC. First- and second-cycle charge-discharge voltage profiles of a) LCO and b) Gr electrodes at 0.14 mA cm^{-2} (~0.1C) for liquid-electrolyte (LE) cells and all-solid-state cells. The result for the LCO electrode, which was an all-solid-state cell without infiltration of the SE, is shown in the inset of a). Rate performances of c) LCO and d) Gr electrodes in all-solid-state cells. The numbers indicate the current densities in mA cm^{-2}. The current densities for charge and discharge were the same. The compositions of electrodes in terms of the weight ratio of active material : PVDF : Super P are shown in c-d.

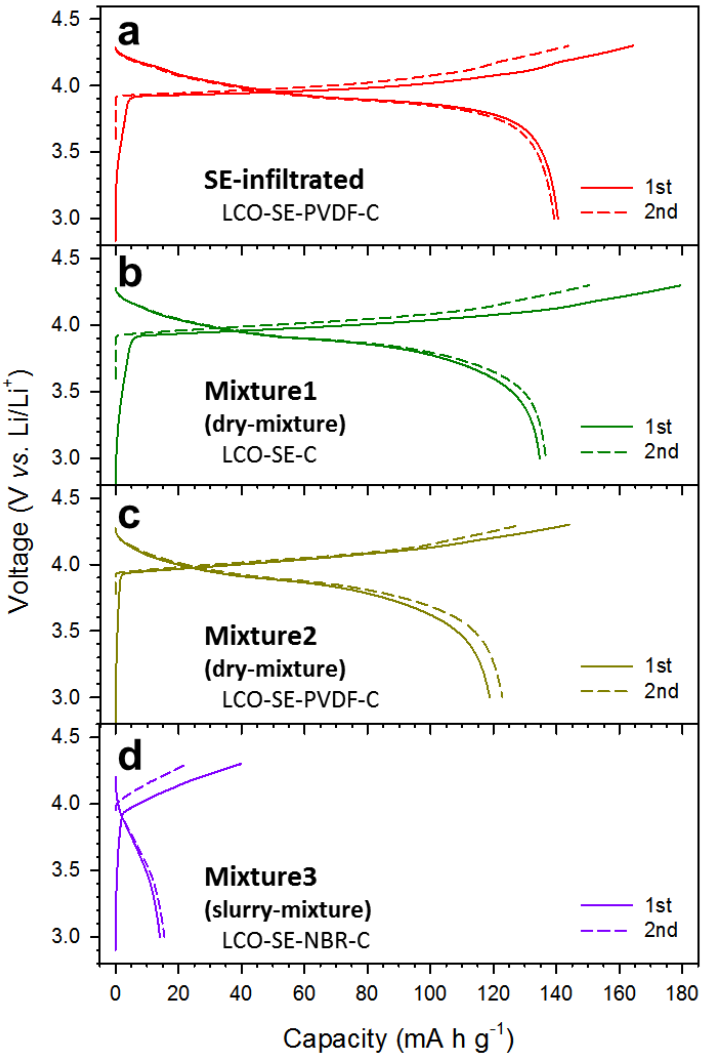

Figure 19. First- and second-cycle charge-discharge voltage profiles of LCO/Li-In all-solid-state cells at 0.14 mA cm^{-2} and 30 ºC, employing a) LPSCl-infiltrated electrode, b) electrode prepared by manual mixing of LCO, SE, and Super P, c) electrode prepared by manual mixing of LCO, SE, PVDF, and Super P, and d) electrode prepared from a slurry consisting of LCO, SE, NBR, and Super P in xylene.

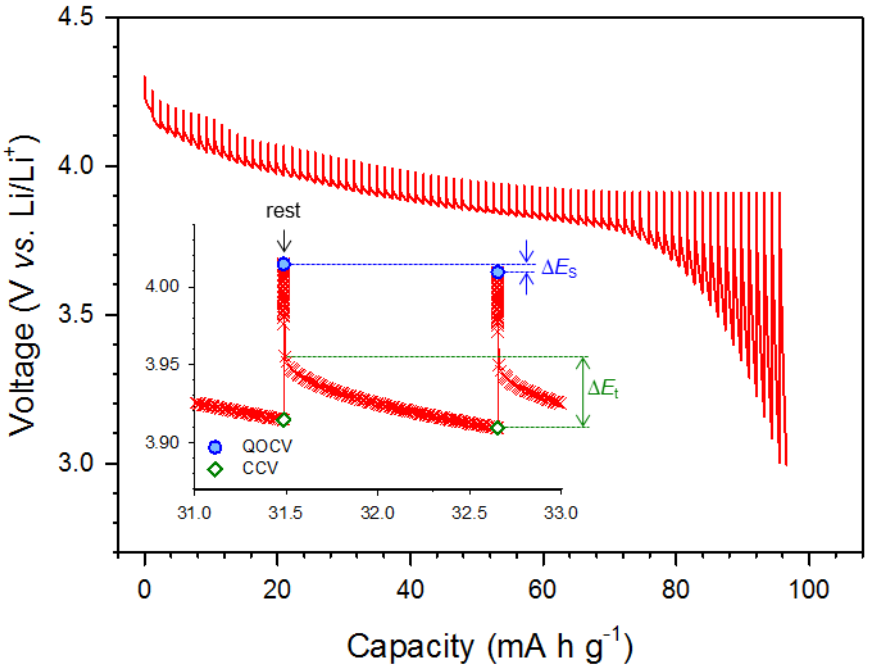

Figure 20. Transient discharge voltage profile obtained from GITT measurements for an LPSCl-infiltrated LCO electrode with a composition of 97:1:2 in an all-solid-state cell at 30 ºC. An enlarged view is shown in the inset, in which the steady-state voltage change (ΔE_S) and the transient voltage change (ΔE_t) values used for obtaining the interfacial contact area are illustrated. Constant current of 0.70 mA cm^{-2} (0.5C) was applied for 60 s, followed by resting for 2 h.

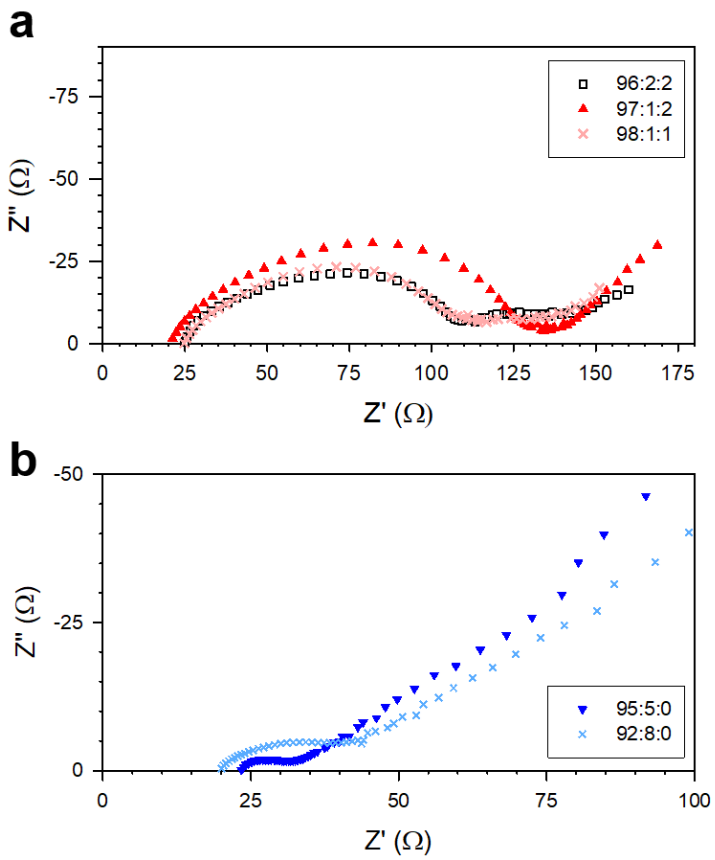

Figure 21. Nyquist plots for a) LCO and b) Gr electrodes in all-solid-state cells.

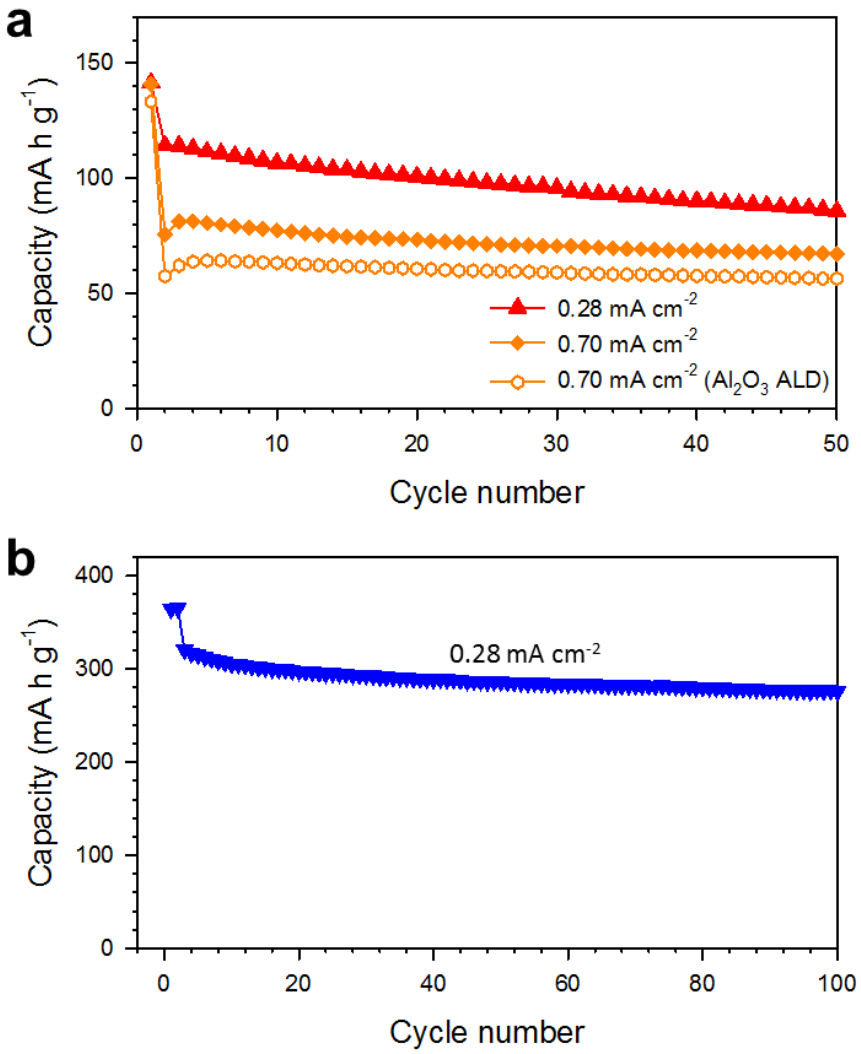

Figure 22. Cycling performances of all-solid-state LCO/Li-In and Gr/Li-In half-cells employing LPSCl-infiltrated a) bare and Al_2O_3 coated LCO and b) Gr electrodes at 30 ºC. The voltage ranges for LCO and Gr electrodes were 3.0–4.3 V and 0.005–2.0 V (vs. Li/Li^+), respectively. The LCO and graphite electrodes were charged/discharged at 0.14 mA cm^{-2} (~0.1C) for the first cycle and the first two cycles, respectively, before cycling at 0.28 mA cm^{-2} or 0.70 mA cm^{-2}. The SE-infiltrated Al_2O_3 coated LCO electrode was prepared by three cycles of ALD prior to the SE-infiltration.

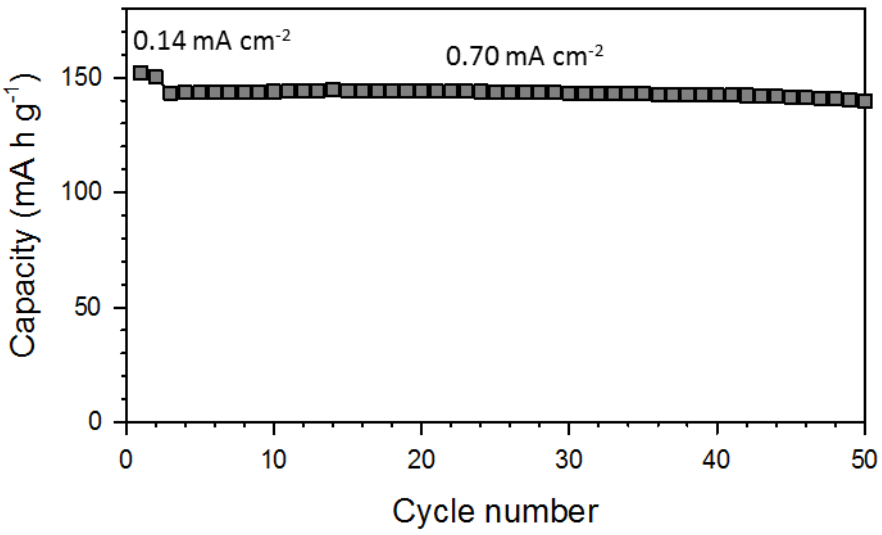

Figure 23. Cycling performance of LCO electrode (without SE-infiltration) in LE cell at 30 ºC.

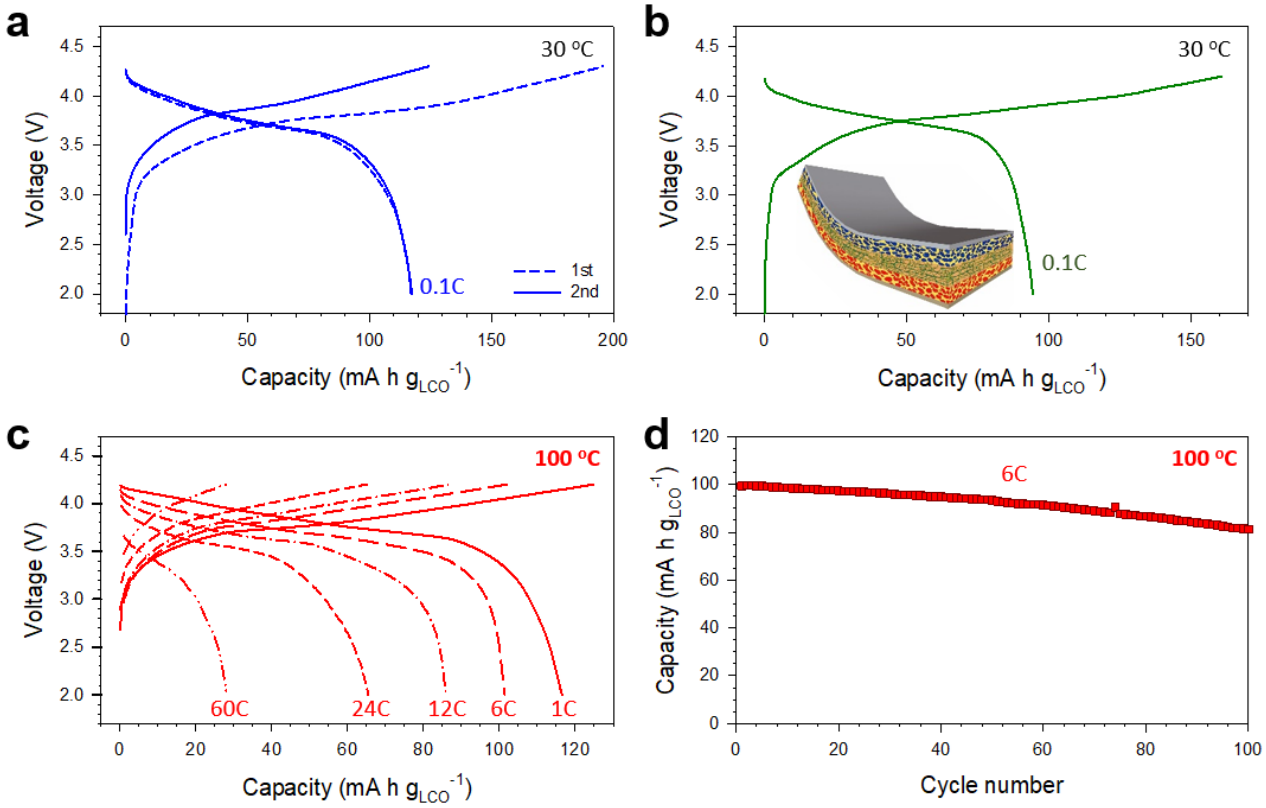

Figure 24. Electrochemical performances of LCO/Gr ASLBs employing LPSCl-infiltrated electrodes at 30 °C and 100 °C. Initial charge-discharge voltage profiles of LCO/Gr ASLB at 0.1C (0.14 mA cm^{-2}) and 30 °C, using a) conventional thick (~600 μm) SE layer (2.0–4.3 V) and b) thin (~70 μm) SE-NW composite film (2.0–4.2 V). c) Charge-discharge voltage profiles at different C-rates and d) cycling performance at 6C for LCO/Gr ASLB at 100 °C (2.0–4.2 V).

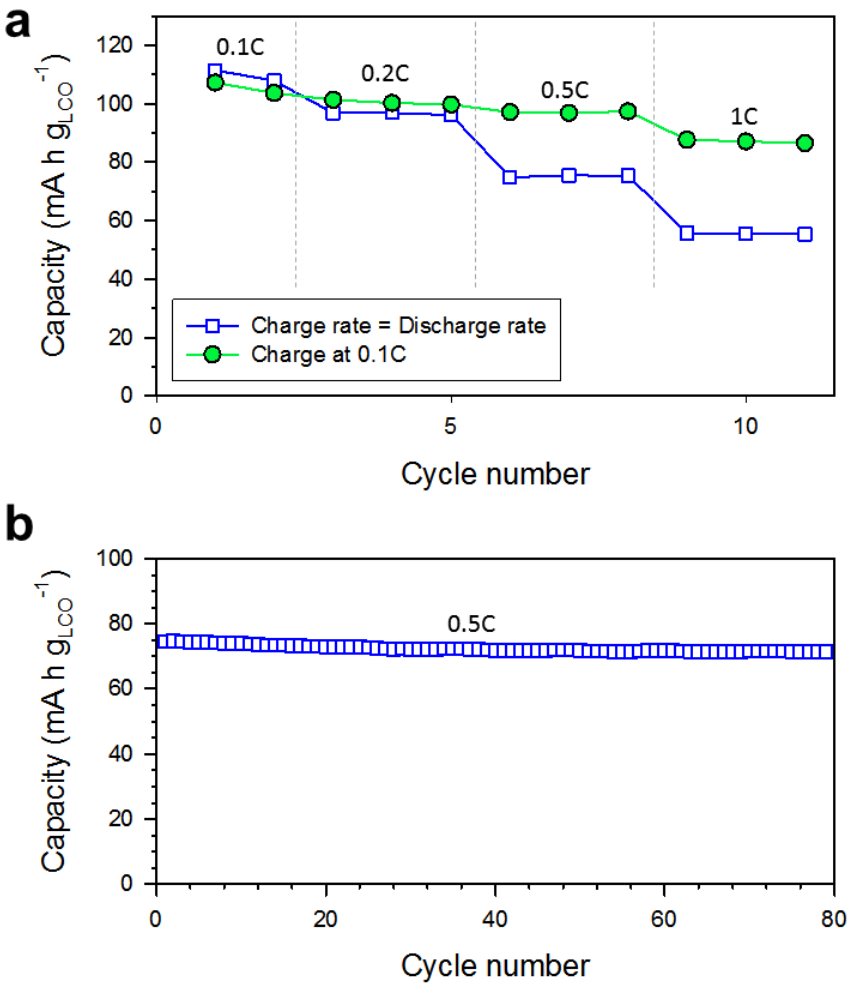

Figure 25. a) Rate and b) cycling performances of LCO/Gr ASLBs employing the LPSCl-infiltrated electrodes at 30 ºC. The discharge C-rates are shown in a. The C-rate for charge and discharge was the same in b. 1C corresponds with 1.4 mA cm^{-2}.

4.2 Sheet-type Li_6PS_5Cl-infiltrated Si anodes for all-solid-state batteries

Si is a promising anode material owing to its highest specific capacity among the alloying materials (4200 mA h g^{-1} for $Li_{4.4}Si$), low operating voltage (~0.3 V vs. Li/Li^+), and its natural abundance. Despite the extremely high specific capacity, practical application of Si in conventional LIBs has been hindered by large volume change (~400%) during lithiation and de-lithiation, which results in pulverization of Si particles and electrical contact loss in the electrodes.[14, 90] Many studies have been devoted to realizing use of Si anodes for LIBs such as reducing the particle size, providing void space for accommodating volume changes, synthesizing nanostructure composite with carbonaceous materials to alleviate volume change.[91] Morover, the advanced polymeric binders such as poly(acrylic acid) (PAA)[92], sodium carboxymethyl cellulose (CMC),[93] and cross-linked PAA/CMC[94], have been employed to maintain electrical contacts during cycling. Compared to electrochemical performance of Si using the conventional PVDF binder, significant improvements in cycling performance of Si electrodes have been observed by using the advanced binders, which is attributed to better adhesion between electrode components.[94]

To date, only a few reports exist on Si anodes for ASLBs and most of the results are based on dry-mixed electrodes using nano-sized Si with extremely low mass loading (0.2–0.3 mg cm^{-2} of Si) at low current density . For high-performance Si ASLBs, an external pressure, which affects the reversible capacity and CE of Si-based ASLBs,[95] should be applied during the operation of ASLBs to maintain ionic/electronic contact in the electrodes. In this regard, the selection of polymeric binders is also expected to have a significant effect on electrochemical performance of Si-based ASLBs.

In this section, SE-infiltrated Si electrodes using solution-processable Li_6PS_5Cl (LPSCl) and investigated the effects of particle size (nano- vs. micro-Si), polymeric binders (PVDF vs. PAA/CMC), and external pressure on the electrochemical performance of the ASLBs. The LPSCl- infiltrated Si electrodes show reversible capacities of over 3000 mA h g^{-1} (0.005–1.5 V *vs.* Li/Li^+) at 30 °C, outperforming dry-mixed electrodes. Finally, all-solid-state LCO/Si full cells using the LPSCl-infiltrated electrodes shows a high energy density of 348 Wh kg_{LCO+Si}^{-1}.

4.2.1 LPSCl-infiltrated Si electrodes

The process of infiltration of conventional composite Si electrodes with solution-processable SEs is illustrated in Figure 26. The Si composite electrodes were prepared by casting slurries, which were a mixture of active materials (m-Si or n-Si), polymeric binder (PVDF or PAA/CMC), and carbon additives. The SE-infiltrated Si electrodes were prepared by infiltration of the LPSCl solution using the dip-coating method, followed by solvent removal and additional heat-treatment at 180 °C under vacuum. The surface of Si wetted by the SE solution was well covered with an LPSCl layer during evaporation heat-treatment process. The weight fraction of LPSCl was ~50 wt% in electrodes after infiltration. Finally, highly dense LPSCl-infiltrated Si electrodes were fabricated by cold-pressing under 770 MPa.

Raman and XRD analyses were performed for the m-Si electrodes before and after infiltration to examine the compatibility of m-Si and LPSCl solution (Figure 27 and 28). The LPSCl infiltrated Si electrode show strong peaks at 520 cm^{-1} (labelled as "#"), which is the characteristic peak of crystalline Si (T_{2g}). The LPSCl peak, centered at 423 cm^{-1} and corresponding to PS_4^{3-}, is also observed in LPSCl-infiltrated electrode (Figure 27).[42] The XRD patterns of LPSCl-infiltrated electrode reveal no change in the Si peak positions (labelled as "#") and contain signature peaks of LPSCl (Figure 28 and 29). The impurities for Sol-LPSCl are not clearly observed in the composite electrodes due to limited mass loading of LPSCl in the composite electrodes. Both Raman and XRD results indicate that Si is compatible with LPSCl solution and confirm that formation of LPSCl is not affected by electrode components even after at high-temperature heat treatment at 180 °C. Figure 30 presents the cross-sectional FESEM images of the cold-pressed LPSCl-infiltrated m-Si electrode and the its EDXS elemental maps of silicon and sulfur. The pores of the m-Si electrode are filled well with LPSCl, which is attributed to the excellent wettability of the LPSCl solution on the electrode and the high deformability of the sulfide SEs. Moreover, negligible porosity is observed after cold-pressing, which confirms the intimate ionic contact between m-Si and LPSCl. The cross-sectional FESEM image and corresponding EDXS elemental maps of the LPSCl infiltrated n-Si electrode show even distribution of LPSCl in the electrode, confirming the excellent penetration of LPSCl solution into electrodes using the nanoparticles (Figure 31) .

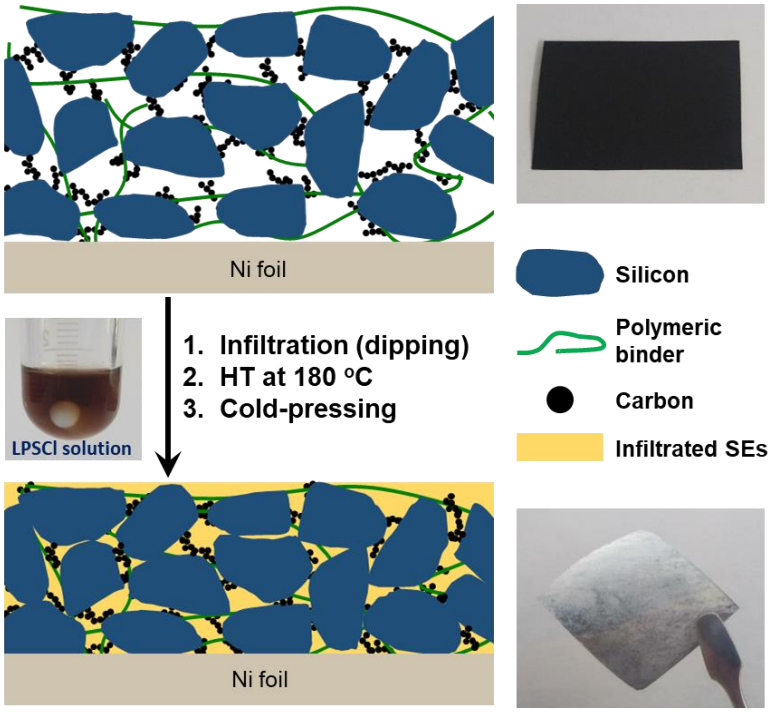

Figure 26. Schematic diagram illustrating the process for infiltration of conventional Si composite electrodes with solution-processable SEs. The photographs show the m-Si electrodes before and after the infiltration of Li_6PS_5Cl (LPSCl). A photograph of LPSCl-dissolved ethanol solution is also shown.

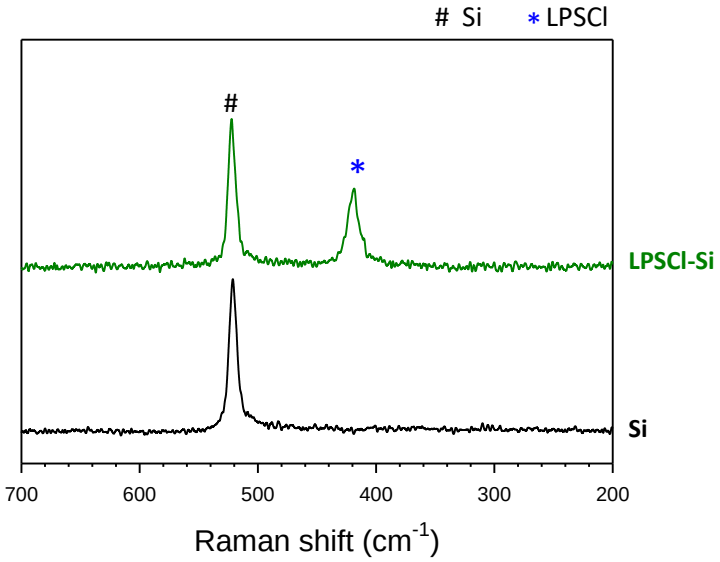

Figure 27. Raman spectra of m-Si electrodes before and after the infiltration of solution-processed LPSCl.

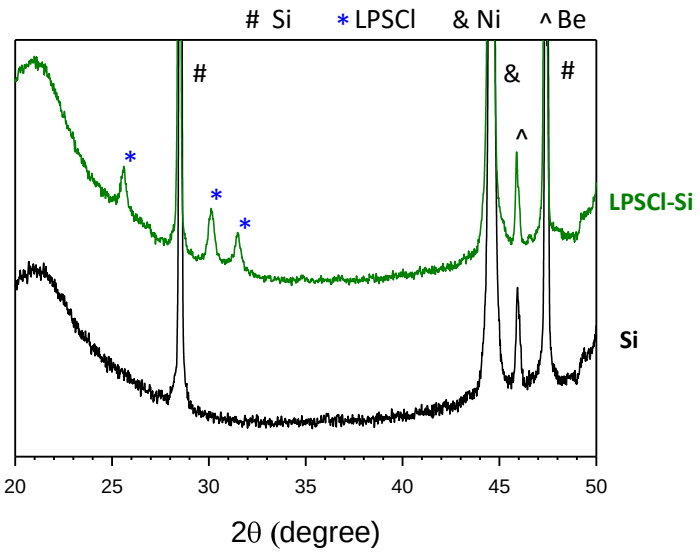

Figure 28. XRD patterns of m-Si electrodes before and after the infiltration of solution-processed LPSCl.

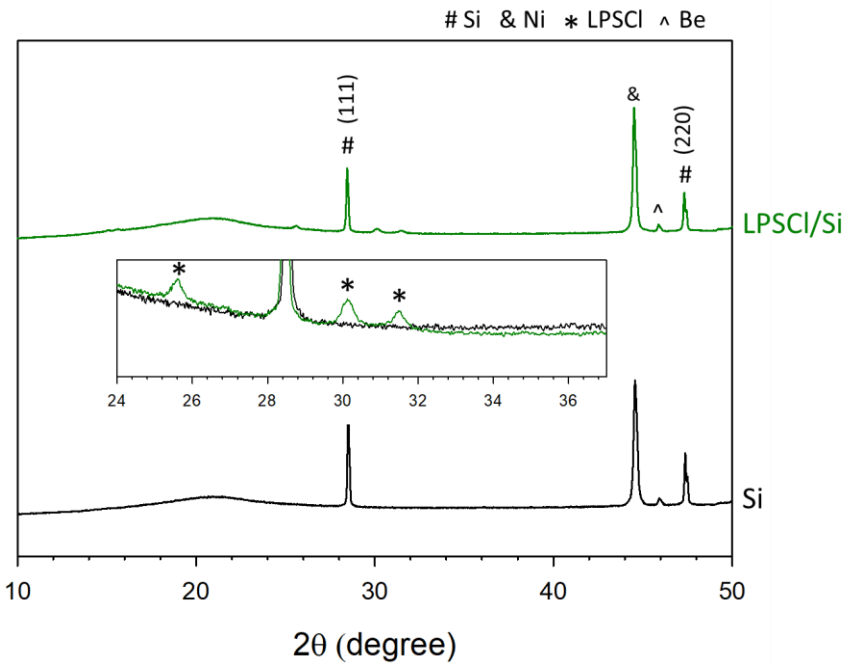

Figure 29. XRD patterns of the m-Si electrodes before and after infiltration of the LPSCl. Enlarged views to reveal the peaks of Li_6PS_5Cl are shown in the inset.

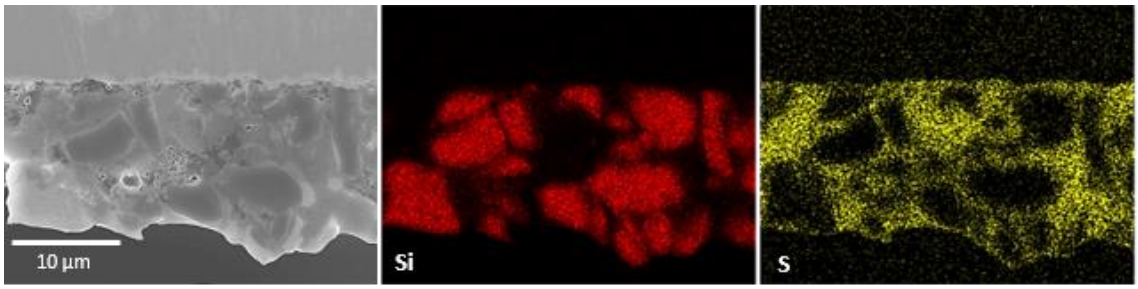

Figure 30. cross-sectional FESEM image of the LPSCl-infiltrated m-Si electrode and its corresponding EDXS elemental maps.

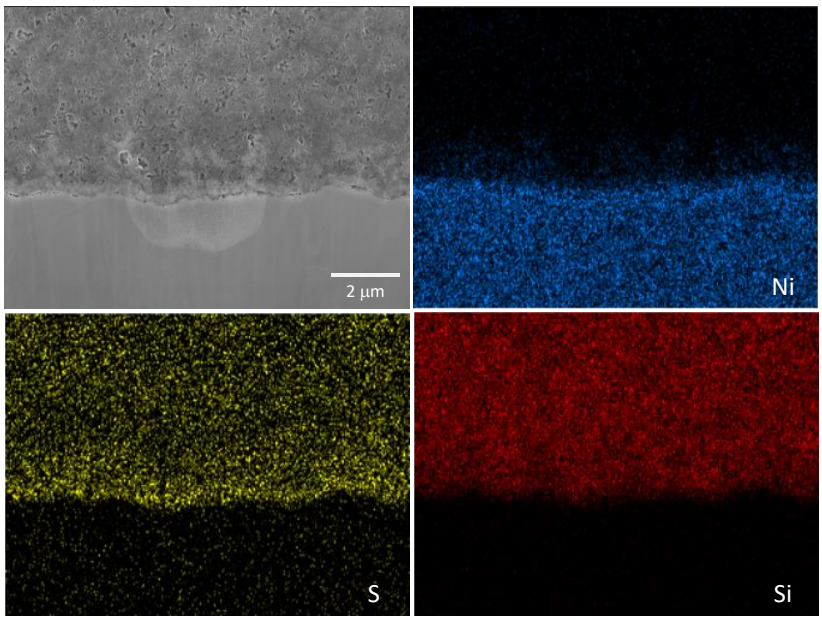

Figure 31. Cross-sectional FESEM image of the LPSCl-infiltrated n-Si electrode after cold pressing and the corresponding EDXS elemental maps of Ni, S, and Si.

4.2.2 Electrochemical characterization

The electrochemical characterization of all-solid-state Si/Li-In half cells using the LPSCl-infiltrated Si (m-Si or n-Si) electrodes with two different kinds of binders (PVDF or PAA/CMC) was performed at 30 °C under external pressure. The first- and second- cycle voltage profiles of the LPSCl-infiltrated Si electrodes are shown in Figure 32a (m-Si) and Figure 32b (n-Si). Surprisingly, all the electrodes show high first-cycle capacities of over 3000 mA h g^{-1} and initial CEs of over 80% for both m-Si and n-Si at 0.05C (0.20–0.25 mA cm^{-2}). In conventional LIBs, it is generally known that m-Si shows lower capacities and initial CEs than n-Si because of the loss of electrical contacts and pulverization of Si particle due to the larger volume change of m-Si than that of n-Si.[91] However, in this work, m-Si electrode shows higher initial CE of 88.7% as compared with that of n-Si (80.4%). It should be noted that this value is greater than m-Si with PAA/CMC electrode using FEC-added liquid electrolyte (84.4 %, Figure 33). The large surface area of n-Si caused more severe irreversible consumption of at electrode-electrolyte interface compared to that of m-Si, resulting in low CE for n-Si. However, after 10th cycle, the CEs were stabilized to nearly 99.5% for both Si electrodes, which means formation of favorable passivation layers at initial cycles (Figure 34). In contrast to Si electrode in conventional LIBs, the effect of polymeric binders (PVDF vs. PAA/CMC) on electrochemical performance is negligible, which is attributed to large external pressure of 140 MPa.

The comparison of polymeric binders for LE-based cells is shown in Figure 33. Before assembling the cells, all the electrodes were heat-treated at 180 °C under vacuum for cross-linking of PAA and CMC. While both electrodes exhibited similar discharge (lithiation) capacities, the charge (de-lithiation) capacity for the electrode using PAA/CMC is much higher (~2250 mA h g^{-1}) than that using PVDF (~890 mA h g^{-1}). It is known that a three-dimensionally cross-linked PAA/CMC is formed during heat-treatment, thereby contributing to maintain the electrical contacts between electrode components upon large volume changes.[94] In this regard, the negligible effect of polymeric binders on the electrochemical performance of all-solid-state cells could be surprising. During operation of all-solid-state Si/Li-In half cells, it should be noted that the external pressure of 140 MPa is applied to maintain ionic and electronic contact upon cycling. The high reversible capacities and initial CEs regardless of polymeric binders and particle size of Si could be explained by existence of the high external pressure. In short, high external pressure during operation could be critical for maintaining electrical contacts upon cycling and is enough to nullify the effect of particle size of Si and polymeric binders. The first- and second-differential discharge-charge voltage profiles for the LPSCl-infiltrated m-Si and n-Si electrodes are shown in Figure 35a and 35b. The crystalline Si undergoes transformation into amorphous phase (a-Li_xSi) during lithiation and then rapidly crystallize into c-$Li_{15}Si_4$ during precedent lithiation below 50 mV and the sharp peaks at ~0.45 V is indicative of the de-lithiation of c-$Li_{15}Si_4$. The rate performances of the LPSCl-infiltrated m-Si and n-Si electrodes are shown in Figure 32c and 33d. The rate capabilities of Si electrodes do not show significant variations by the particle size of Si (m-Si vs. n-Si) or the

polymeric binders (PVDF vs. PAA/CMC). The n-Si electrodes showed slightly better cycling performance compared to m-Si electrodes. The capacity retention of n-Si as compared with the capacity at the 9th cycle after 30 cycles is higher (91.1% and 78.2% for using PVDF and PAA/CMC, respectively) than that of m-Si (73.9% and 69.3% for using PVDF and PAA/CMC, respectively).

The results for the LPSCl-infiltrated m-Si electrode is compared to those of dry-mixed electrodes without binder (referred to as "Mixture1") and an electrode with PVDF binder (referred to as "Mixture2") (Figure 36). The LPSCl-infiltrated electrode shows much higher capacity (3246 mA h g^{-1}) than that of Mixture1 (1437 mA h g^{-1}) and Mixture2 (1243 mA h g^{-1}) electrodes, which could be explained by the intimate ionic contacts of Si with LPSCl enabled by using liquefied SEs. In conventional dry-mixing process, the particle size of Si and SEs, which is not carefully considered for Mixture1 and Mixture2 electrodes, could have significant effect on electrochemical performance. The distribution of electrode components might be less uniform than that in the LPSCl-infiltrated electrodes, which result in poor electrochemical performance. These results highlight that the infiltration process using solution-processable SEs is advantageous for the fabrication of composite electrodes for ASLBs in terms of ionic and electronic percolation.

Despite the high initial capacities of over 3000 mA h g^{-1}, the LPSCl-infiltrated Si electrodes show gradual capacity fading during cycling (Figure 32), which might be caused by side reaction between Si and LPSCl at a low voltage or contact loss during lithiation and de-lithiation. Figure 37a compares the self-discharge behavior of LPSCl-infiltrated n-Si electrodes with varying storage times after lithiation at 30 °C. The n-Si was used due to its higher surface area than that of m-Si. While a marginal decrease in capacity is observed, CEs is almost the same after 7 days (97.4% vs. 97.0% without storage). It is therefore confirmed that effect of side reaction between Si and LPSCl on electrochemical performance could be marginal. The cross-sectional FESEM image of m-Si electrodes after 40 cycles is shown in Figure 37b. Compared with the pristine densified electrode (Figure 30), cracks are observed in the cycled electrodes, which is caused by severe volume change in Si during lithiation and de-lithiation. The ionic and electronic contact loss in the electrodes gradually decreased the capacities of the LPSCl-infiltrated Si electrodes. While the external pressure of 140 MPa is high enough to nullify the effect of the particle size of Si and the polymeric binders, but it could not completely prevent the electrical contact loss in electrodes during cycling. However, in perspective of practical applications, an external pressure of 140 MPa is not realistic and should be required to be minimized while retaining the performance. The discharge-charge voltage profiles of the LPSCl-infiltrated Si electrodes with variation of the external pressure is shown in Figure 38. Notably, the LPSCl-infiltrated Si electrodes exhibit similar capacities at both high (140 MPa) and low (20 MPa) external pressures. However, further lowering of the external pressure to 5 MPa for n-Si electrode results in the significantly lowered CEs (80.4% and 82.2% under 140 and 20 MPa, respectively vs. 64.0% under 5 MPa, Figure S9), indicating that the low external pressure of 5 MPa would be not enough to nullify the effects of large volume

changes of Si during lithiation and de-lithiation. This result emphasizes the importance of engineering of external pressure for high-capacity electrode materials having large volume changes.

Finally, an all-solid-state full cells using the LPSCl-infiltrated LCO and m-Si (with PVDF) electrodes were evaluated at 30 °C (Figure 39). The m-Si was selected for full cells because of its high initial CE and tap density compared with n-Si electrode. The LPSCl-infiltrated LCO electrode was prepared by the same procedure as in previous work.[96] The full cell configuration is shown in the inset in Figure 39a. The LCO/m-Si full cell shows a reversible capacity of 104 mA h g_{LCO}^{-1} at 0.14 mA cm^{-2} in the voltage range of 2.8–4.2 V, which translates to an energy density of 348 W h kg_{LCO+Si}^{-1}. The application of high-capacity Si anode improves the energy density by 21% compared with the LCO/Gr full cell (279 Wh kg_{LCO+Gr}^{-1}) in previous paper.[96] Moreover, stable cycling performance was observed at 0.2C (0.28 mA cm^{-2}). Although the electrochemical performance is not satisfactory, it should be considered that pure m-Si powders were used in this work and further elaboration such as a Si-carbon composite, and functional binders with Li^+ conductivity and/or self-healing ability, combined with engineering of external pressure would lead to the improvements.[97-98]

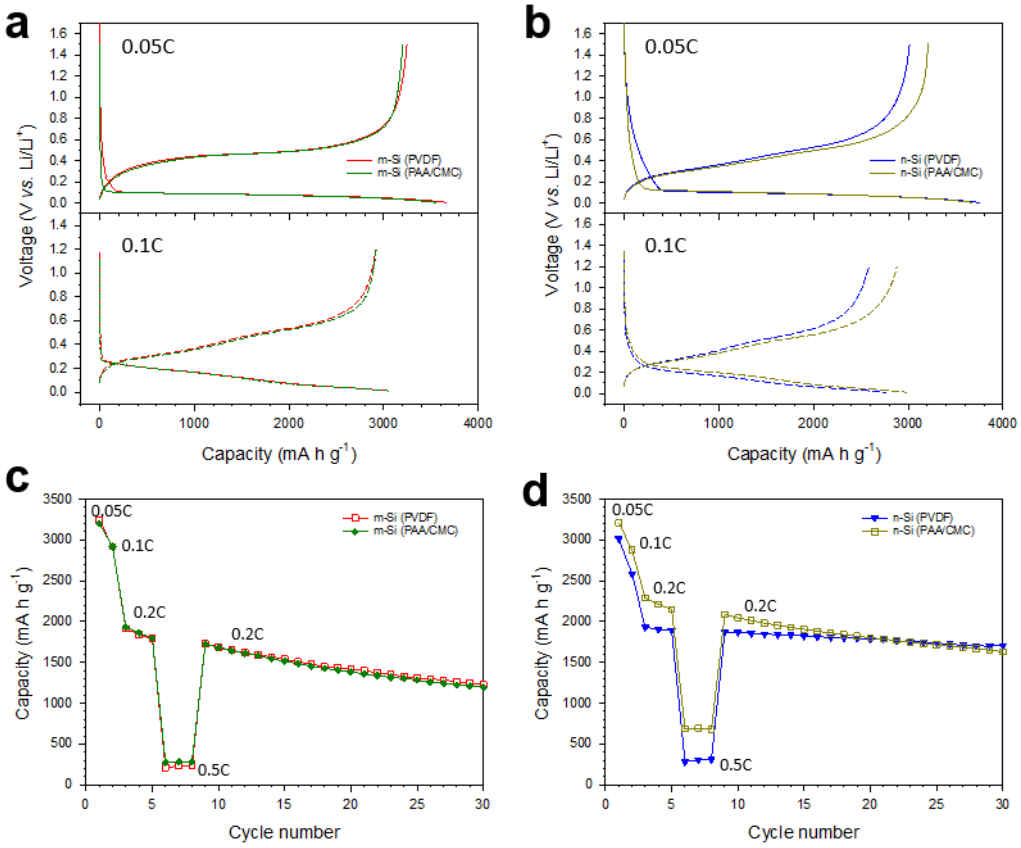

Figure 32. Electrochemical characterization of all-solid-state Si/Li-In half cells employing LPSCl-infiltrated electrodes at 30 °C. First- and second-cycle discharge-charge voltage profiles of (a) m-Si and (b) n-Si electrodes (0.005–1.5 V for the first cycle and 0.01–1.2 V for the second cycle). Charge capacity varied by C-rate as a function of cycle number for (c) m-Si and (d) n-Si electrodes in all-solid-state cells. The C-rates for charge and discharge were the same (1C = 4.0–5.0 mA cm^{-2}).

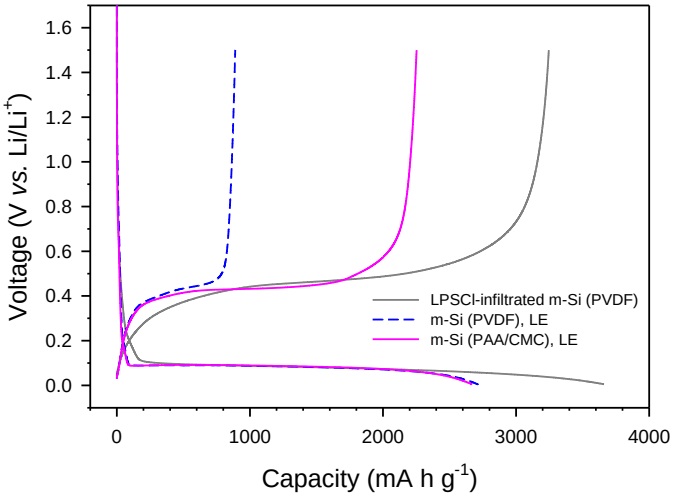

Figure 33. First-cycle discharge-charge voltage profiles of all-solid-state cell using LPSCl-infiltrated m-Si and liquid-electrolyte cells employing m-Si using PVDF or PAA/CMC at 0.05C (0.20–0.25 mA cm^{-2}) and 30 °C. Heat treatment was carried out for all electrodes at 180 °C under vacuum prior to the electrochemical test.

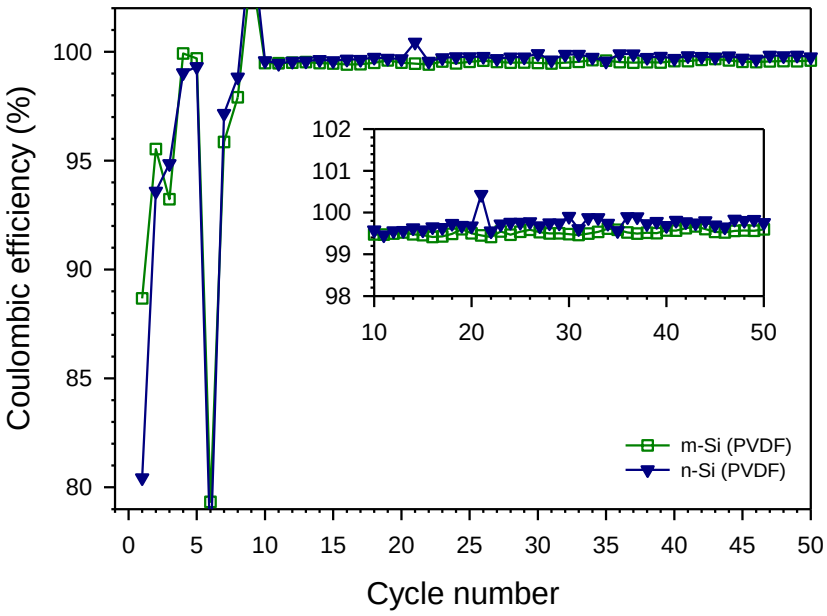

Figure 34. Coulombic efficiencies (CEs) of m-Si and n-Si electrodes with PVDF in all-solid-state Si/Li-In half cells.

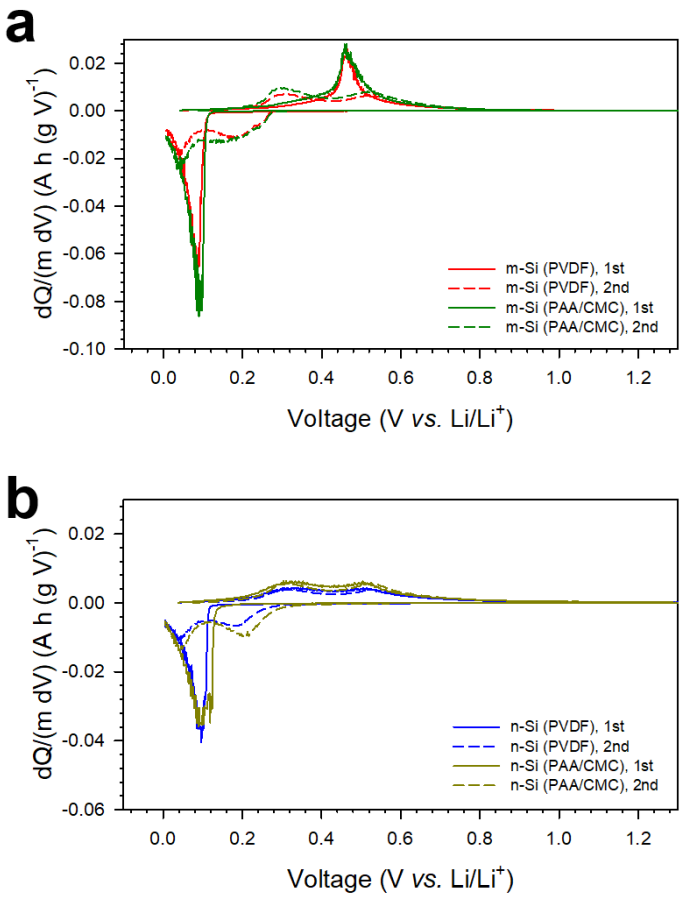

Figure 35. The differential discharge-charge capacity profiles during the first two cycles for (e) m-Si and (f) n-Si electrodes.

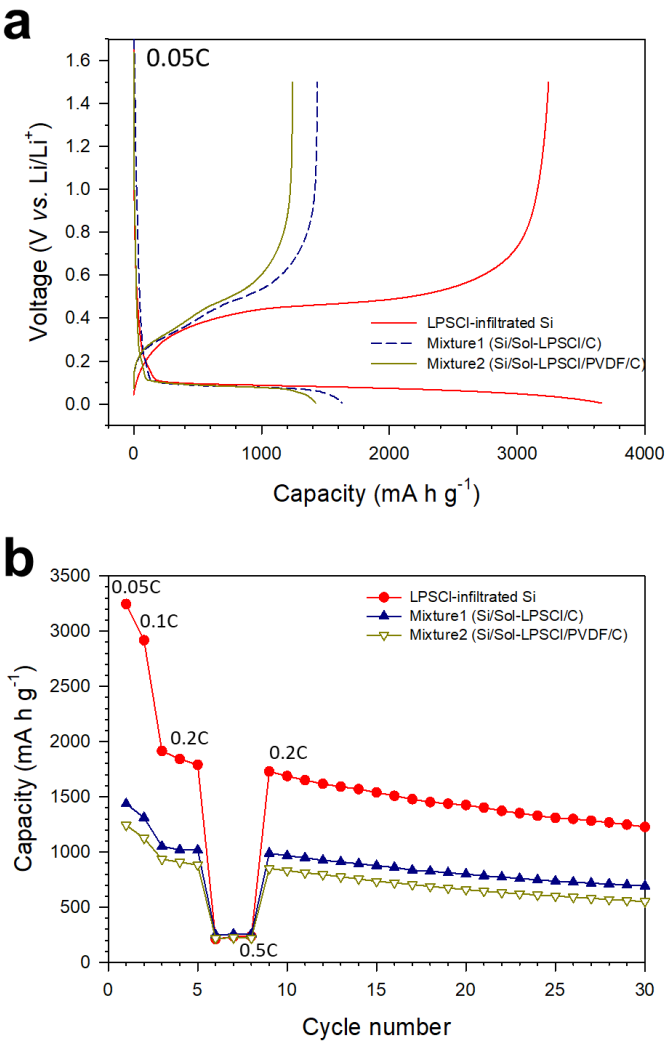

Figure 36. Electrochemical performances of all-solid-state Si/Li-In half cells employing the LPSCl-infiltrated electrode and the conventional mixture electrodes, which were prepared by manual mixing in dry conditions (Mixture1 and Mixture2). (a) First-cycle discharge-charge voltage profiles of Si/Li-In all-solid-state cells at 0.05C (0.20–0.25 mA cm^{-2}) and 30 °C. (b) Rate performance of all-solid-state Si/Li-In cells.

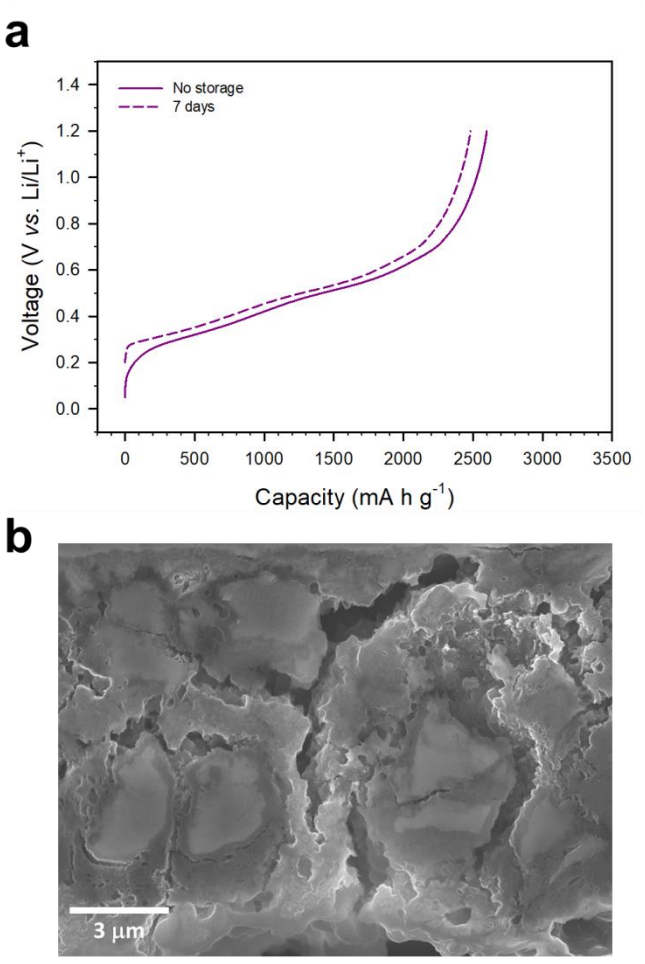

Figure 37. (a) Charge (de-lithiation) voltage profiles of LPSCl-infiltrated n-Si electrode with variation of storage after discharge (lithiation) at 30 °C. (b) The cross-sectional FESEM image of the LPSCl-infiltrated m-Si electrode after 40 cycles.

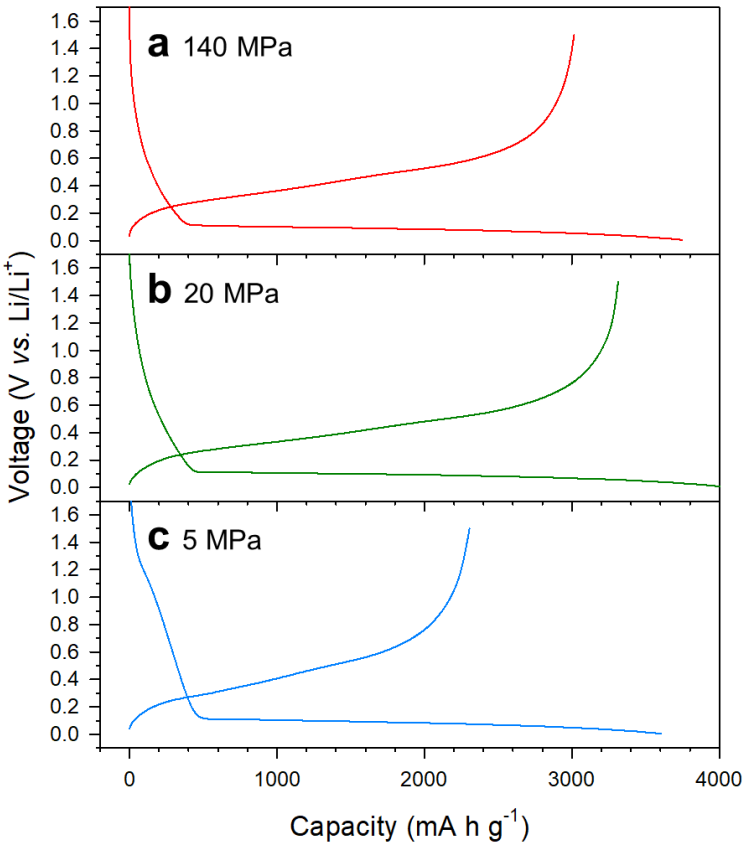

Figure 38. First-cycle discharge-charge voltage profiles of all-solid-state Si/Li-In half cells employing LPSCl-infiltrated n-Si electrodes with PVDF binder at 0.05C (0.20–0.25 mA cm^{-2}) and 30 °C under the external pressure of a) 140, b) 20, and c) 5 MPa.

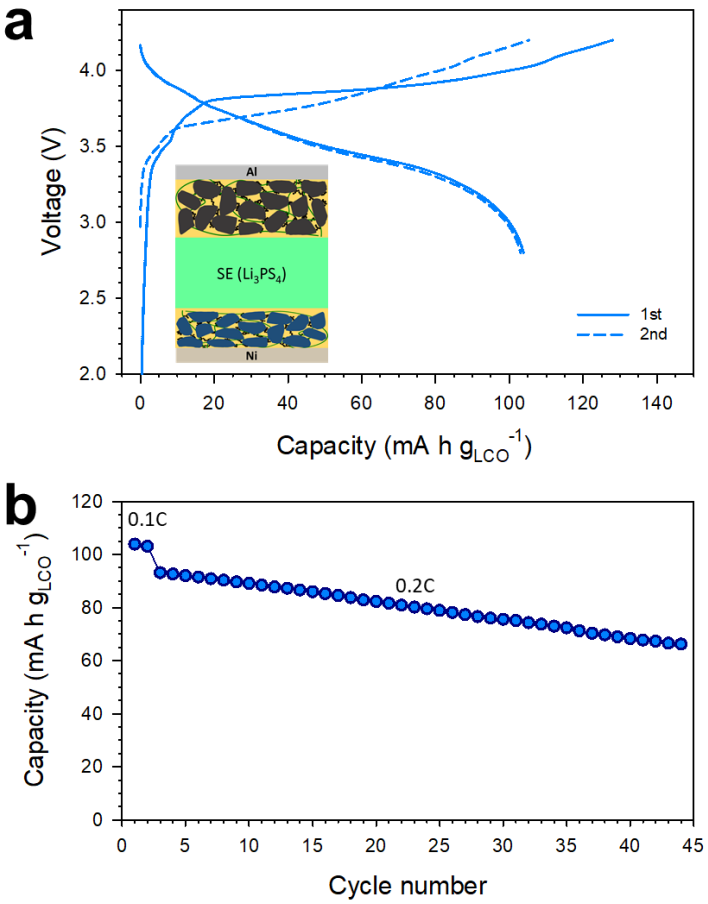

Figure 39. Electrochemical performance of LCO/m-Si all-solid-state full-cells employing LPSCl-infiltrated LCO and m-Si electrodes at 30 °C: (a) Initial charge-discharge voltage profiles at 0.1C (0.14 mA cm^{-2}) and (b) cycling performance. The cell configuration of LCO/m-Si ASLBs is illustrated in the inset in (a).

4.3 Thin and flexible solid electrolyte membranes with ultrahigh thermal stability for all-solid-state lithium-ion batteries

Despite the favorable properties of sulfide SEs, there are only few reports for sulfide SE-based membranes due to the chemical instability which hinders the application of solution-based process. In this section, facile and scalable fabrication of thin (40−70 μm) sulfide SE membrane by infiltration of solution-processable SEs into highly porous electrospun polymer membranes is demonstrated. The excellent thermal stability of polyimide (PI) allows the heat-treatment at high temperature (400 °C), which is necessary to improve the Li^+ conductivity of SE membrane. The $LiNi_{0.6}Co_{0.2}Mn_{0.2}O_2$ (NCM622)/graphite full cells using SE-infiltrated PI (40 μm) show a high reversible capacity of 146 mA h g_{NCM622}^{-1}, and energy density of 110 W h kg_{cell}^{-1} (including current collector) at 30 °C. The negligible capacity fading after exposure to high temperature (180 °C) demonstrates the excellent thermal stability of SE-infiltrated PI membranes. Furthermore, new fabrication protocol for ASLBs is demonstrated by injecting SE solution into pre-assembled $LiCoO_2$/PI/$Li_4Ti_5O_{12}$ assembly.

4.3.1 Characterization of SE membranes

The fabrication process of SE membranes by infiltration of solution-processable SEs into porous polymer matrix is illustrated in Figure 40. Electrospun porous polymer membranes (polyimide (PI) or polyetherimide (PEI)) having interconnected fibrous structures and high porosity of 80−90% were used as scaffold for SE infiltration. The thin SE membranes were fabricated by dropping the SE solution onto the polymer matrixes. Both PI and PEI matrixes showed excellent wettability with SE solution, enabling excellent penetration of SE into interconnected fibrous structures. Moreover, the thickness of resulting SE membranes was easily controlled by varying the thickness of polymer matrixes and the amount of SE solution. After drying the solvent, further heat-treatment was carried out at 400 °C for PI and 180 °C for PEI for removing organic impurities and improving crystallinity. Finally, SE-infiltrated polymer membranes were pressed under 550 MPa for achieving densified thin SE membranes.

The PI membranes were prepared by electrospinning of polyamic acid (PAA) precursor solutions, followed by imidization. The absorption peaks of imide group were identified by Fourier transform infrared spectroscopy (FTIR), indicating asymmetric C=O stretching at 1775 cm^{-1}, symmetric C=O stretching at 1720 cm^{-1}, and C-N stretching at 1375m^{-1} (Figure 41).[99] Moreover, the absorption peak related with N-H stretching at 3300–3500 cm^{-1} did not observed, which confirms the complete conversion of PAA into PI by thermal imidization process. The photograph of electrospun PI membrane and its microstructure morphology are shown in Figure 42. The FESEM image reveals that the PI membrane consists of randomly arranged nanofibers with diameters of around 500 nm and includes

many pores between fibers. The porosity value of the is about 80−90%, which is enough to infiltrate the large amounts of SEs. In addition, TGA result for PI membrane indicates that the onset temperature for thermal decomposition is about ~500 °C and weight loss is less than 2% up to 400 °C in N_2 atmosphere (Figure 43). This feature allows heat-treatment at high temperature after infiltration, which contributes to increasing the Li^+ conductivity of SE membranes. Moreover, unlike polymer electrolytes such as PEOs having poor thermal stability, the combination of SEs with the PI membrane does not significantly deteriorate the safety of ASLBs. In these regards, the PI membrane was chosen for infiltration of solution-processable SEs.

The Li^+ conductivities of solution-processed $Li_6PS_5Cl_{1-x}Br_x$ ($0 \le x \le 1$) with variation of heat-treatment temperature and halogen composition are shown in Figure 44. The solution-processed single halogen Li_6PS_5X (X = Cl, Br) exhibited the Li^+ conductivity of 0.1−0.2 mS cm^{-1} after heat-treatment at 180 °C. These values are too low for application to SE membranes because combination of SEs with polymers causes the decrease of Li^+ conductivity owing to ionically insulating polymer.[52] Previous reports demonstrated that the optimization of lattice polarizability and site disorder of X^-/S^{2-} leads to improvement in the Li^+ conductivities.[82, 100] The solution-processed multi-halogen $Li_6PS_5Cl_{0.5}Br_{0.5}$ exhibited higher Li^+ conductivity of 0.4 mS cm^{-1} under heat-treatment at 180 °C, compared those of the single-halogen Li_6PS_5Cl and Li_6PS_5Br. Further heat-treatment of solution-processed SEs at 400 °C increased the Li^+ conductivities to ~1.0 mS cm^{-1}, which is attributed to the removal of organic impurities and improved crystallinity. The $Li_6PS_5Cl_{0.5}Br_{0.5}$ shows the highest Li^+ conductivity of 2.0 mS cm^{-1}, which is enough to be used for SE membranes and this trend is in good agreement with previous results for $Li_6PS_5Cl_{1-x}Br_x$ ($0 \le x \le 1$) prepared by solid-state or liquid-phase syntheses.[82, 100-101] Figure 45 shows the powder X-ray diffraction (XRD) patterns of solution-processed $Li_6PS_5Cl_{1-x}Br_x$ ($0 \le x \le 1$) heat-treated at 400 °C. All samples had cubic argyrodite phase (CIF no. 418490 for Li_6PS_5Cl) as major crystalline phase and shift in main peaks was observed owing to the larger ionic size of Br- (1.82 Å for coordination number (CN) = 6) than that of Cl- (1.67 Å for CN = 6). The minor impurities such as Li_2S, LiX were also observed for all samples, which is possibly generated due to reactivity of PS_4^{3-} unit with ethanol.[85, 102]

Based on the Li^+ conductivities of solution-processed SEs and thermal stability of PI membranes, the heat-treatment of $Li_6PS_5Cl_{0.5}Br_{0.5}$-infiltrated PI membrane was performed at 400 °C and this SE membrane is referred to as “PI-LPSClBr”. The photograph of PI-LPSClBr and its corresponding FESEM image are shown in Figure 46. The PI-LPSClBr is flexible and compact without any noticeable cracks on the surface, which is attributed to excellent mechanical properties of the PI membrane and deformability of sulfide SEs. It should be emphasized that these features could provide the applicability of large-scale fabrication process such as roll-to-roll processes for ASLBs. The variations of the Li^+ conductivities and conductance of SE membranes as function of thickness is shown in Figure 47 and

Table 3. In order to compare the effect of heat-treatment temperature, the electrospun PEI having poor thermal stability than PI was also used. The $Li_6PS_5Cl_{0.5}Br_{0.5}$-infiltrated PEI membrane was heat-treated at 180 °C and referred to as "PEI-LPSClBr" (Figure 48). The PI-LPSClBr shows the Li^+ conductivities ranging of 0.058–0.2 mS cm^{-1} at 30 °C depending on the thickness, which is much higher than that of PEI-LPSClBr (0.0013 mS cm^{-1}). Due to the ionically insulating PI and PEI, it is not surprising that the Li^+ conductivities of LPSClBr-infiltrated membranes are lower than that of solution-processed LPSClBr (2.0 mS cm^{-1}). However, it is worth to be noted that consideration of conductance rather than conductivity is critical for electrochemical performance of all-solid-state cells. In previous work, the electrochemical performance of $LiTiS_2/Li_4Ti_5O_{12}$ all-solid-state full cell using thin NW-Li_3PS_4 membranes (0.2 mS cm^{-1}, 70 μm) outperformed the that of ASLB using thick Li_3PS_4 pellet (0.73 mS cm^{-1}, 700 μm), demonstrating the importance of the ionic conductance.[52] The PI-LPSClBr shows the similar ionic conductance to the solution-processed LPSClBr, implying the use of PI-LPSClBr does not significantly degrade the electrochemical performance of ASLBs. Moreover, the use of thin SE membranes has potential to realize high-energy density of ASLBs by significantly reducing the thickness and the mass loading of SE layers (5.0–9.5 mg cm^{-2} for PI-LPSClBr and 113 mg cm^{-2} for SE pellet). The electronic conductivity of the PI-LPSClBr also measured by the DC polarization method using Ti/SE membrane/Ti cell. It should be noted that the high electronic conductivity of SE could be responsible for gradual capacity loss by self-discharge. The PI-LPSClBr exhibited the electronic conductivity of ~10^{-9} S cm^{-1} based on the linear fitting of applied voltage and stabilized current (Figure 49), which is 5 orders lower than the ionic conductivity. This result indicates that the PI-LPSClBr is almost a pure Li^+ conductor. Figure 50 shows the cross-sectional FESEM image of cold-pressed PI-LPSClBr and its corresponding EDXS elemental maps for S and Cl. The liquified SEs were penetrated well into the pores between PI nanofibers, which is attributed to the excellent wettability of SE solution on PI membranes.

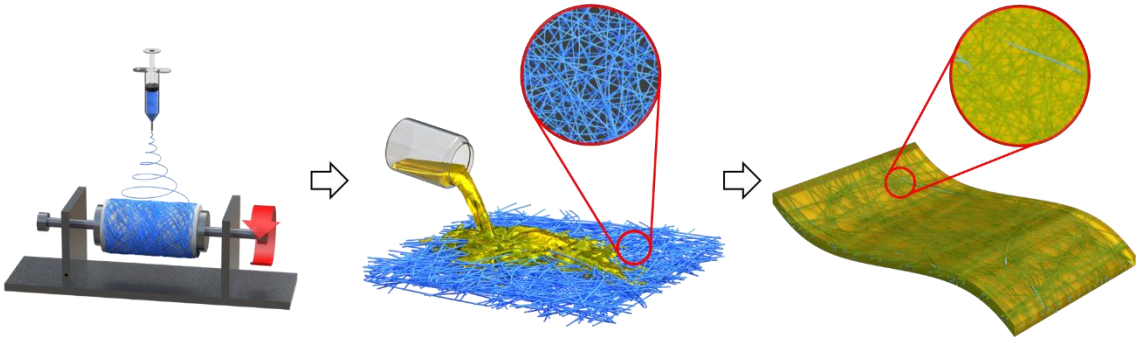

Figure 40. Schematic illustrating the fabrication of sulfide SE membranes for ASLBs by infiltration of electrospun porous polyimide (PI) nonwovens (NWs) with solution-processable $Li_6PS_5[Cl,Br]$.

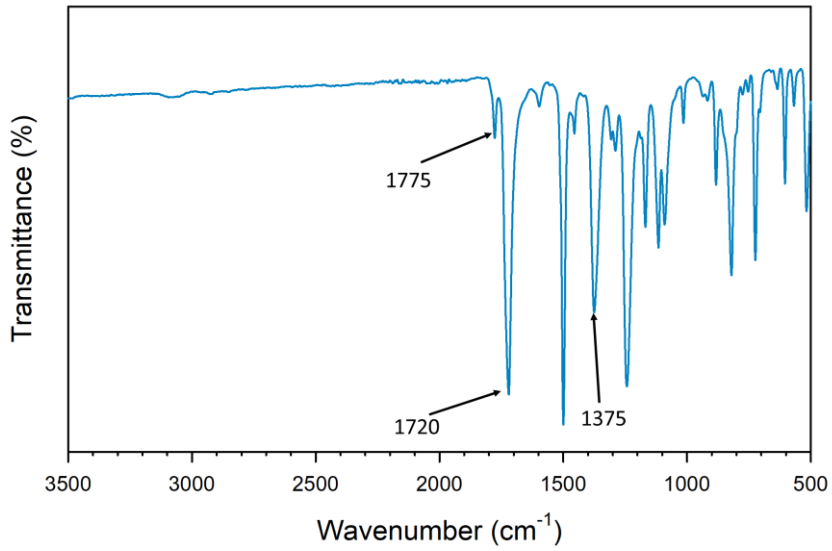

Figure 41. FTIR spectrum of the electrospun PI membranes.

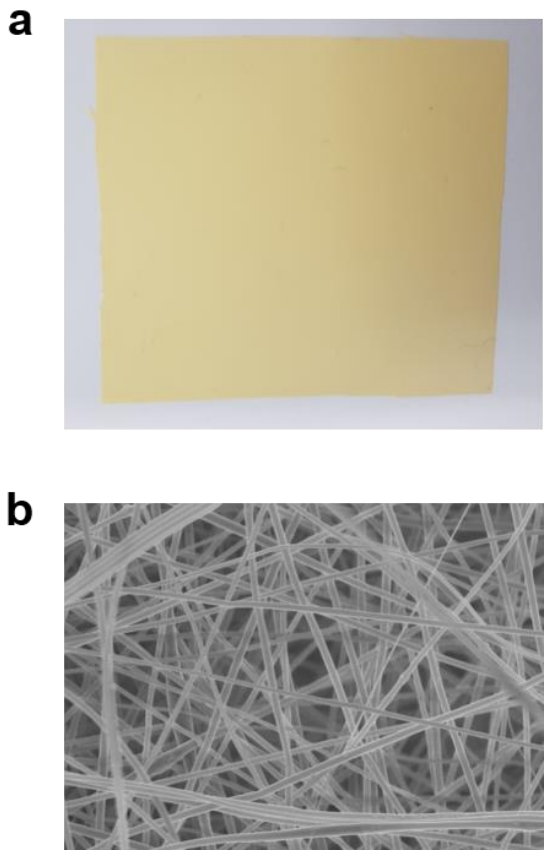

Figure 42. a) photograph and b) FESEM image of the electrospun PI membranes.

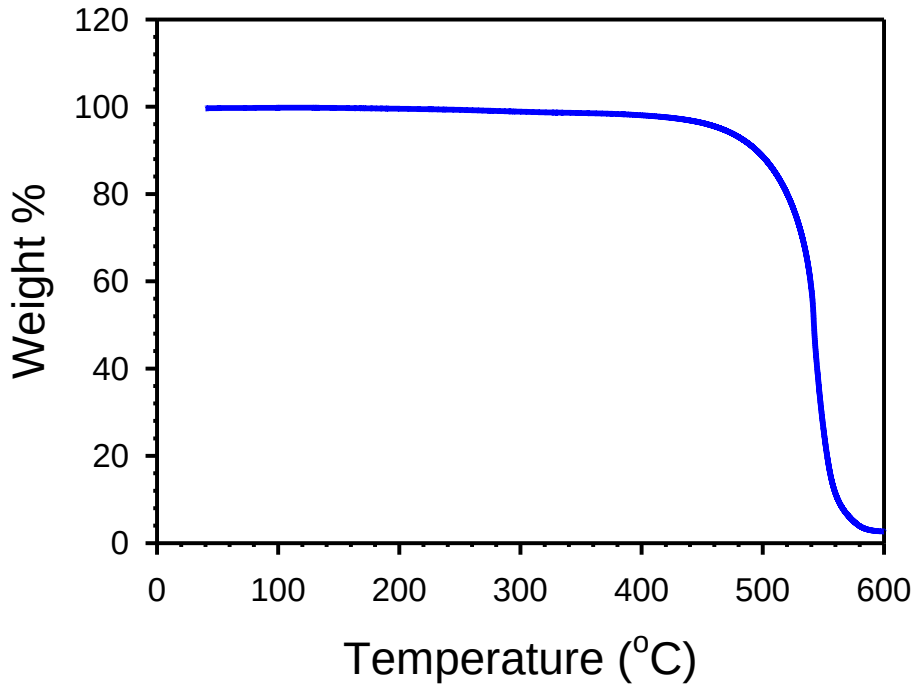

Figure 43. TGA result of the electrospun PI membranes.

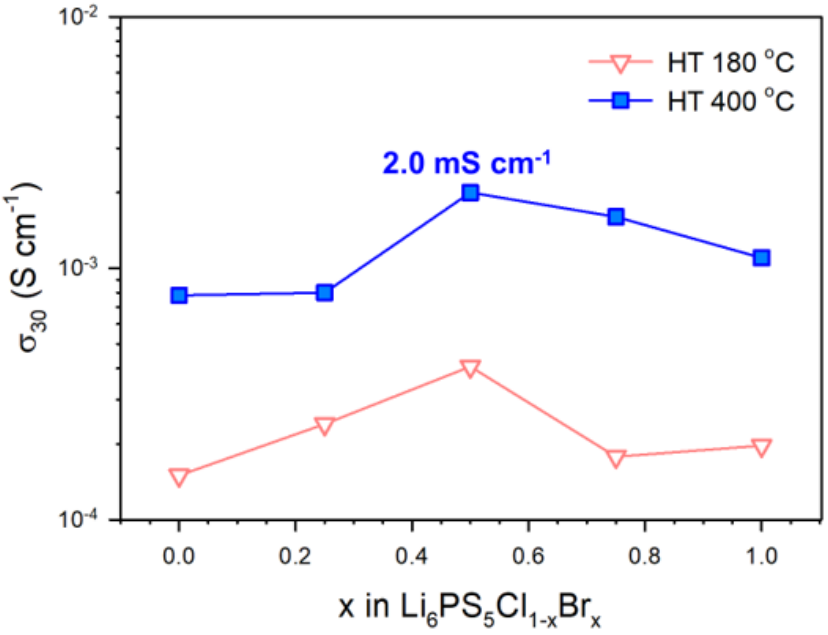

Figure 44. Li^+ conductivities of solution-processed $Li_6PS_5Cl_{1-x}Br_x$ heat-treated at 180 or 400 °C.

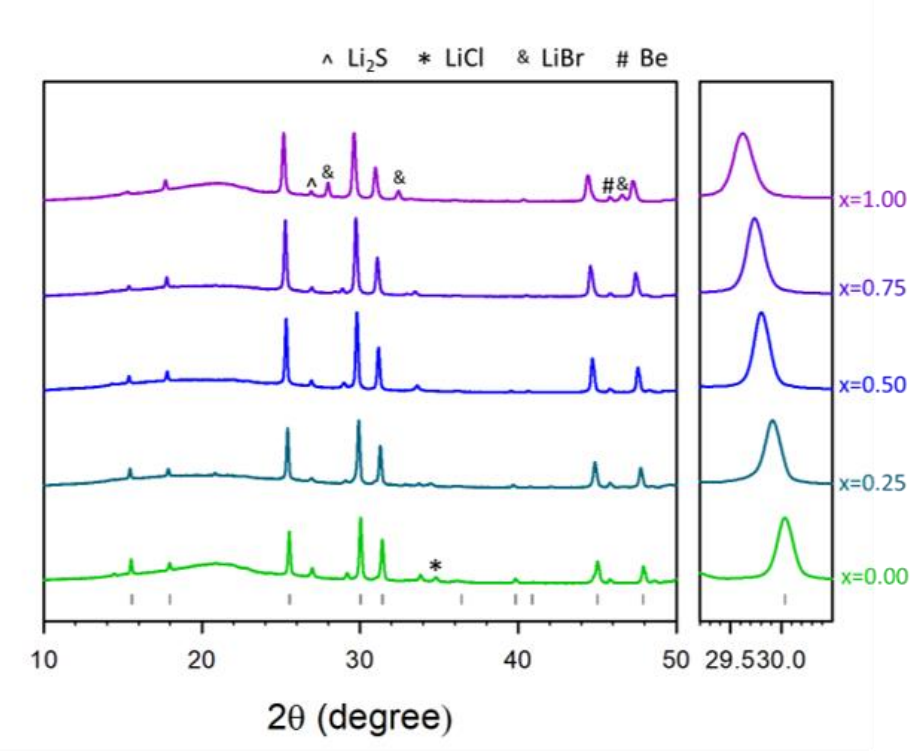

Figure 45. XRD results of solution-processed $Li_6PS_5Cl_{1-x}Br_x$ heat-treated at 400 °C.

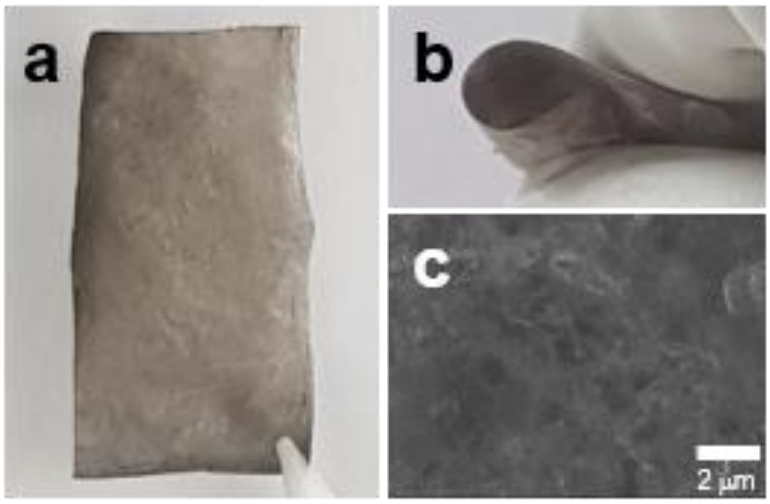

Figure 46. a) and b) photographs and surface image of the $Li_6PS_5Cl_xBr_{1-x}$-infiltrated PI membranes.

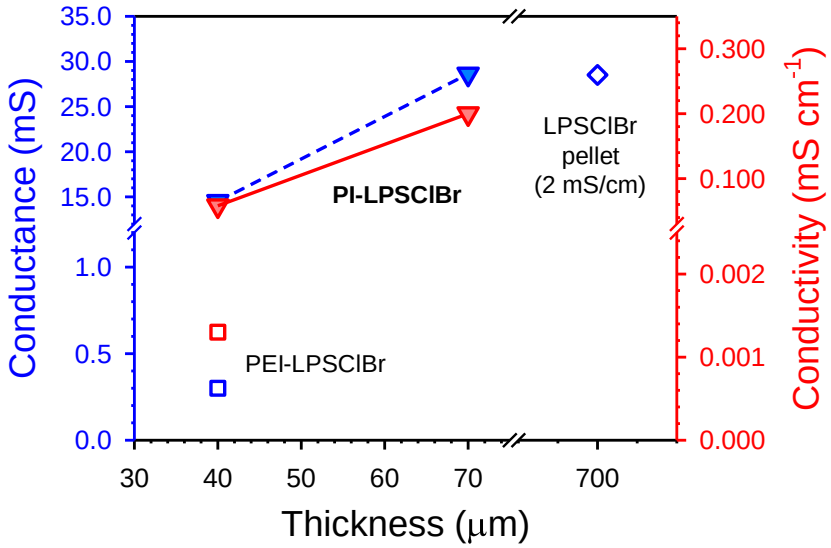

Figure 47. Li^+ conductance and conductivity of the $Li_6PS_5Cl_xBr_{1-x}$-infiltrated PI membranes with variation of thickness.

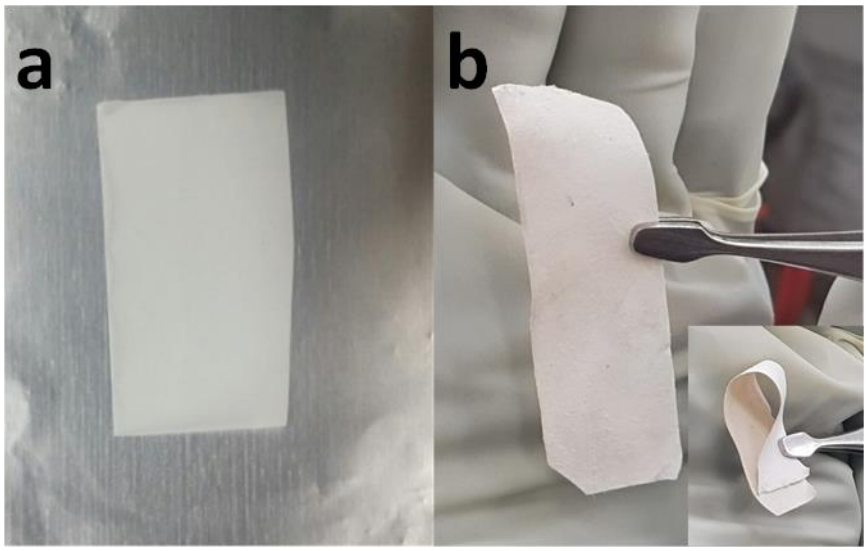

Figure 48. Photographs of a) the electrospun PEI membrane and b) the $Li_6PS_5Cl_{0.5}Br_{0.5}$-infiltrated PEI (PEI-LPSClBr) membrane. The heat-treatment temperature for PEI-LPSClBr was 180 °C.

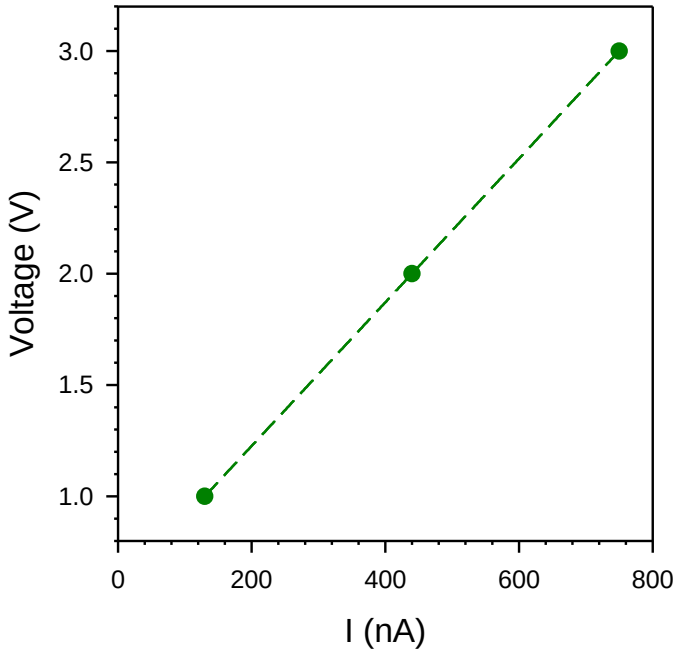

Figure 49. Linear fitting result of DC polarization curves of PI-LPSClBr.

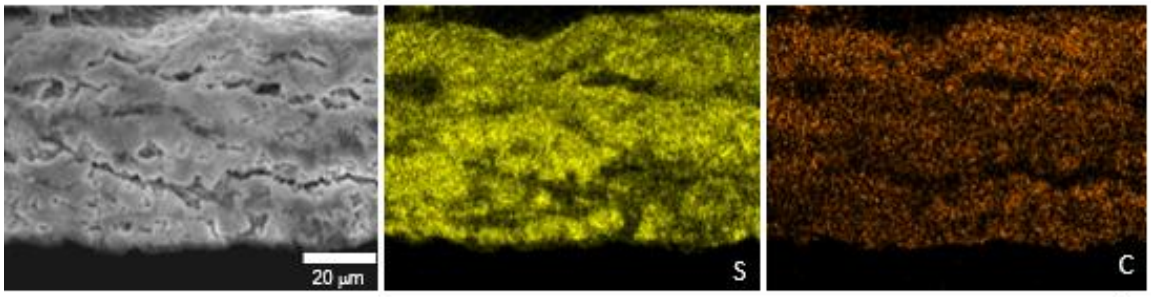

Figure 50. Cross-sectional SEM image and corresponding EDXS elemental maps of the $Li_6PS_5Cl_xBr_{1-x}$-infiltrated PI membranes.

Table 3. Characteristics of sulfide SE membranes and pellets.

Sample	Li^+ conductance[a] (mS)	Thickness (μm)	Li^+ conductivity[a] (mS cm^{-1})	Areal mass (mg cm^{-2})
PI-LPSClBr	15	40	0.058	5.0
	29	70	0.020	9.5
PEI-LPSClBr	0.30	40	0.0013	6.3
LPSClBr pellet	29	700	2.0	113

[a]At 30 °C

4.3.2 Electrochemical characterization

For electrochemical characterization, all-solid-state full cells employing thin SE membranes were fabricated. The sheet-type NCM622 and $Li_4Ti_5O_{12}$ (LTO) electrodes prepared by conventional slurry process were used as cathode and anodes, respectively. It should be noted that the ~40 μm thick SE membranes were used for full cells despite of the low Li^+ conductivity, in perspective of the cell-based energy density. Figure 51 shows the cross-sectional FESEM image and corresponding EDXS elemental maps for NCM622/PI-LPSClBr/LTO full cell, confirming that thin SE layer are in contacts with both cathode and anode layers without any cracking or short-circuiting. The first cycle charge-discharge profiles of NCM622/LTO full cells at 0.22 mA cm^{-2} (~0.1C) and 30 °C are shown in Figure 52a. The full cell employing PI-LPSClBr showed much lower capacity (~126 mA h g_{NCM622}^{-1}) than that of full cell using PEI-LPSClBr (~86 mA g_{NCM622}^{-1}) due to difference of the Li^+ conductivities. The trend for rate capabilities is also consistent with one in the Li^+ conductivities (Figure 52b). These results emphasize the excellent thermal stability of PI membranes that enables the heat-treatment at high temperature (400 °C). For achieving high-energy density, all-solid-state NCM622/graphite full cells employing 40 μm thick PI-LPSClBr were assembled, and its first two-cycle charge-discharge voltage profiles at 0.22 mA cm^{-2} (~0.1C) and 30 °C are displayed in Figure 53a. Despite of the low Li^+ conductivity of the PI-LPSClBr (0.058 mS cm^{-1}), the NCM622/graphite full cell exhibited a high reversible capacity of 146 mA h g_{NCM622}^{-1} at first cycle, which is comparable to that of previously reported NCM622/graphite full cells employing thick SE layer (> 1.0 mS cm^{-1}).[96] This result emphasizes the importance of the ionic conductance rather than the ionic conductivity on electrochemical performance and provides insights for designing thin SE membranes. The energy density of the NCM622/graphite full cell employing PI-LPSClBr is 110 Wh kg^{-1} (based on the weight of cathode, anode, SE membrane, and current collectors), which is much higher compared to those of previously reported ASLB cells using thick SE layers.[98] The stable cycling performance was also observed, indicating the capacity retention of 85.8% after 100 cycles (Figure 53b). Moreover, the NCM622/PI-LPSClBr/graphite full cell was exposed in abuse conditions (180 °C) for 1 h after cycling. Figure 54 shows the charge-discharge voltage profiles of the NCM622/PI/graphite full cell before and after exposure to 180 °C for 1 h. The negligible difference in capacity was observed, indicating that the use of PI-LPSClBr does not degrade the thermal stability of ASLBs. The OPC, the PEO-LiFTSI containing 10 wt % Al_2O_3 nanoparticles, was also prepared for comparison. In stark constrast, the OPC showed thermal shrinkage after exposure to 180 °C and lost its original shape after exposure to 400 °C (Figure 55). This implies that the use of OPC as single SE layer does not effectively prevent the internal short circuit at elevated temperature, which is directly related to battery safety. Thus, it should be emphasized that the thermal stability of polymer is also carefully considered for fabrication of SE membranes.

Finally, as motivated by liquid electrolyte injection process, the ASLB was fabricated by injecting the SE solution into the pre-assembled cathode/polymer membrane/anode assembly. As a proof of concept, conventional LCO and LTO electrodes prepared by slurry-mixing process were used as cathode and anode, respectively. The liquified LPSClBr was infiltrated into the pre-assembled LCO/PI/LTO, followed by removing solvent and heat-treatment (Figure 56a). Considering the thermal stability of PVDF binders in electrodes, heat-treatment temperature was fixed to 180 °C, which could be increased by using thermally stable polymeric binders. The first-cycle charge-discharge voltage profiles of the LPSClBr-infiltrated pre-assembled LCO/PI/LTO is displayed in Figure 56b, showing the initial capacity of 101.4 mA h g_{LCO}^{-1}.

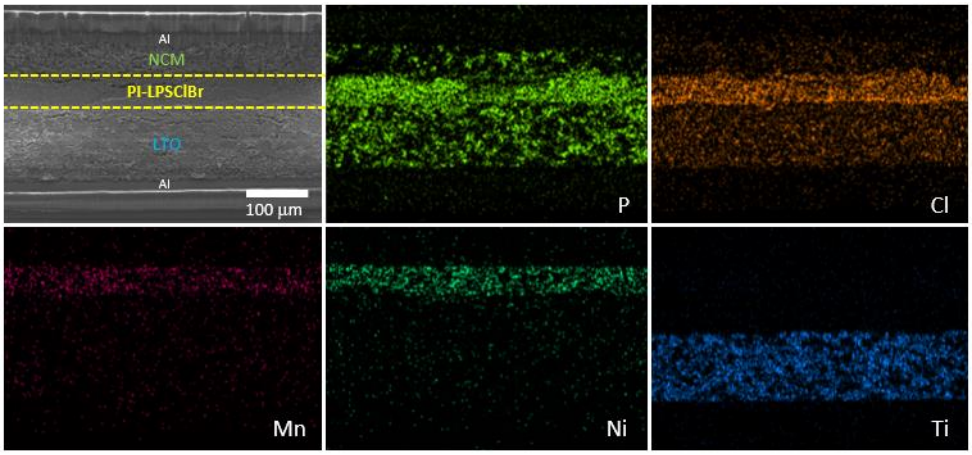

Figure 51. Cross-sectional SEM image of NCM/PI-$Li_6PS_5Cl_{0.5}Br_{0.5}$/LTO all-solid-state full-cells and its corresponding elemental maps.

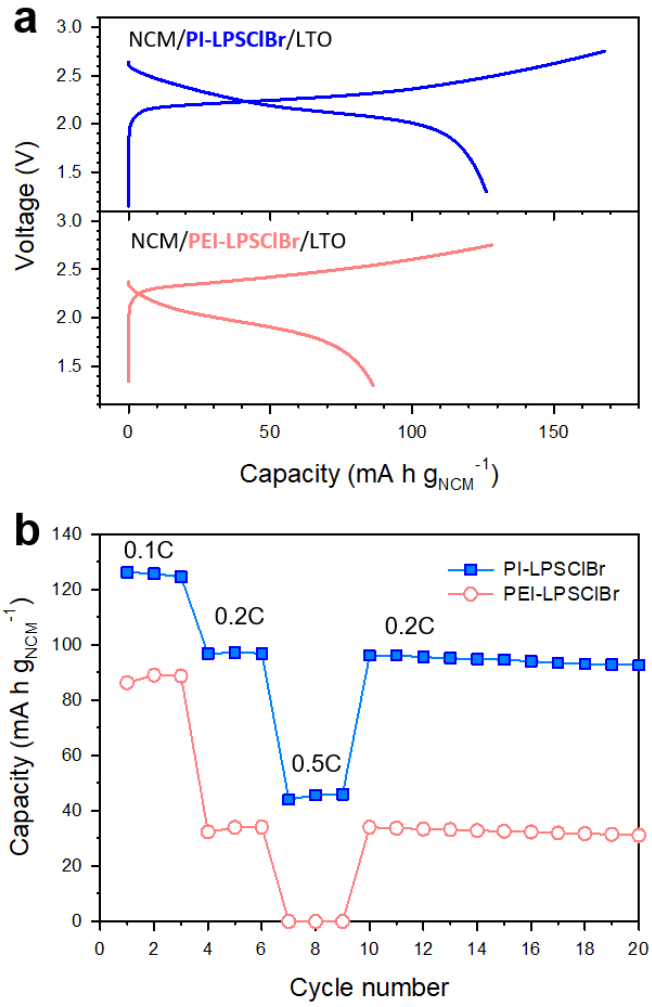

Figure 52. Results of NCM/LTO all-solid-state full-cells employing PI (or PE)-$Li_6PS_5Cl_{0.5}Br_{0.5}$ membranes. a) First-cycle charge-discharge voltage profiles of NCM/PI-$Li_6PS_5Cl_{0.5}Br_{0.5}$/LTO and NCM/PEI-$Li_6PS_5Cl_{0.5}Br_{0.5}$/LTO all-solid-state full-cells at 30 °C and b) their corresponding rate capabilities.

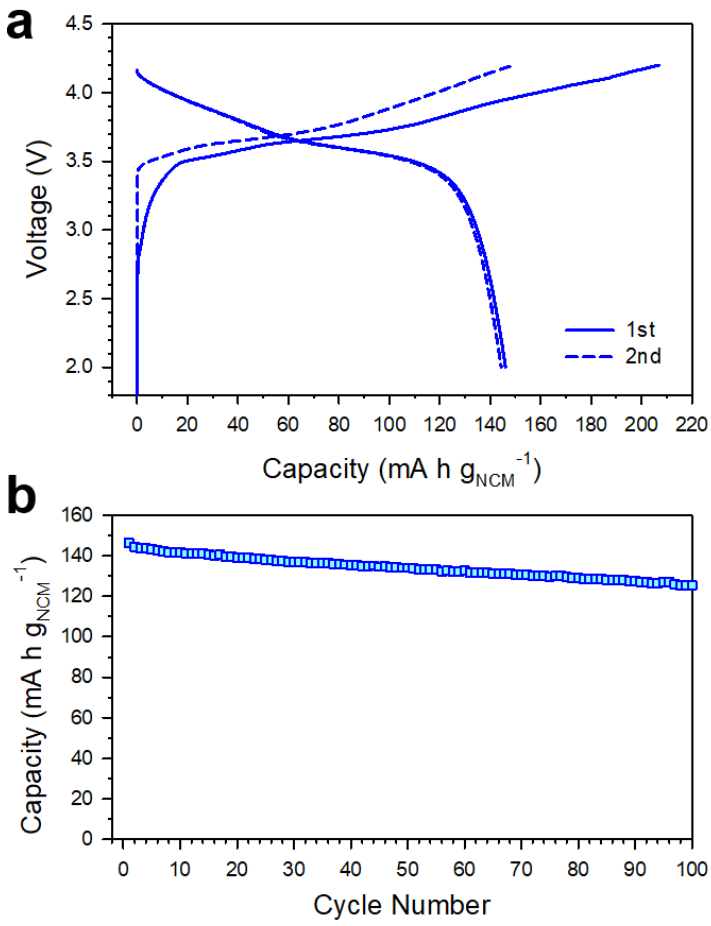

Figure 53. Results of all-solid-state full-cells employing PI-$Li_6PS_5Cl_{0.5}Br_{0.5}$ membranes. a) First two-cycle charge-discharge voltage profiles and b) the corresponding cycling performance of NCM/graphite all-solid-state full-cells employing PI-$Li_6PS_5Cl_{0.5}Br_{0.5}$ membranes at 0.1C and 30 ºC.

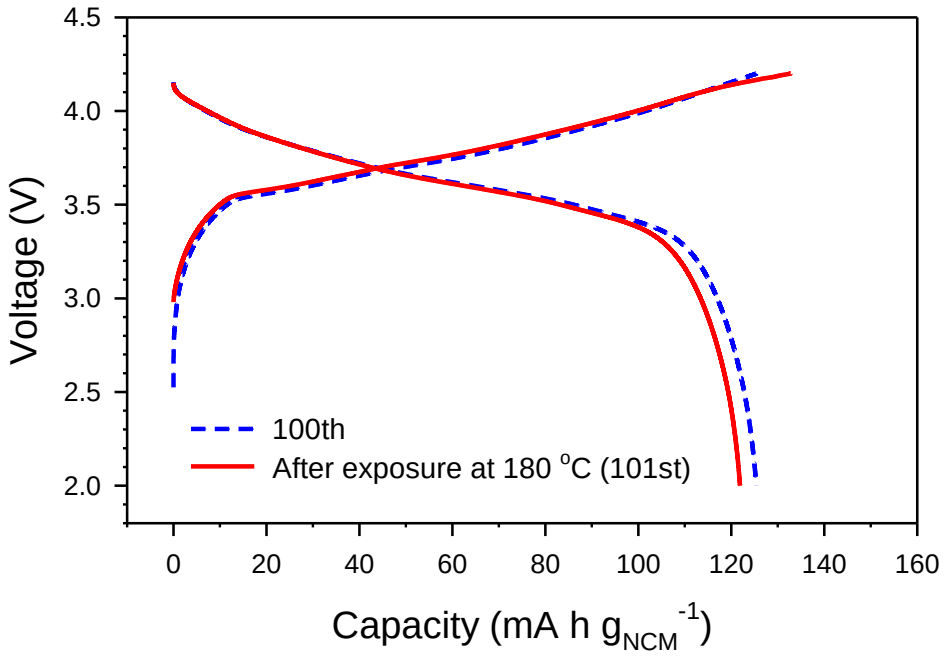

Figure 54. Charge-discharge voltage profiles for NCM/graphite all-solid-state full-cells employing PI-$Li_6PS_5Cl_{0.5}Br_{0.5}$ membranes at 0.1C and 30 °C before and after exposure to 180 °C for 1 h.

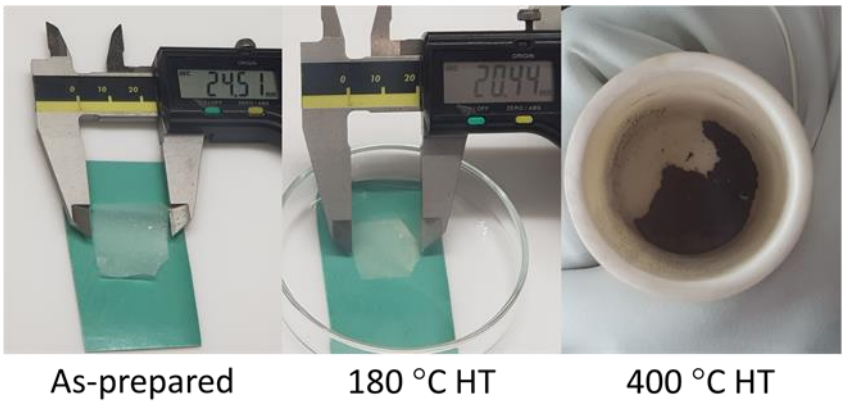

Figure 55. Photographs of PEO-LiTFSI including 10 wt % of Al_2O_3 before and after exposure to high temperature (180 and 400 °C).

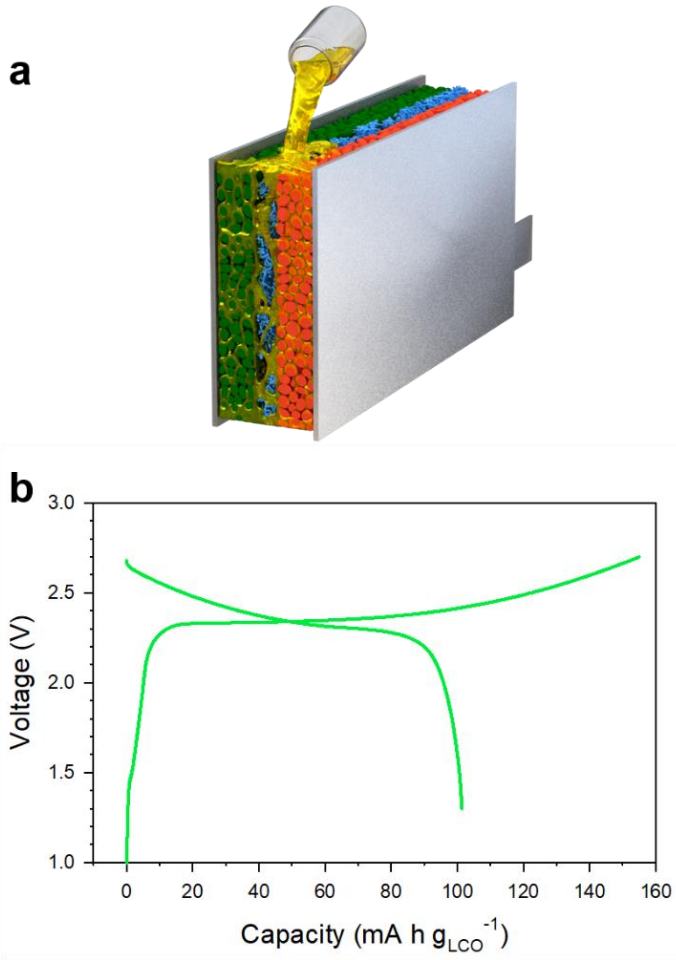

Figure 56. a) Schematic illustrating fabrication of ASLBs by injection of liquefied sulfide SEs ($Li_6PS_5Cl_{0.5}Br_{0.5}$-EtOH solution) into Al/NCM/PI NWs/LTO/Al assemblies and b) the corresponding first-cycle charge-discharge voltage profiles at 0.1C and 70 °C.

5. Conclusion

This research successfully demonstrated a new scalable fabrication protocol for practical sheet-type ASLBs by infiltration of the solution-processable sulfide SEs ($Li_6PS_5Cl_{1-x}Br_x$ ($0 \leq x \leq 1$)). The complementary analyses confirmed the compatibility of active materials with SE solution and formation of intimate ionic contacts and favorable ionic percolation. The SE-infiltrated LCO and Gr electrodes showed high reversible capacities of 141 and 364 mA h g^{-1} at 30 °C, respectively, which is comparable to that of LE-based cells. These values were comparable to those of LE cells and superior to those for conventional dry-mixed (with or without binders) and slurry-mixed (with NBR binder) all-solid-state cells, demonstrating the exceptional advantage of liquefied SEs for achieving intimate ionic contacts. The all-solid-state LCO/Gr full cells using SE-infiltrated electrodes also showed promising electrochemical performance (279 W h kg_{LCO+Gr}^{-1}) not only 30 °C but also 100 °C, highlighting the excellent thermal stability of ASLBs.

Furthermore, the sheet-type Si electrodes was also developed and showed high reversible capacities and initial CEs of over 3000 mA h g^{-1} and over 80%, respectively, which resulted from intimate ionic contacts and formation of efficient Li^+ pathways. In contrast to conventional LIBs, the effects of particle size (m-Si and n-Si) and polymeric binders (PVDF and PAA/CMC) on electrochemical performance were not significant because of the high external pressure of 140 MPa during operation of ASLBs. The comparison of cell performance with variation of external pressure demonstrated the importance of pressure engineering. The energy density of the all-solid-state LCO/Si full cell was 348 W h kg_{LCO+Si}^{-1}, which is superior to that of the LCO/Gr full cell.

Lastly, the thin and flexible SE membranes with high thermal stability were successfully developed by rational design of the highly conductive solution-processable SEs and the thermally stable porous polymer membranes. The optimization of composition of $Li_6PS_5Cl_{1-x}Br_x$ ($0 \leq x \leq 1$) and heat-treatment temperature increased the Li^+ conductivities up to 2.0 mS cm^{-1}. The PI-LPSClBr showed the comparable ionic conductance to that of pristine SE pellet with significantly reduced the mass loading of SE layer. The NCM622/Gr full cells using the PI-LPSClBr (40 μm) demonstrated the promising electrochemical performance and excellent thermal stability compared to OPC SE membranes. Finally, the new and facile fabrication protocol for ASLBs, SE injection process, was successfully demonstrated by infiltrating the liquified SEs into the pre-assembled LCO/PI/LTO assembly. This new fabrication protocol for ASLBs could provide breakthrough for practical all-solid-state battery technologies, enabling the application of scalable process for ASLBs.

Reference

1. Li, M.; Lu, J.; Chen, Z.; Amine, K., 30 Years of Lithium-Ion Batteries. *Adv. Mater.* **2018**, 1800561.

2. Cano, Z. P.; Banham, D.; Ye, S.; Hintennach, A.; Lu, J.; Fowler, M.; Chen, Z., Batteries and fuel cells for emerging electric vehicle markets. *Nat. Energy* **2018,** *3* (4), 279-289.

3. Scrosati, B.; Garche, J., Lithium batteries: Status, prospects and future. *J. Power Sources* **2010,** *195* (9), 2419-2430.

4. He, P.; Yu, H.; Li, D.; Zhou, H., Layered lithium transition metal oxide cathodes towards high energy lithium-ion batteries. *J. Mater. Chem.* **2012,** *22* (9), 3680-3695.

5. Xu, B.; Qian, D.; Wang, Z.; Meng, Y. S., Recent progress in cathode materials research for advanced lithium ion batteries. *Materials Science and Engineering: R: Reports* **2012,** *73* (5-6), 51-65.

6. Goodenough, J. B.; Kim, Y., Challenges for Rechargeable Li Batteries†. *Chem. Mater.* **2010,** *22* (3), 587-603.

7. Ellis, B. L.; Lee, K. T.; Nazar, L. F., Positive Electrode Materials for Li-Ion and Li-Batteries†. *Chem. Mater.* **2010,** *22* (3), 691-714.

8. Croguennec, L.; Palacin, M. R., Recent achievements on inorganic electrode materials for lithium-ion batteries. *J. Am. Chem. Soc.* **2015,** *137* (9), 3140-3156.

9. Liu, C.; Neale, Z. G.; Cao, G., Understanding electrochemical potentials of cathode materials in rechargeable batteries. *Mater. Today* **2016,** *19* (2), 109-123.

10. Xu, K., Electrolytes and interphases in Li-ion batteries and beyond. *Chem. Rev.* **2014,** *114* (23), 11503-11618.

11. Xu, K., Nonaqueous liquid electrolytes for lithium-based rechargeable batteries. *Chemical reviews* **2004,** *104* (10), 4303-4418.

12. Myung, S.-T.; Maglia, F.; Park, K.-J.; Yoon, C. S.; Lamp, P.; Kim, S.-J.; Sun, Y.-K., Nickel-

Rich Layered Cathode Materials for Automotive Lithium-Ion Batteries: Achievements and Perspectives. *ACS Energy Lett.* **2017,** *2* (1), 196-223.

13. Xu, W.; Wang, J.; Ding, F.; Chen, X.; Nasybulin, E.; Zhang, Y.; Zhang, J.-G., Lithium metal anodes for rechargeable batteries. *Energy Environ. Sci.* **2014,** *7* (2), 513-537.

14. Jin, Y.; Zhu, B.; Lu, Z.; Liu, N.; Zhu, J., Challenges and Recent Progress in the Development of Si Anodes for Lithium-Ion Battery. *Adv. Energy Mater.* **2017,** *7* (23), 1700715.

15. Liu, W.; Oh, P.; Liu, X.; Lee, M. J.; Cho, W.; Chae, S.; Kim, Y.; Cho, J., Nickel-rich layered lithium transition-metal oxide for high-energy lithium-ion batteries. *Angew. Chem. Int. Ed.* **2015,** *54* (15), 4440-4457.

16. Placke, T.; Kloepsch, R.; Dühnen, S.; Winter, M., Lithium ion, lithium metal, and alternative rechargeable battery technologies: the odyssey for high energy density. *J. Solid State Electrochem.* **2017,** *21* (7), 1939-1964.

17. Feng, X.; Ouyang, M.; Liu, X.; Lu, L.; Xia, Y.; He, X., Thermal runaway mechanism of lithium ion battery for electric vehicles: A review. *Energy Storage Mater.* **2018,** *10*, 246-267.

18. Hess, S.; Wohlfahrt-Mehrens, M.; Wachtler, M., Flammability of Li-Ion Battery Electrolytes: Flash Point and Self-Extinguishing Time Measurements. *J. Electrochem. Soc.* **2015,** *162* (2), A3084-A3097.

19. Hu, Y.-S., Batteries: Getting solid. *Nat. Energy* **2016,** *1* (4), 16042.

20. Janek, J.; Zeier, W. G., A solid future for battery development. *Nat. Energy* **2016,** *1* (9), 16141.

21. Jung, Y. S.; Oh, D. Y.; Nam, Y. J.; Park, K. H., Issues and Challenges for Bulk-Type All-Solid-State Rechargeable Lithium Batteries using Sulfide Solid Electrolytes. *Israel J. Chem.* **2015,** *55* (5), 472-485.

22. Ren, Y.; Chen, K.; Chen, R.; Liu, T.; Zhang, Y.; Nan, C.-W.; Vyas, B., Oxide Electrolytes for Lithium Batteries. *Journal of the American Ceramic Society* **2015,** *98* (12), 3603-3623.

23. Kerman, K.; Luntz, A.; Viswanathan, V.; Chiang, Y.-M.; Chen, Z., Review—Practical

Challenges Hindering the Development of Solid State Li Ion Batteries. *J. Electrochem. Soc.* **2017,** *164* (7), A1731-A1744.

24. Zhang, Z.; Shao, Y.; Lotsch, B.; Hu, Y.-S.; Li, H.; Janek, J.; Nazar, L. F.; Nan, C.-W.; Maier, J.; Armand, M.; Chen, L., New horizons for inorganic solid state ion conductors. *Energy Environ. Sci.* **2018,** *11* (8), 1945-1976.

25. Kato, Y.; Hori, S.; Saito, T.; Suzuki, K.; Hirayama, M.; Mitsui, A.; Yonemura, M.; Iba, H.; Kanno, R., High-power all-solid-state batteries using sulfide superionic conductors. *Nat. Energy* **2016,** *1* (4), 16030.

26. Jung, K.-N.; Shin, H.-S.; Park, M.-S.; Lee, J.-W., Solid-State Lithium Batteries: Bipolar Design, Fabrication, and Electrochemistry. *ChemElectroChem* **2019**, 6 (15), 3842-3859.

27. Keller, M.; Varzi, A.; Passerini, S., Hybrid electrolytes for lithium metal batteries. *J. Power Sources* **2018,** *392*, 206-225.

28. Sun, C.; Liu, J.; Gong, Y.; Wilkinson, D. P.; Zhang, J., Recent advances in all-solid-state rechargeable lithium batteries. *Nano Energy* **2017,** *33*, 363-386.

29. Gao, Z.; Sun, H.; Fu, L.; Ye, F.; Zhang, Y.; Luo, W.; Huang, Y., Promises, Challenges, and Recent Progress of Inorganic Solid-State Electrolytes for All-Solid-State Lithium Batteries. *Adv. Mater.* **2018,** *30* (17), e1705702.

30. Park, K. H.; Bai, Q.; Kim, D. H.; Oh, D. Y.; Zhu, Y. Z.; Mo, Y. F.; Jung, Y. S., Design Strategies, Practical Considerations, and New Solution Processes of Sulfide Solid Electrolytes for All-Solid-State Batteries. *Adv. Energy Mater.* **2018,** *8* (18), 1800035.

31. Kamaya, N.; Homma, K.; Yamakawa, Y.; Hirayama, M.; Kanno, R.; Yonemura, M.; Kamiyama, T.; Kato, Y.; Hama, S.; Kawamoto, K.; Mitsui, A., A lithium superionic conductor. *Nat. Mater.* **2011,** *10* (9), 682-686.

32. Zhou, L.; Assoud, A.; Zhang, Q.; Wu, X.; Nazar, L. F., A New Family of Argyrodite Thioantimonate Lithium Superionic Conductors. *J. Am. Chem. Soc.* **2019**, doi: 10.1021/jacs.9b08357.

33. Adeli, P.; Bazak, J. D.; Park, K. H.; Kochetkov, I.; Huq, A.; Goward, G. R.; Nazar, L. F.,

Boosting Solid-State Diffusivity and Conductivity in Lithium Superionic Argyrodites by Halide Substitution. *Angew. Chem. Int. Ed.* **2019,** *58* (26), 8681-8686.

34. Kraft, M. A.; Ohno, S.; Zinkevich, T.; Koerver, R.; Culver, S. P.; Fuchs, T.; Senyshyn, A.; Indris, S.; Morgan, B. J.; Zeier, W. G., Inducing High Ionic Conductivity in the Lithium Superionic Argyrodites $Li_{6+x}P_{1-x}Ge_xS_5I$ for All-Solid-State Batteries. *J. Am. Chem. Soc.* **2018,** *140* (47), 16330-16339.

35. Kwak, H.; Park, K. H.; Han, D.; Nam, K.-W.; Kim, H.; Jung, Y. S., Li^+ conduction in air-stable Sb-Substituted Li_4SnS_4 for all-solid-state Li-Ion Batteries. *J. Power Soureces* **2020**, *446*, 227338.

36. Park, K. H.; Oh, D. Y.; Choi, Y. E.; Nam, Y. J.; Han, L.; Kim, J. Y.; Xin, H.; Lin, F.; Oh, S. M.; Jung, Y. S., Solution-Processable Glass LiI-Li_4SnS_4 Superionic Conductors for All-Solid-State Li-Ion Batteries. *Adv. Mater.* **2016,** *28* (9), 1874-1883.

37. Miura, A.; Rosero-Navarro, N. C.; Sakuda, A.; Tadanaga, K.; Phuc, N. H. H.; Matsuda, A.; Machida, N.; Hayashi, A.; Tatsumisago, M., Liquid-phase syntheses of sulfide electrolytes for all-solid-state lithium battery. *Nat. Rev. Chem.* **2019**, 3, 189-198.

38. Liu, Z.; Fu, W.; Payzant, E. A.; Yu, X.; Wu, Z.; Dudney, N. J.; Kiggans, J.; Hong, K.; Rondinone, A. J.; Liang, C., Anomalous high ionic conductivity of nanoporous beta-Li_3PS_4. *J. Am. Chem. Soc.* **2013,** *135* (3), 975-978.

39. Rangasamy, E.; Liu, Z.; Gobet, M.; Pilar, K.; Sahu, G.; Zhou, W.; Wu, H.; Greenbaum, S.; Liang, C., An iodide-based $Li_7P_2S_8I$ superionic conductor. *J. Am. Chem. Soc.* **2015,** *137* (4), 1384-1387.

40. Ito, S.; Nakakita, M.; Aihara, Y.; Uehara, T.; Machida, N., A synthesis of crystalline $Li_7P_3S_{11}$ solid electrolyte from 1,2-dimethoxyethane solvent. *J. Power Sources* **2014,** *271*, 342-345.

41. Yao, X.; Liu, D.; Wang, C.; Long, P.; Peng, G.; Hu, Y. S.; Li, H.; Chen, L.; Xu, X., High-Energy All-Solid-State Lithium Batteries with Ultralong Cycle Life. *Nano Lett.* **2016,** *16* (11), 7148-7154.

42. Yubuchi, S.; Teragawa, S.; Aso, K.; Tadanaga, K.; Hayashi, A.; Tatsumisago, M., Preparation of high lithium-ion conducting Li_6PS_5Cl solid electrolyte from ethanol solution for all-solid-state

lithium batteries. *J. Power Sources* **2015,** *293*, 941-945.

43. Choi, Y. E.; Park, K. H.; Kim, D. H.; Oh, D. Y.; Kwak, H. R.; Lee, Y. G.; Jung, Y. S., Coatable Li_4SnS_4 Solid Electrolytes Prepared from Aqueous Solutions for All-Solid-State Lithium-Ion Batteries. *ChemSusChem* **2017,** *10* (12), 2605-2611.

44. Ito, S.; Fujiki, S.; Yamada, T.; Aihara, Y.; Park, Y.; Kim, T. Y.; Baek, S.-W.; Lee, J.-M.; Doo, S.; Machida, N., A rocking chair type all-solid-state lithium ion battery adopting Li_2O–ZrO_2 coated $LiNi_{0.8}Co_{0.15}Al_{0.05}O_2$ and a sulfide based electrolyte. *J. Power Sources* **2014,** *248*, 943-950.

45. Lee, K.; Lee, J.; Choi, S.; Char, K.; Choi, J. W., Thiol–Ene Click Reaction for Fine Polarity Tuning of Polymeric Binders in Solution-Processed All-Solid-State Batteries. *ACS Energy Lett.* **2018,** *4* (1), 94-101.

46. Oh, D. Y.; Nam, Y. J.; Park, K. H.; Jung, S. H.; Cho, S.-J.; Kim, Y. K.; Lee, Y.-G.; Lee, S.-Y.; Jung, Y. S., Excellent Compatibility of Solvate Ionic Liquids with Sulfide Solid Electrolytes: Toward Favorable Ionic Contacts in Bulk-Type All-Solid-State Lithium-Ion Batteries. *Adv. Energy Mater.* **2015,** *5* (22), 1500865.

47. Lee, K.; Kim, S.; Park, J.; Park, S. H.; Coskun, A.; Jung, D. S.; Cho, W.; Choi, J. W., Selection of Binder and Solvent for Solution-Processed All-Solid-State Battery. *J. Electrochem. Soc.* **2017,** *164* (9), A2075-A2081.

48. Sakuda, A.; Kuratani, K.; Yamamoto, M.; Takahashi, M.; Takeuchi, T.; Kobayashi, H., All-Solid-State Battery Electrode Sheets Prepared by a Slurry Coating Process. *J. Electrochem. Soc.* **2017,** *164* (12), A2474-A2478.

49. Nam, Y. J.; Oh, D. Y.; Jung, S. H.; Jung, Y. S., Toward practical all-solid-state lithium-ion batteries with high energy density and safety: Comparative study for electrodes fabricated by dry- and slurry-mixing processes. *J. Power Sources* **2018,** *375*, 93-101.

50. Hippauf, F.; Schumm, B.; Doerfler, S.; Althues, H.; Fujiki, S.; Shiratsushi, T.; Tsujimura, T.; Aihara, Y.; Kaskel, S., Overcoming binder limitations of sheet-type solid-state cathodes using a solvent-free dry-film approach. *Energy Storage Mater.* **2019**, 21, 390-398.

51. Oh, D. Y.; Kim, D. H.; Jung, S. H.; Han, J.-G.; Choi, N.-S.; Jung, Y. S., Single-step wet-

chemical fabrication of sheet-type electrodes from solid-electrolyte precursors for all-solid-state lithium-ion batteries. *J. Mater. Chem. A* **2017,** *5* (39), 20771-20779.

52. Nam, Y. J.; Cho, S. J.; Oh, D. Y.; Lim, J. M.; Kim, S. Y.; Song, J. H.; Lee, Y. G.; Lee, S. Y.; Jung, Y. S., Bendable and thin sulfide solid electrolyte film: a new electrolyte opportunity for free-standing and stackable high-energy all-solid-state lithium-ion batteries. *Nano Lett.* **2015,** *15* (5), 3317-3323.

53. Liu, L.; Xu, J.; Wang, S.; Wu, F.; Li, H.; Chen, L., Practical evaluation of energy densities for sulfide solid-state batteries. *eTransportation* **2019,** *1*, 100010.

54. Whiteley, J. M.; Taynton, P.; Zhang, W.; Lee, S. H., Ultra-thin solid-state Li-ion electrolyte membrane facilitated by a self-healing polymer matrix. *Adv. Mater.* **2015,** *27* (43), 6922-6927.

55. Liu, W.; Liu, N.; Sun, J.; Hsu, P. C.; Li, Y.; Lee, H. W.; Cui, Y., Ionic conductivity enhancement of polymer electrolytes with ceramic nanowire fillers. *Nano Lett.* **2015,** *15* (4), 2740-2745.

56. Fu, K. K.; Gong, Y.; Dai, J.; Gong, A.; Han, X.; Yao, Y.; Wang, C.; Wang, Y.; Chen, Y.; Yan, C., Flexible, solid-state, ion-conducting membrane with 3D garnet nanofiber networks for lithium batteries. *Proc. Natl. Acad. Sci. U. S. A.* **2016,** *113* (26), 7094-7099.

57. Zhai, H.; Xu, P.; Ning, M.; Cheng, Q.; Mandal, J.; Yang, Y., A Flexible Solid Composite Electrolyte with Vertically Aligned and Connected Ion-Conducting Nanoparticles for Lithium Batteries. *Nano Lett.* **2017**, 17 (5), 3182-3187.

58. Ban, X.; Zhang, W.; Chen, N.; Sun, C., A High-Performance and Durable Poly(ethylene oxide)-Based Composite Solid Electrolyte for All Solid-State Lithium Battery. *The Journal of Physical Chemistry C* **2018,** *122* (18), 9852-9858.

59. Zhang, X.; Xie, J.; Shi, F.; Lin, D.; Liu, Y.; Liu, W.; Pei, A.; Gong, Y.; Wang, H.; Liu, K.; Xiang, Y.; Cui, Y., Vertically Aligned and Continuous Nanoscale Ceramic-Polymer Interfaces in Composite Solid Polymer Electrolytes for Enhanced Ionic Conductivity. *Nano Lett.* **2018**, 18 (6), 3829-3838.

60. Li, R.; Guo, S.; Yu, L.; Wang, L.; Wu, D.; Li, Y.; Hu, X., Morphosynthesis of 3D Macroporous Garnet Frameworks and Perfusion of Polymer-Stabilized Lithium Salts for Flexible Solid-State

Hybrid Electrolytes. *Advanced Materials Interfaces* **2019,** *6* (10), 1900200.

61. Lv, F.; Wang, Z.; Shi, L.; Zhu, J.; Edström, K.; Mindemark, J.; Yuan, S., Challenges and development of composite solid-state electrolytes for high-performance lithium ion batteries. *J. Power Sources* **2019,** *441*, 227175.

62. Liu, W.; Lee, S. W.; Lin, D.; Shi, F.; Wang, S.; Sendek, A. D.; Cui, Y., Enhancing ionic conductivity in composite polymer electrolytes with well-aligned ceramic nanowires. *Nat. Energy* **2017,** *2* (5), 17035.

63. Wan, J.; Xie, J.; Mackanic, D. G.; Burke, W.; Bao, Z.; Cui, Y., Status, promises, and challenges of nanocomposite solid-state electrolytes for safe and high performance lithium batteries. *Mater. Today Nano* **2018,** *4*, 1-16.

64. Duan, H.; Fan, M.; Chen, W. P.; Li, J. Y.; Wang, P. F.; Wang, W. P.; Shi, J. L.; Yin, Y. X.; Wan, L. J.; Guo, Y. G., Extended Electrochemical Window of Solid Electrolytes via Heterogeneous Multilayered Structure for High-Voltage Lithium Metal Batteries. *Adv. Mater.* **2019**, 31 (12), 1807789.

65. Pang, Q.; Zhou, L.; Nazar, L. F., Elastic and Li-ion-percolating hybrid membrane stabilizes Li metal plating. *Proc. Natl. Acad. Sci. U. S. A.* **2018,** *115* (49), 12389-12394.

66. Chen, S.; Wang, J.; Zhang, Z.; Wu, L.; Yao, L.; Wei, Z.; Deng, Y.; Xie, D.; Yao, X.; Xu, X., In-situ preparation of poly(ethylene oxide)/Li_3PS_4 hybrid polymer electrolyte with good nanofiller distribution for rechargeable solid-state lithium batteries. *J. Power Sources* **2018,** *387*, 72-80.

67. Zhang, Q.; Cao, D.; Ma, Y.; Natan, A.; Aurora, P.; Zhu, H., Sulfide-Based Solid-State Electrolytes: Synthesis, Stability, and Potential for All-Solid-State Batteries. *Adv. Mater.* **2019**, 31 (44), 1901131.

68. Mizuno, F.; Hayashi, A.; Tadanaga, K.; Tatsumisago, M., New, Highly Ion-Conductive Crystals Precipitated from Li_2S-P_2S_5 Glasses. *Adv. Mater.* **2005,** *17* (7), 918-921.

69. Muramatsu, H.; Hayashi, A.; Ohtomo, T.; Hama, S.; Tatsumisago, M., Structural change of Li_2S–P_2S_5 sulfide solid electrolytes in the atmosphere. *Solid State Ionics* **2011,** *182* (1), 116-119.

70. Hayashi, A.; Hama, S.; Minami, T.; Tatsumisago, M., Formation of superionic crystals from

mechanically milled Li_2S–P_2S_5 glasses. *Electrochemistry Communications* **2003,** *5* (2), 111-114.

71. Dietrich, C.; Weber, D. A.; Sedlmaier, S. J.; Indris, S.; Culver, S. P.; Walter, D.; Janek, J.; Zeier, W. G., Lithium ion conductivity in Li_2S–P_2S_5 glasses – building units and local structure evolution during the crystallization of superionic conductors Li_3PS_4, $Li_7P_3S_{11}$ and $Li_4P_2S_7$. *J. Mater. Chem. A* **2017,** *5* (34), 18111-18119.

72. Kudu, Ö. U.; Famprikis, T.; Fleutot, B.; Braida, M.-D.; Le Mercier, T.; Islam, M. S.; Masquelier, C., A review of structural properties and synthesis methods of solid electrolyte materials in the Li_2S−P_2S_5 binary system. *J. Power Sources* **2018,** *407*, 31-43.

73. Deiseroth, H.-J.; Kong, S.-T.; Eckert, H.; Vannahme, J.; Reiner, C.; Zaiß, T.; Schlosser, M., Li_6PS_5X: A Class of Crystalline Li-Rich Solids With an Unusually High Li^+ Mobility. *Angew. Chem. Int. Ed.* **2008,** *120* (4), 767-770.

74. Zhu, Y.; He, X.; Mo, Y., Origin of outstanding stability in the lithium solid electrolyte materials: insights from thermodynamic analyses based on first-principles calculations. *ACS Appl. Mater. Interfaces* **2015,** *7* (42), 23685-23693.

75. Sakuda, A.; Hayashi, A.; Tatsumisago, M., Interfacial Observation between LiCoO2Electrode and Li2S−P2S5Solid Electrolytes of All-Solid-State Lithium Secondary Batteries Using Transmission Electron Microscopy. *Chem. Mater.* **2010,** *22* (3), 949-956.

76. Richards, W. D.; Miara, L. J.; Wang, Y.; Kim, J. C.; Ceder, G., Interface Stability in Solid-State Batteries. *Chem. Mater.* **2016,** *28* (1), 266-273.

77. Pervez, S. A.; Cambaz, M. A.; Thangadurai, V.; Fichtner, M., Interface in Solid-State Lithium Battery: Challenges, Progress, and Outlook. *ACS Appl Mater Interfaces* **2019,** *11* (25), 22029-22050.

78. Asano, T.; Sakai, A.; Ouchi, S.; Sakaida, M.; Miyazaki, A.; Hasegawa, S., Solid Halide Electrolytes with High Lithium-Ion Conductivity for Application in 4 V Class Bulk-Type All-Solid-State Batteries. *Adv. Mater.* **2018,** *30* (44), 1803075.

79. Kim, S.; Oguchi, H.; Toyama, N.; Sato, T.; Takagi, S.; Otomo, T.; Arunkumar, D.; Kuwata, N.; Kawamura, J.; Orimo, S. I., A complex hydride lithium superionic conductor for high-energy-density all-solid-state lithium metal batteries. *Nat. Communications* **2019,** *10* (1), 1081.

80. Shin, B. R.; Nam, Y. J.; Oh, D. Y.; Kim, D. H.; Kim, J. W.; Jung, Y. S., Comparative Study of TiS_2/Li-In All-Solid-State Lithium Batteries Using Glass-Ceramic Li_3PS_4 and $Li_{10}GeP_2S_{12}$ Solid Electrolytes. *Electrochimica Acta* **2014,** *146*, 395-402.

81. Ghidiu, M.; Ruhl, J.; Culver, S.; Zeier, W., Solution-Based Synthesis of Lithium Thiophosphate Superionic Conductors for Solid-State Batteries: A Chemistry Perspective. *J. Mater. Chem. A* **2019**, 7 (30), 17735-17753.

82. Zhou, L.; Park, K.-H.; Sun, X.; Lalère, F.; Adermann, T.; Hartmann, P.; Nazar, L. F., Solvent-Engineered Design of Argyrodite Li_6PS_5X (X = Cl, Br, I) Solid Electrolytes with High Ionic Conductivity. *ACS Energy Lett.* **2018,** *4* (1), 265-270.

83. Yubuchi, S.; Uematsu, M.; Hotehama, C.; Sakuda, A.; Hayashi, A.; Tatsumisago, M., An argyrodite sulfide-based superionic conductor synthesized by a liquid-phase technique with tetrahydrofuran and ethanol. *J. Mater. Chem. A* **2019,** *7* (2), 558-566.

84. Yubuchi, S.; Tsukasaki, H.; Sakuda, A.; Mori, S.; Hayashi, A.; Tatsumisago, M., Quantitative analysis of crystallinity in an argyrodite sulfide-based solid electrolyte synthesized via solution processing. *RSC Advances* **2019,** *9* (25), 14465-14471.

85. Yubuchi, S.; Uematsu, M.; Deguchi, M.; Hayashi, A.; Tatsumisago, M., Lithium-Ion-Conducting Argyrodite-Type Li6PS5X (X = Cl, Br, I) Solid Electrolytes Prepared by a Liquid-Phase Technique Using Ethanol as a Solvent. *ACS Applied Energy Materials* **2018,** *1* (8), 3622-3629.

86. Itoh, T.; Sato, H.; Nishina, T.; Matue, T.; Uchida, I., In situ Raman spectroscopic study of Li_xCoO_2 electrodes in propylene carbonate solvent systems. *J. Power Sources* **1997,** *68* (2), 333-337.

87. Cancado, L.; Takai, K.; Enoki, T.; Endo, M.; Kim, Y.; Mizusaki, H.; Speziali, N.; Jorio, A.; Pimenta, M., Measuring the degree of stacking order in graphite by Raman spectroscopy. *Carbon* **2008,** *46* (2), 272-275.

88. Jung, S. H.; Oh, K.; Nam, Y. J.; Oh, D. Y.; Brüner, P.; Kang, K.; Jung, Y. S., Li_3BO_3–Li_2CO_3: Rationally Designed Buffering Phase for Sulfide All-Solid-State Li-Ion Batteries. *Chem. Mater.* **2018,** *30* (22), 8190-8200.

89. Jung, Y. S.; Cavanagh, A. S.; Dillon, A. C.; Groner, M. D.; George, S. M.; Lee, S.-H., Enhanced Stability of $LiCoO_2$ Cathodes in Lithium-Ion Batteries Using Surface Modification by Atomic Layer Deposition. *J. Electrochem. Soc.* **2010,** *157* (1), A75.

90. Kwon, T. W.; Choi, J. W.; Coskun, A., The emerging era of supramolecular polymeric binders in silicon anodes. *Chem. Soc. Rev.* **2018,** *47* (6), 2145-2164.

91. Kasavajjula, U.; Wang, C.; Appleby, A. J., Nano-and bulk-silicon-based insertion anodes for lithium-ion secondary cells. *J. Power Sources* **2007,** *163* (2), 1003-1039.

92. Magasinski, A.; Zdyrko, B.; Kovalenko, I.; Hertzberg, B.; Burtovyy, R.; Huebner, C. F.; Fuller, T. F.; Luzinov, I.; Yushin, G., Toward efficient binders for Li-ion battery Si-based anodes: polyacrylic acid. *ACS Appl. Mater. Interfaces* **2010,** *2* (11), 3004-3010.

93. Li, J.; Lewis, R.; Dahn, J., Sodium carboxymethyl cellulose a potential binder for Si negative electrodes for Li-ion batteries. *Electrochemical and Solid-State Letters* **2007,** *10* (2), A17-A20.

94. Koo, B.; Kim, H.; Cho, Y.; Lee, K. T.; Choi, N. S.; Cho, J., A highly cross-linked polymeric binder for high-performance silicon negative electrodes in lithium ion batteries. *Angew. Chem. Int. Ed.* **2012,** *51* (35), 8762-8767.

95. Piper, D. M.; Yersak, T. A.; Lee, S. H., Effect of Compressive Stress on Electrochemical Performance of Silicon Anodes. *J. Electrochem. Soc.* **2012,** *160* (1), A77-A81.

96. Kim, D. H.; Oh, D. Y.; Park, K. H.; Choi, Y. E.; Nam, Y. J.; Lee, H. A.; Lee, S. M.; Jung, Y. S., Infiltration of Solution-Processable Solid Electrolytes into Conventional Li-Ion-Battery Electrodes for All-Solid-State Li-Ion Batteries. *Nano Lett.* **2017,** *17* (5), 3013-3020.

97. Jung, Y. S.; Lee, K. T.; Oh, S. M., Si–carbon core–shell composite anode in lithium secondary batteries. *Electrochimica acta* **2007,** *52* (24), 7061-7067.

98. Oh, D. Y.; Nam, Y. J.; Park, K. H.; Jung, S. H.; Kim, K. T.; Ha, A. R.; Jung, Y. S., Slurry-Fabricable Li^+-Conductive Polymeric Binders for Practical All-Solid-State Lithium-Ion Batteries Enabled by Solvate Ionic Liquids. *Adv. Energy Mater.* **2019,** *9* (16), 1802927.

99. Jiang, W.; Liu, Z.; Kong, Q.; Yao, J.; Zhang, C.; Han, P.; Cui, G., A high temperature operating

nanofibrous polyimide separator in Li-ion battery. *Solid State Ionics* **2013,** *232*, 44-48.

100. Wang, H.; Yu, C.; Ganapathy, S.; van Eck, E. R. H.; van Eijck, L.; Wagemaker, M., A lithium argyrodite $Li_6PS_5Cl_{0.5}Br_{0.5}$ electrolyte with improved bulk and interfacial conductivity. *J. Power Sources* **2019,** *412*, 29-36.

101. Kraft, M. A.; Culver, S. P.; Calderon, M.; Bocher, F.; Krauskopf, T.; Senyshyn, A.; Dietrich, C.; Zevalkink, A.; Janek, J.; Zeier, W. G., Influence of Lattice Polarizability on the Ionic Conductivity in the Lithium Superionic Argyrodites Li_6PS_5X (X = Cl, Br, I). *J. Am. Chem. Soc.* **2017**, 139 (3), 10909-10918.\

102. Kim, D. H.; Lee, H. A.; Song, Y. B.; Park, J. W.; Lee, S. -M.; Jung, Y. S., Sheet-type Li6PS5Cl-infiltrated Si anodes fabricated by solution process for all-solid-state lithium-ion batteries. *J. Power Sources* **2019***, 426,* 143.

Permission

- Some part of chapter 4.1 is reproduced with permission - Kim, D. H.; Oh, D. Y.; Park, K. H.; Choi, Y. E.; Nam, Y. J.; Lee, H. A.; Lee, S. M.; Jung, Y. S., Infiltration of Solution-Processable Solid Electrolytes into Conventional Li-Ion-Battery Electrodes for All-Solid-State Li-Ion Batteries. *Nano Lett.* **2017,** *17* (5), 3013-3020. Copyright 2017 American Chemical Society.

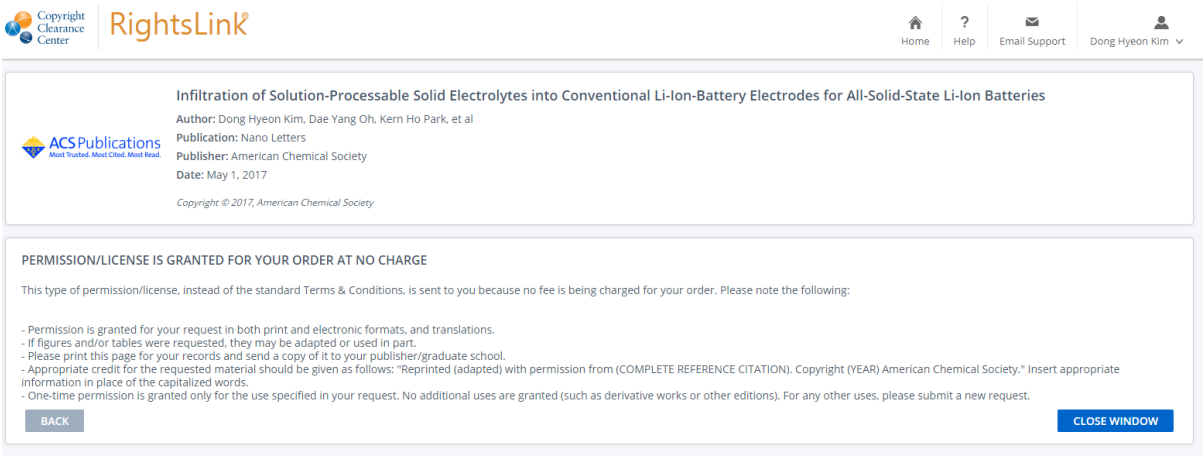

- Some part of chapter 4.2 is reproduced with permission - Kim, D. H.; Lee, H. A.; Song, Y. B.; Park, J. W.; Lee, S. -M.; Jung, Y. S., Sheet-type Li6PS5Cl-infiltrated Si anodes fabricated by solution process for all-solid-state lithium-ion batteries. *J. Power Sources* **2019**, *426,* 143. Copyright 2019 Elsevier.

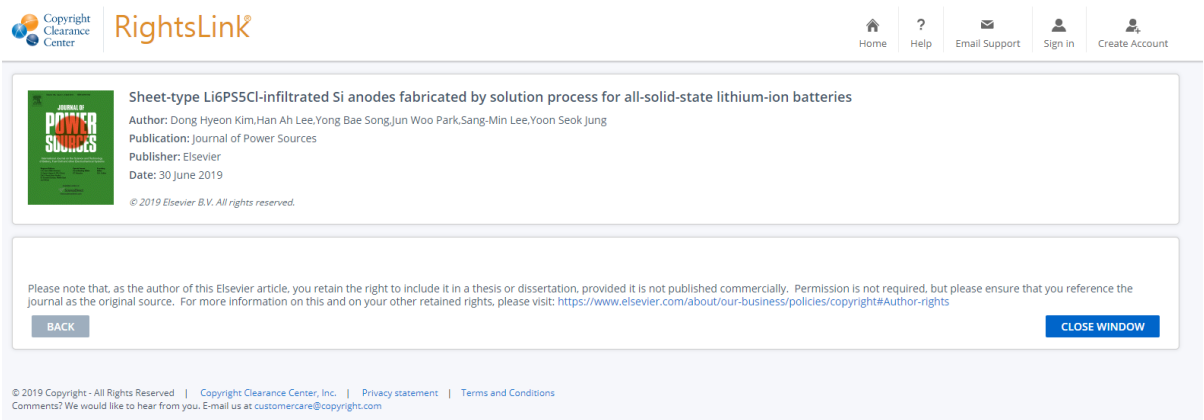

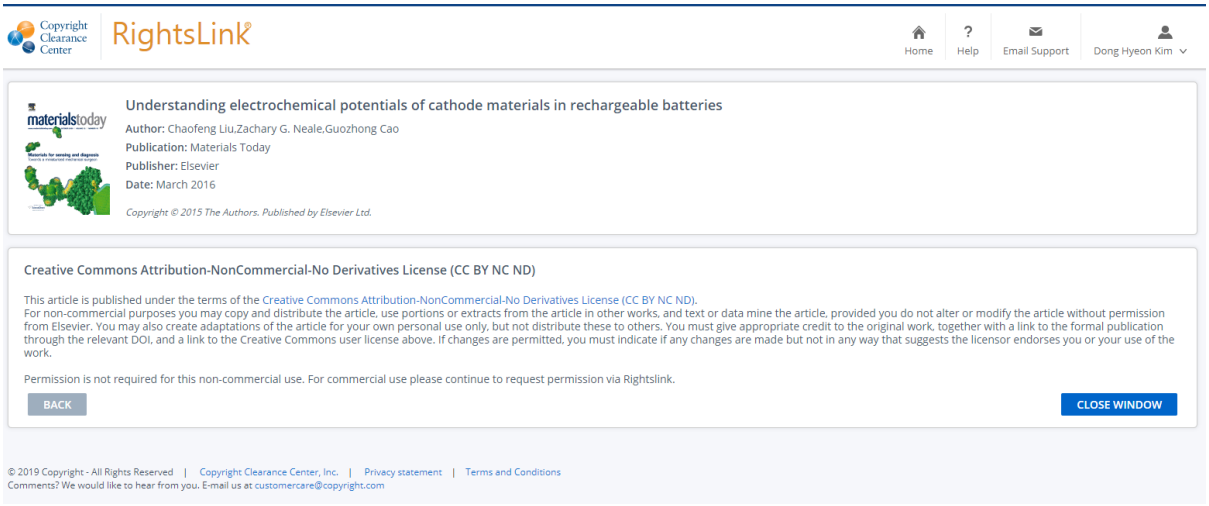

Copyright Clearance Center | RightsLink®

Home | Help | Email Support | Dong Hyeon Kim

Understanding electrochemical potentials of cathode materials in rechargeable batteries

Author: Chaofeng Liu,Zachary G. Neale,Guozhong Cao
Publication: Materials Today
Publisher: Elsevier
Date: March 2016

Copyright © 2015 The Authors. Published by Elsevier Ltd.

Creative Commons Attribution-NonCommercial-No Derivatives License (CC BY NC ND)

This article is published under the terms of the Creative Commons Attribution-NonCommercial-No Derivatives License (CC BY NC ND).
For non-commercial purposes you may copy and distribute the article, use portions or extracts from the article in other works, and text or data mine the article, provided you do not alter or modify the article without permission from Elsevier. You may also create adaptations of the article for your own personal use only, but not distribute these to others. You must give appropriate credit to the original work, together with a link to the formal publication through the relevant DOI, and a link to the Creative Commons user license above. If changes are permitted, you must indicate if any changes are made but not in any way that suggests the licensor endorses you or your use of the work.

Permission is not required for this non-commercial use. For commercial use please continue to request permission via Rightslink.

BACK | CLOSE WINDOW

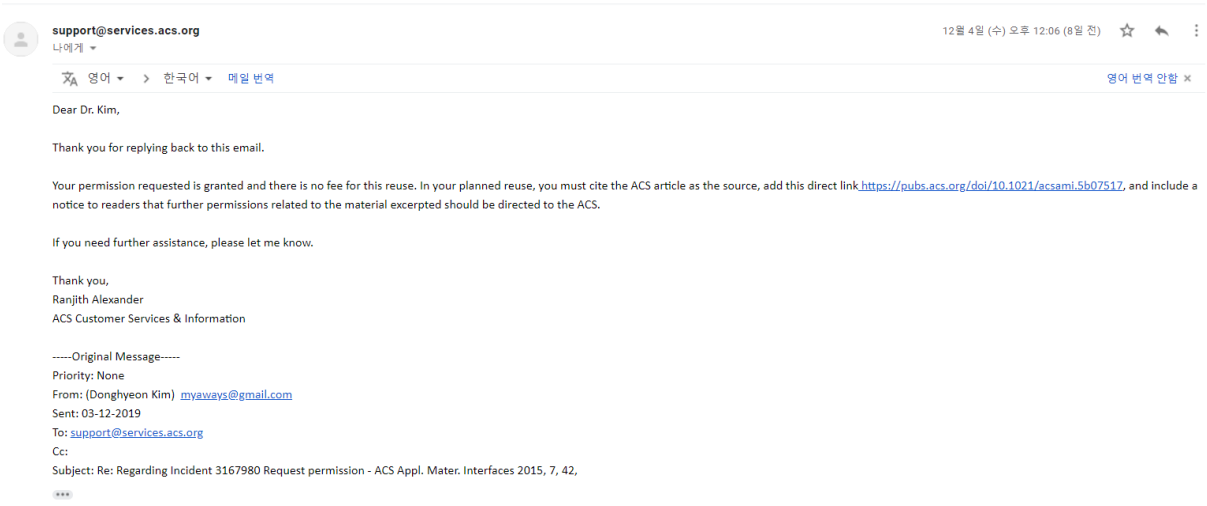

support@services.acs.org
나에게

12월 4일 (수) 오후 12:06 (8일 전)

영어 > 한국어 메일 번역 | 영어 번역 안함

Dear Dr. Kim,

Thank you for replying back to this email.

Your permission requested is granted and there is no fee for this reuse. In your planned reuse, you must cite the ACS article as the source, add this direct link https://pubs.acs.org/doi/10.1021/acsami.5b07517, and include a notice to readers that further permissions related to the material excerpted should be directed to the ACS.

If you need further assistance, please let me know.

Thank you,
Ranjith Alexander
ACS Customer Services & Information

-----Original Message-----
Priority: None
From: (Donghyeon Kim) myaways@gmail.com
Sent: 03-12-2019
To: support@services.acs.org
Cc:
Subject: Re: Regarding Incident 3167980 Request permission - ACS Appl. Mater. Interfaces 2015, 7, 42,

JOHN WILEY AND SONS LICENSE
TERMS AND CONDITIONS

Nov 30, 2019

This Agreement between Dong Hyeon Kim ("You") and John Wiley and Sons ("John Wiley and Sons") consists of your license details and the terms and conditions provided by John Wiley and Sons and Copyright Clearance Center.

License Number	4718710717887
License date	Nov 30, 2019
Licensed Content Publisher	John Wiley and Sons
Licensed Content Publication	Advanced Energy Materials
Licensed Content Title	Design Strategies, Practical Considerations, and New Solution Processes of Sulfide Solid Electrolytes for All-Solid-State Batteries
Licensed Content Author	Yoon Seok Jung, Yifei Mo, Yizhou Zhu, et al
Licensed Content Date	Apr 23, 2018
Licensed Content Volume	8
Licensed Content Issue	18
Licensed Content Pages	24

Type of use	Dissertation/Thesis
Requestor type	Author of this Wiley article
Format	Print and electronic
Portion	Figure/table
Number of figures/tables	2
Original Wiley figure/table number(s)	Figure 1b and figure 6
Will you be translating?	No
Title of your thesis / dissertation	Development of Sheet-Type All-Solid-State Li-Ion Batteries Using Solution-Processable Sulfide Solid Electrolytes
Expected completion date	Feb 2020
Expected size (number of pages)	101
Requestor Location	Dong Hyeon Kim 222, Wangsimni-ro, Seongdong-gu Seoul, 04763 Korea, Republic Of Attn: Dong Hyeon Kim
Publisher Tax ID	EU826007151
Total	0.00 USD

SPRINGER NATURE LICENSE
TERMS AND CONDITIONS

Nov 30, 2019

This Agreement between Dong Hyeon Kim ("You") and Springer Nature ("Springer Nature") consists of your license details and the terms and conditions provided by Springer Nature and Copyright Clearance Center.

License Number	4718720279320
License date	Nov 30, 2019
Licensed Content Publisher	Springer Nature
Licensed Content Publication	Nature Reviews Chemistry
Licensed Content Title	Liquid-phase syntheses of sulfide electrolytes for all-solid-state lithium battery
Licensed Content Author	Akira Miura et al
Licensed Content Date	Feb 19, 2019
Type of Use	Thesis/Dissertation
Requestor type	academic/university or research institute
Format	print and electronic
Portion	figures/tables/illustrations
Number of figures/tables/illustrations	1

High-res required	no
Will you be translating?	no
Circulation/distribution	1 - 29
Author of this Springer Nature content	no
Title	Development of Sheet-Type All-Solid-State Li-Ion Batteries Using Solution-Processable Sulfide Solid Electrolytes
Institution name	n/a
Expected presentation date	Feb 2020
Portions	Figure 3g
Requestor Location	Dong Hyeon Kim 222, Wangsimni-ro, Seongdong-gu Seoul, 04763 Korea, Republic Of Attn: Dong Hyeon Kim
Total	0.00 USD

Terms and Conditions

Springer Nature Customer Service Centre GmbH
Terms and Conditions

This agreement sets out the terms and conditions of the licence (the **Licence**) between you and **Springer Nature Customer Service Centre GmbH** (the **Licensor**). By clicking 'accept' and completing the transaction for the material (**Licensed Material**), you also confirm your acceptance of these terms and conditions.

JOHN WILEY AND SONS LICENSE
TERMS AND CONDITIONS

Nov 30, 2019

This Agreement between Dong Hyeon Kim ("You") and John Wiley and Sons ("John Wiley and Sons") consists of your license details and the terms and conditions provided by John Wiley and Sons and Copyright Clearance Center.

License Number	4718711028633
License date	Nov 30, 2019
Licensed Content Publisher	John Wiley and Sons
Licensed Content Publication	Israel Journal of Chemistry
Licensed Content Title	Issues and Challenges for Bulk-Type All-Solid-State Rechargeable Lithium Batteries using Sulfide Solid Electrolytes
Licensed Content Author	Kern Ho Park, Young Jin Nam, Dae Yang Oh, et al
Licensed Content Date	Jan 23, 2015
Licensed Content Volume	55
Licensed Content Issue	5
Licensed Content Pages	14

Type of use	Dissertation/Thesis
Requestor type	University/Academic
Format	Print and electronic
Portion	Figure/table
Number of figures/tables	1
Original Wiley figure/table number(s)	Figure 1
Will you be translating?	No
Title of your thesis / dissertation	Development of Sheet-Type All-Solid-State Li-Ion Batteries Using Solution-Processable Sulfide Solid Electrolytes
Expected completion date	Feb 2020
Expected size (number of pages)	101
Requestor Location	Dong Hyeon Kim 222, Wangsimni-ro, Seongdong-gu Seoul, 04763 Korea, Republic Of Attn: Dong Hyeon Kim
Publisher Tax ID	EU826007151
Total	0.00 USD